

# **NATURAL AIR CIRCULATION MODEL DEVELOPMENT FOR THE DIGINDY TUNNEL**

by

**Luis Carlos Maldonado Jaime**

**A Thesis**

*Submitted to the Faculty of Purdue University*

*In Partial Fulfillment of the Requirements for the degree of*

**Master of Science**



School of Engineering Technology

West Lafayette, Indiana

August 2021

**THE PURDUE UNIVERSITY GRADUATE SCHOOL**  
**STATEMENT OF COMMITTEE APPROVAL**

**Dr. Jason Ostanek, Chair**

School of Engineering Technology

**Dr. José Garcia**

School of Engineering Technology

**Prof. William Hutzel**

School of Engineering Technology

**Dr. Emad Elwakil**

School of Construction Management

**Approved by:**

Dr. Duane D. Dunlap

*Dedicated to my family that always supported me during this journey*

## **ACKNOWLEDGMENTS**

I want to thank my advisor Dr. Jason Ostanek for trusting me and providing me the opportunity to work on this research. Also, I want to thank Dr. Jason Ostanek for the personal and academic advice that encouraged me during the degree.

I want to acknowledge my thesis committee for their comments and guidance. I want to thank my family for supporting and cheering me during this process. I also want to thank all my colleagues and close friends that gave me their hands in the most challenging times.

Finally, I want to acknowledge the support of Olivia Hawbaker and Mike Miller, from Citizens Energy Group, for supporting the project and guide me on the DigIndy tunnel's functionality and construction.

## TABLE OF CONTENTS

LIST OF TABLES .....	9
LIST OF FIGURES .....	10
LIST OF ABBREVIATIONS.....	13
LIST OF SYMBOLS .....	14
GLOSSARY .....	17
ABSTRACT.....	19
CHAPTER 1. INTRODUCTION .....	20
1.1 Introduction of the Problem and Purpose .....	20
1.2 Problem Statement .....	21
1.2.1 Significance of the Problem.....	21
1.3 Purpose Statement.....	21
1.3.1 Significance of the Purpose .....	22
1.4 Research Questions .....	22
1.5 Assumptions.....	23
1.6 Delimitations.....	24
1.7 Limitations .....	24
1.8 Summary .....	25
CHAPTER 2. REVIEW OF LITERATURE .....	26
2.1 Findings Pertaining to the Problem and Purpose.....	26
2.2 Findings Pertaining to the Methodology.....	28
2.2.1 Relevant Factors for Air Circulation in Sewer Systems .....	28
2.2.2 Ventilation Modeling for Sewer Systems.....	29
2.2.3 Natural Air Circulation in Long Tunnels.....	32
2.3 Uniqueness of the Present Work.....	34
2.4 Summary .....	34
CHAPTER 3. RESEARCH METHODOLOGY .....	36
3.1 Introduction of the Research Methodology .....	36
3.2 DigIndy Tunnel .....	36
3.2.1 Initial Alignment (DRTC+ECT).....	37

3.2.2 Second Alignment (DRTC+ECT+WRT+LPgRT) .....	40
3.2.3 Third Alignment (DRTC+ECT+WRT+LPgRT+FCT) .....	40
3.2.4 Fourth Alignment (DRTC+ECT+WRT+LPgRT+FCT+PRDT) .....	40
3.2.5 DigIndy Tunnel Openings .....	40
3.3 Experimental Procedure .....	41
3.3.1 Instrumentation Selection .....	42
3.3.2 Experimental Setup .....	44
3.3.3 Data Collection .....	46
3.3.4 Initial Testing of Instrumentation .....	47
3.4 Numerical Modeling Procedure .....	47
3.4.1 Modeled Physics .....	48
3.4.1.3 Buoyancy Forces .....	48
3.4.1.3.1 Humid Air Modeling .....	48
3.4.1.3.2 Condensation .....	50
3.4.1.1 Pressure Differences .....	52
3.4.1.1.1 Static Pressure Difference .....	53
3.4.1.1.2 Thermal Potential Pressure Difference .....	53
3.4.1.1.3 Wind Suction Pressure Difference .....	54
3.4.1.4 Clear Water Stream .....	55
3.4.2 Computational Model Setup .....	57
3.4.2.1 Computational Mesh .....	57
3.4.2.1.1 Tunnel Geometry Simplification .....	58
3.4.2.1.2 Meshing Strategy .....	58
3.4.2.1.3 Mesh Independence Analysis .....	61
3.4.2.2 Computational Model Configuration .....	62
3.4.2.3 Momentum Boundary Conditions .....	63
3.4.2.3.1 Entries and Exits Minor Loss Coefficients .....	63
3.4.2.4 Thermal Boundary Conditions .....	65
3.4.2.5 Species Boundary Conditions .....	66
3.4.2.5.1 Clear Water Stream Species Boundary Condition .....	66
3.4.3 Computational Model Validation Procedure .....	66

3.4.3.1 Experimental Measurement Uncertainty .....	67
CHAPTER 4. RESULTS .....	69
4.1 Effect of Seasonal Condition .....	69
4.1.1 Surface Weather Station Experimental Results .....	69
4.1.2 In-Shaft Station Experimental Results and Model Validation .....	73
4.1.2.1 In-Shaft Vertical Velocity Results .....	73
4.1.2.2 In-Shaft Temperature Results.....	75
4.1.2.3 In-Shaft Water Vapor Mass Fraction Results.....	77
4.1.3 Discussion of Seasonal Effect and Model Validation .....	78
4.1.3.1. Sinking Effect.....	79
4.1.3.1. Discrepancy at Utility Shaft No.3 .....	79
4.1.3.1. Longitudinal Temperature Distribution from Cold Air Ingestion.....	80
4.2 Effect of Tunnel Alignment .....	86
4.2.1 Boundary Conditions for Future Alignments .....	87
4.2.2 Initial Alignment Effect (DRTC+ECT).....	88
4.2.3 Second Alignment Effect (DRTC+ECT+WRT+LPgRT) .....	91
4.2.4 Third Alignment Effect (DRTC+ECT+WRT+LPgRT+WRT) .....	93
4.2.5 Fourth Alignment Effect (DRTC+ECT+WRT+LPgRT+WRT+PRDT).....	95
4.2.6 Discussion of Alignment Effect.....	98
CHAPTER 5. SUMMARY, CONCLUSIONS, AND RECOMMENDATIONS.....	100
5.1 Summary .....	100
5.2 Conclusions.....	100
5.3 Answer to Research Questions .....	101
5.4 Recommendations.....	103
LIST OF REFERENCES .....	104
APPENDIX A – INSTRUMENTS RESOLUTION, ACCURACY, AND UNCERTAINTY ..	109
APPENDIX B – TECHNICAL DRAWING OF 8020 ALUMINUM STRUCTURES .....	110
APPENDIX C – BILL OF MATERIALES.....	131
APPENDIX D – MONTHLY NO-RAIN CONDITION SURFACE MEASUREMENTS .....	137
APPENDIX E – CFD BOUNDARY CONDITIONS FOR DRTC+ECT ALIGNMENT .....	140

APPENDIX F – DRTC+ECT ALIGNMENT MONTHLY IN-SHAFT EXPERIMENTAL MEASUREMENTS .....	141
-------------------------------------------------------------------------------------	-----



## LIST OF TABLES

<i>Table 3.1.</i> Hydraulic diameter and the total opening area of openings. ....	41
<i>Table 3.2.</i> Species transportation model configuration. ....	49
<i>Table 3.3.</i> Air and water vapor properties. ....	49
<i>Table 3.4.</i> Water’s latent heat of evaporation, latent heat of sublimation, and enthalpy of saturated liquid water. ....	51
<i>Table 3.5.</i> Height difference with respect to screen shaft opening for each opening. ....	54
<i>Table 3.6.</i> Clear water stream volumetric flow, velocity flow, and water height for each alignment.....	56
<i>Table 3.7.</i> Information of the number of cells and control quality values for the different alignment meshes.....	61
<i>Table 3.8.</i> Minor loss coefficients for openings in the DigIndy tunnel. ....	65
<i>Table 4.1.</i> Dry weather times (no-rain/no-fill conditions). ....	70
<i>Table 4.2.</i> Value configurations for cold conditions simulations. ....	87
<i>Table 4.3.</i> Value configurations for warm conditions simulations. ....	88
<i>Table 4.4.</i> DRTC+ECT alignment cold conditions results. ....	88
<i>Table 4.5.</i> DRTC+ECT alignment warm conditions results.....	90
<i>Table 4.6.</i> DRTC+ECT+WRT+LPgRT alignment cold conditions results.....	91
<i>Table 4.7.</i> DRTC+ECT+WRT+LPgRT alignment warm conditions results.....	92
<i>Table 4.8.</i> DRTC+ECT+WRT+LPgRT+WRT alignment cold conditions results.....	93
<i>Table 4.9.</i> DRTC+ECT+WRT+LPgRT+WRT alignment warm conditions results. ....	94
<i>Table 4.10.</i> DRTC+ECT+WRT+LPgRT+WRT+PRDT alignment cold conditions results. ....	96
<i>Table 4.11.</i> DRTC+ECT+WRT+LPgRT+WRT+PRDT alignment warm conditions results.....	97

## LIST OF FIGURES

<i>Figure 2.1.</i> Schematic of opening geometries considered by Pescod and Price (1982): a) venturi extractor, b) slotted extractor, and c) plain open. ....	30
<i>Figure 2.2.</i> Schematic of parameters affecting the natural air circulation in extra-long inclined straight tunnels. ....	33
<i>Figure 3.1.</i> DigIndy final tunnel layout over Indianapolis map. <i>Note.</i> Black schematic lines represent DRTC+ECT tunnel alignment. Edited from “DingIndy tunnel layout [Handout],” by Citizens Energy Group, 2016. Reprinted with permission. ....	38
<i>Figure 3.2.</i> DigIndy tunnel alignments with the atmosphere openings: a) DRTC+ECT, b) DRTC+ECT+WRT+LPgRT, c) DRTC+ECT+WRT+LPgRT+WRT, and d) DRTC+ECT+WRT+LPgRT+WRT+PRT. <i>Note.</i> Black rectangles represent bulkhead locations. ....	39
<i>Figure 3.3.</i> Relation between experimental measurements and CFD model. ....	42
<i>Figure 3.4.</i> Instrumentation deployment for DRTC+ECT alignment: a) schematic of instrumentation location for the initial alignment, b) outside weather station installed in utility shaft No.3 location, and c) inside weather station installed in the Eagle Creek drop shaft. <i>Note.</i> Figure 3.4.c adapted from “Underground weather forecast: 0% chance of stink,” by John O’Malley, 2021, Purdue Polytechnic Newsroom. ( <a href="https://polytechnic.purdue.edu/newsroom/underground-weather-forecast-0-chance-of-stink">https://polytechnic.purdue.edu/newsroom/underground-weather-forecast-0-chance-of-stink</a> ). In the public domain. ....	45
<i>Figure 3.5.</i> In-shaft weather final location in screen shaft. <i>Note.</i> Dotted lines represent the central geometrical axes of the opening. ....	46
<i>Figure 3.6.</i> Zentra cloud interface: a) Zentra cloud webpage and b) utility shaft No.3 example measurement visualization. ....	47
<i>Figure 3.7.</i> Schematic of water height in the tunnel’s bottom. ....	55
<i>Figure 3.8.</i> Schematic of the velocity vector direction of the clear water stream. ....	56
<i>Figure 3.9.</i> Schematics of tunnel alignment mesh simplifications: a) computational mesh for DRTC+ECT alignment, b) computational mesh for DRTC+ECT+WRT+LPgRT, c) computational mesh for DRTC+ECT+WRT+LPgRT+WRT, and d) computation mesh for DRTC+ECT+WRT+LPgRT+WRT+PRT alignment. <i>Note.</i> Dashed lines represent sections of the tunnel removed. ....	59
<i>Figure 3.10.</i> Types of meshes over T-junction. ....	60
<i>Figure 3.11.</i> Results of mesh independence analysis: a) vertical velocity in-shaft openings mesh independence, b) temperature in-shaft openings mesh independence, and c) mass fraction in-shaft openings mesh independence. ....	62

<i>Figure 4.1.</i> Atmospheric conditions in the DRTC+ECT alignment openings from May 2020 to April 2021: a) atmospheric pressure over the DRTC+ECT alignment openings, b) atmospheric temperature over the DRTC+ECT alignment openings, c) wind speed magnitude at 1.83 m over DRTC+ECT alignment openings, and d) atmospheric vapor pressure over the DRTC+ECT alignment openings. ....	71
<i>Figure 4.2.</i> Experimental and CFD in-shaft vertical velocity results from May 2020 to April 2021: a) vertical air velocity in Eagle Creek vent shaft, b) vertical air velocity in Eagle Creek drop shaft, c) vertical air velocity in utility shaft No.3 shaft, and d) vertical air velocity in screen shaft.....	74
<i>Figure 4.3.</i> Surface experimental temperature measurements and experimental and CFD in-shaft temperature results, from May 2020 to April 2021: a) air temperature in Eagle Creek vent shaft, b) air temperature in Eagle Creek drop shaft, c) air temperature in utility shaft No.3 shaft, and d) air temperature in screen shaft. ....	76
<i>Figure 4.4.</i> Surface experimental water vapor mass fraction measurements and experimental and CFD in-shaft water vapor mass fraction results, from May 2020 to April 2021: a) water vapor mass fraction in Eagle Creek vent shaft, b) water vapor mass fraction in Eagle Creek drop shaft, c) water vapor mass fraction in utility shaft No.3 shaft, and d) water vapor mass fraction screen shaft.....	78
<i>Figure 4.5.</i> Schematic of air temperature distribution inside the tunnel: a) scenario with uniform wall temperature and b) scenario with non-uniform wall temperature distribution. ....	81
<i>Figure 4.6.</i> Considerations for linear temperature profile in the tunnel. ....	83
<i>Figure 4.7.</i> Experimental, CFD, and CFD linear profile in-shaft vertical velocity results from December 2020 to March 2021: a) vertical air velocity in Eagle Creek vent shaft, b) vertical air velocity in Eagle Creek drop shaft, c) vertical air velocity in utility shaft No.3 shaft, and d) vertical air velocity in screen shaft. ....	84
<i>Figure 4.8.</i> Surface experimental temperature measurements and experimental, CFD, and CFD linear profile in-shaft temperature results, from December 2020 to March 2021: a) air temperature in Eagle Creek vent shaft, b) air temperature in Eagle Creek drop shaft, c) air temperature in utility shaft No.3 shaft, and d) air temperature in screen shaft.....	85
<i>Figure 4.9.</i> Surface experimental water vapor mass fraction measurements and experimental, CFD, and CFD linear profile in-shaft water vapor mass fraction results, from December 2020 to March 2021: a) water vapor mass fraction in Eagle Creek vent shaft, b) water vapor mass fraction in Eagle Creek drop shaft, c) water vapor mass fraction in utility shaft No.3 shaft, and d) water vapor mass fraction screen shaft. ....	86
<i>Figure 4.10.</i> SCFM predictions for the DRTC+ECT alignment: a) cold conditions and b) warm conditions. ....	90
<i>Figure 4.11.</i> SCFM predictions for the DRTC+ECT+WRT+LPgRT alignment: a) cold conditions and b) warm conditions. ....	93
<i>Figure 4.12.</i> SCFM predictions for the DRTC+ECT+WRT+LPgRT+WRT alignment: a) cold conditions and b) warm conditions. ....	95

<i>Figure 4.13.</i> SCFM predictions for the DRTC+ECT+WRT+LPgRT+WRT+PRDT alignment: a) cold conditions and b) warm conditions. ....	98
-------------------------------------------------------------------------------------------------------------------------------------	----

## **LIST OF ABBREVIATIONS**

ACFM	Actual Cubic Feet per Minute
CEG	Citizens Energy Group
CFD	Computational Fluid Dynamics
CSO	Combined Sewer Overflow
CSS	Combined Sewer System
CWA	Clean Water Act
DRTC	Deep Rock Tunnel Connector
DS	Drop Shaft
EC	Eagle Creek
ECT	Eagle Creek Tunnel
FC	Fall Creek
FCT	Fall Creek Tunnel
LP	Lower Pogues
LPgRT	Lower Pogues Run Tunnel
PR	Pleasant Run
PRDT	Pleasant Run Deep Tunnel
RANS	Reynolds Average Navier-Stokes
SCFM	Standard Cubic Feet per Minute
SSS	Sanitary Sewer Systems
UDF	User Defined Function
USEPA	United States Environmental Protection Agency
WR	White River
WRT	White River Tunnel

## LIST OF SYMBOLS

$a$ – Adjustable factor (-), Vapor pressure model constant (Pa)	$P$ – Unwetted Perimeter ( $m$ ), Pressure ( $Pa$ )
$A$ – Clear water stream cross-sectional area ( $m^2$ )	$Q$ – Volumetric flow ( $m^3/s$ ), Volumetric heat generation ( $W/m^3$ )
$\vec{A}$ – Wall normal area vector ( $m^2$ )	$R$ – Radius ( $m$ )
$b$ – Vapor pressure model constant	$R_h$ – Air hydraulic radius ( $m$ )
$B$ – Multi-sample fixed bias	$S$ – Source term
$c$ – Vapor pressure model constant ( $^{\circ}C$ )	$S_0$ – Slope (-)
$C_c$ – Contraction coefficient (-)	$t$ – Thickness plate ( $m$ ), t-statistics
$C_p$ – Specific heat ( $kJ/kg \cdot K$ )	$T$ – Temperature (K)
$d_h$ – Hydraulic diameter single hole ( $m$ )	$U$ – X velocity component ( $m/s$ )
$D$ – Mass diffusivity ( $m^2/s$ )	$U_{\infty}$ – Free stream velocity ( $m/s$ )
$f$ – Friction factor (-)	$V$ – Velocity magnitude ( $m/s$ ), Y velocity component ( $m/s$ )
$g$ – Gravity ( $9.81 m/s^2$ )	$\vec{V}$ – Velocity vector ( $m/s$ )
$h$ – Enthalpy ( $kJ/kg$ )	$V_0$ – Clear water stream average velocity ( $m/s$ )
$H$ – Height difference ( $m$ )	$W$ – Wastewater surface width ( $m$ ), Z velocity component ( $m/s$ )
$k$ – Thermal conductivity ( $W/m \cdot K$ ), Turbulent kinetic energy ( $m^2/s^2$ )	$y$ – Stream height ( $m$ )
$K_L$ – Minor loss coefficient (-)	$Y$ – Mass fraction ( $kg/kg_{humidair}$ )
$K_{LS}$ – Minor loss coefficient single hole (-)	$y^+$ – Non-dimensional distance
$M$ – Molecular weight air ( $kg/K \cdot mol$ )	
$n$ – Number of samples (-)	

### Greek Symbols

$\alpha$  – Angle between approaching wind and tunnel axis (*rad*)

$\beta$  – Equivalent diameter ratio (-)

$\delta X_0$  – Zeroth order uncertainty

$\delta X_{fixed}$  – Single-sample fixed bias

$\delta X$  – Uncertainty

$\Delta P$  – Pressure difference (*Pa*)

$\Delta P_u$  – Ultra-static pressure difference (*Pa*)

$\Delta P_w$  – Ventilation wall pressure difference (*Pa*)

$\Delta P_t$  – Thermal potential pressure difference (*Pa*)

$\varepsilon$  – Turbulent dissipation rate ( $m^2/s^3$ ), Roughness height (*m*)

$\theta$  – Azimuthal angle (*rad*)

$\mu$  – Dynamic viscosity ( $kg/m \cdot s$ )

$\rho$  – Density ( $kg/m^3$ )

$\sigma$  – Standard deviation

$\tau$  – Condensation time scale (*s*)

$\varphi$  – Polar angle (*rad*)

### Subscripts

*abs* – Absolute

*atm* – Atmospheric

*avg* – Average

*drop* – Drop pressure

*e* – Energy equation

*h* – Hydraulic

*i* – Inside, Opening index, Instrument index

*l* – Liquid

*lat* – Latent of evaporation or sublimation

*m* – Mixture, Continuity equation

*open* – Open area

*ref* – Reference

$\rho v$  – Momentum equation

*s* – Static

*sat* – Saturation

*t* – Thermal

*total* – Total area

*u* – Ultra-static

*v* – Water vapor, Species equation

*w* – Wetted, Wind

*ws* – Water stream

*x* – X coordinate, Sample

$\bar{x}$  – Sample mean

*y* – Y coordinate

$z - Z$  coordinate



## GLOSSARY

**Combined sewage overflow (CSO) events:** Events where the combined sewer system cannot hold and transport more water. The overflowed water is discharged into water bodies to prevent the flow's backing into the streets (Citizens Energy Group [CEG], n.d.; USEPA, 1999).

**Combined sewer system (CSS):** Tunnels and pipes that transport the residential, commercial, industrial, sewage, and stormwater to treatment facilities in a single pipe (USEPA, 1999).

**Computational fluid dynamics (CFD) models:** Numerical models that use discretization methods to solve fluids dynamics partial differential equations using computers (Ferziger et al., 2020).

**Gravity sewer system:** The gravity sewers transport the wastewater taking advantage of the gravity (USEPA, 2002). The slope and diameter are selected to maintain a constant steady flow inside the sewer pipe (USEPA, 2002).

**In-shaft weather station:** Operational definition that describes the instrumentation installed in the vertical shafts of the tunnel. The instrumentation measures the vertical velocity, temperature, and humidity in the vertical shafts (author definition).

**Microclimate:** Local atmospheric conditions near the ground that are different from the surroundings' atmospheric conditions (Rosenberg et al., 1983).

**Natural ventilation:** Natural ventilation is the ventilation caused by the differences in elevation, temperature, wind speed, and air static pressure between the tunnel's openings (Madsen et al., 2006; Zhang et al., 2018).

**No-rain:** Operational definition that describes no rain in the atmospheric conditions.

**No-fill:** Operational definition that describes almost empty conditions of the DigIndy tunnel.

**Reynolds Average Navier Stokes (RANS) turbulence model:** Approximation method of the Navier Stokes equations, where the turbulent terms are averaged in time and space across all the turbulence spectrum (Ferziger et al., 2020; Hirsch, 2009). The turbulence structures and their effect in the average flow are modeled with empirical and semi-empirical models, e.g., turbulent kinetic energy – turbulent dissipation rate model ( $k - \epsilon$ ), or turbulent kinetic energy – specific rate of dissipation model ( $k - \omega$ ).

**Sanitary sewer system (SSS):** Tunnels and pipes that transport the residential, commercial, industrial, sewage, and limited amounts of stormwater to treatment facilities, in a single pipe (United States Environmental Protection Agency [USEPA], 2020a).

**Surface weather station:** Operational definition that describes the instrumentation installed at the surface level that measures atmospheric pressure, atmospheric temperature, atmospheric humidity, and wind speed (author definition).

**Sinking effect:** Operational definition that simplifies the interpretation of the stack effect or chimney effect for the study. The stack effect or chimney effect is the air movement produced by the temperature difference (Lowe, 2016). The temperature differences lead to a change in density in the air. The colder and denser gas tries to go in the same direction as the gravity. In contrast, the hotter and less dense gas tries to go in the opposite direction to the gravity, in this manner producing air circulation.

**Ventilation:** Exchange of air between the sewer atmosphere and the urban atmosphere (Madsen et al., 2006).

**Wind suction:** When wind crosses over sewer openings, it sucks out air from the sewer. The effect is also known as wind eduction (Madsen et al., 2006; Pescod & Price, 1982).

## **ABSTRACT**

The DigIndy tunnel is an extension of the Indianapolis combined sewer system that stores the combined sewer overflow during heavy rain conditions. The tunnel system has several openings in and around the city of Indianapolis. Gasses emitted from the tunnel may create health concerns and affect the quality of life for nearby residents. Understanding the air circulation patterns provides valuable insight into where gases are likely to emerge from the tunnel and what steps may be taken to mitigate gas emissions in undesirable locations. The objective of the present work is to develop a computational fluid dynamics (CFD) model capable of predicting the air circulation patterns in the DigIndy tunnel under dry weather conditions. In order to inform and validate the CFD model, an experimental campaign was designed and executed to measure weather data and air flow rates within the DigIndy tunnel. Obtaining accurate results requires careful consideration of key physical phenomena to include in the model, geometric simplification strategies, mesh generation strategies, and numerical modeling strategies. Results showed that the seasonal effect, manifest by thermally-driven flow, plays a significant role in the air circulation patterns within the tunnel. Furthermore, results show that tunnel alignment affects the natural air circulation within the tunnel. Large diameter shafts, as the working and retrieval shafts, lead to significant circulation rates in the new tunnel alignments.

## **CHAPTER 1. INTRODUCTION**

The understanding of the natural air circulation in the DigIndy tunnel is important to determine the behavior of sewer gases in the tunnel. This chapter introduces the project problem, purpose, and research questions. Next, a discussion of assumptions, delimitations, and limitations is presented. The chapter concludes with a list of definitions used throughout the document and an outline of the remainder of this document.

### **1.1 Introduction of the Problem and Purpose**

Combined sewer systems (CSS) transport a mixture of wastewater and stormwater from the cities to treatment facilities in a single pipe (Citizens Energy Group [CEG], n.d.; United States Environmental Protection Agency [USEPA], 1999). Under heavy rainfall conditions, the capacity of the CSS can be exceeded as a result of the larger volume of water from the wet weather (USEPA, 2004). When the CSS exceeds its capacity, combined sewage overflow (CSO) events occur (USEPA, 2004). The CSO is discharged into public water bodies to prevent overflowing the system and backing into the streets (CEG, n.d.; USEPA, 1999). To avoid the discharging of CSO into public waterways, several communities across the US implemented CSO capture systems to mitigate CSO's environmental impact (USEPA, 2004). The DigIndy tunnel is an extension of Indianapolis' CSS, which stores the combined sewage overflow during heavy rain seasons.

The DigIndy tunnel is a 5.5 m diameter, 43 km long tunnel underneath Indianapolis designed to capture, store, and transport 946 million liters of CSOs (CEG, n.d.; Kenyon, 2016). The transportation of wastewater and rainstorm water leads to pathogenic microorganisms and solid and gaseous pollutants inside the DigIndy Tunnel (Kim et al., 2009; USEPA, 1999, 2004). Pathogenic microorganisms such as E. Coli and intestinal viruses have been discovered in CSO systems (Kim et al., 2009). Such pathogens affect the aquatic environment and decline water quality, impacting communities' health (Kim et al., 2009; USEPA, 2004). Furthermore, the microorganism and pollutants inside the tunnel contribute to the formation of chemical compounds, i.e., hydrogen sulfide, generating safety and health concerns (Matias et al., 2017; Pescod & Price, 1982; Qian, 2018). Hydrogen sulfide gases create unpleasant odors, toxic and

deadly atmospheres in confined spaces, corrosion of sewer systems, and structural weakness (Matias et al., 2017). Intoxication for hydrogen sulfide is considered the mainly work-related cause of deaths in sewer system workers (Matias et al., 2017).

## **1.2 Problem Statement**

Ventilation modeling is an essential part of odor and corrosion studies in sewer systems (Lowe, 2016; Wang et al., 2012). Airflow circulation is required to estimate volatile compounds' dispersion and transportation (Madsen et al., 2006). Airflow estimations and volatile compound concentrations help develop odor and corrosion control strategies and technologies (Wang et al., 2012). The problem addressed by this study was the natural air circulation inside the DigIndy tunnel due to atmospheric conditions during dry weather conditions.

### **1.2.1 Significance of the Problem**

The DigIndy tunnel has up to 35 different openings across Indianapolis that help maintain adequate oxygen levels within the tunnel, controlling odor and corrosion (Madsen et al., 2006; Pescod & Price, 1982). Furthermore, the openings allow the venting of pressurized air from CSO discharges, avoiding geyser events in the tunnel (Qian, 2018). However, in dry weather conditions, the openings allow the venting of sewer gases from the tunnel to residential areas (Pan et al., 2020). In order to implement odor control strategies and technologies, there is a necessity to identify sewer gas venting locations and the flow characteristics (Lowe, 2016; Pan et al., 2020).

## **1.3 Purpose Statement**

The purpose of this research project was to better understand the physical phenomena that cause air circulation within the DigIndy tunnel network. Understanding the flow physics involves several aspects, such as understanding which forces affect the airflow, understanding how seasonal conditions affect the airflow, and understanding how the tunnel alignment affects airflow.

### **1.3.1 Significance of the Purpose**

The primary analysis tool used in the present work was computational fluid dynamics (CFD) modeling. Using CFD, the flow physics of natural air circulation was investigated under different seasonal conditions and different tunnel alignments. In order to use CFD as an analysis tool, it is critical to understand the forces affecting the airflow circulation. An accurate yet computationally inexpensive model must consider and model the most important effects and disregard the least essential effects. A validated computational model provides generalization and applicability for different seasonal conditions and different sewer system configurations (Pescod & Price, 1982; Qian, 2018; Ward et al., 2011).

Additionally to understanding the effect of seasonal conditions and tunnel alignment, the model may assist in identifying possible odorous locations that require mitigation strategies, e.g., air treatment facilities (Lowe, 2016; Ward et al., 2011). The developed natural air circulation model contributes to the understanding, restoration, and improvement of urban infrastructure (National Academy of Engineering, n.d.).

### **1.4 Research Questions**

As discussed in the previous sections, the present work aims to develop a CFD model to predict the natural air circulation in the DigIndy tunnel. The present study answers one question related to model development:

1. For developing a computational model to predict natural air circulation in CSO storage tunnels, what physical phenomena must be included in the model and what phenomena may be disregarded?

Furthermore, the study answers two questions related to the application of the CFD model to the specific geometry and environmental conditions of the DigIndy tunnel:

2. What is the effect of seasonal conditions in the natural air circulation in the DigIndy tunnel?
3. What is the effect of different alignment configurations in the natural air circulation in the DigIndy tunnel?

The first research question was addressed in two steps. First, by carrying out a diligent literature review looking for the most important forces affecting the air circulation in sewer systems. Second, installing field measurements outside and inside the first DigIndy tunnel alignment to measure the most important parameters for air circulation determined in the literature review.

The second research question was addressed by analyzing the field measurements and exercising the CFD model. The third research question was addressed by exercising the CFD model for the different stages of the DigIndy tunnel.

### **1.5 Assumptions**

In order to simplify the development of the CFD model, several assumptions were made:

- The temperature in the tunnel's wall was assumed constant with a value of 12.78 °C (O. Hawbaker, personal communication, September 30, 2019; Kusuda & Achenbach, 1965).
- Heat conduction within the tunnel wall was neglected. The tunnel's wall was considered adiabatic.
- The average atmospheric conditions in a time segment large than two days without rain were considered the representative atmospheric conditions for the dry weather conditions of each month.
- Representative atmospheric conditions were assumed as steady-state conditions. No time-dependent variation was considered.
- The tunnel has a constant stream of clear water at the bottom (O. Hawbaker, personal communication, September 30, 2019). The effect of this stream on the airflow within the tunnel was modeled as a moving wall. The moving wall captures the shear stress between the two fluids, such that the stream drags the air in the direction of water motion. Multiphase effects, such as shear stress within the water phase, e.g., waves, were not considered.
- The humid airflow inside the DigIndy tunnel was modeled as a single-phase fluid. For the real system, liquid water droplets may be created from wall condensation and bulk condensation. Two-phase flow effects were not considered. However, heat and mass transfer due to evaporation and condensation were accounted.

- Mass transfer effects were considered by modeling the humid air as two species: dry air and water vapor.
- Water vapor was the only species transported by the air. Hydrogen sulfide and other trace gases were not considered.
- The geometric representation of the connection and openings of the system was simplified. Not all of the openings to the atmosphere were accounted for, e.g., diversion chambers. Only the shafts directly connected to the atmosphere were modeled.
- Tunnel sections without any shaft directly connected to the atmosphere were neglected.

### **1.6 Delimitations**

The work aimed to study the natural air circulation in the DigIndy tunnel during dry weather conditions. The following list of the project's delimitations was based on the study's purpose.

- Rain times were not considered in the atmospheric conditions (no-rain conditions).
- The DigIndy tunnel was analyzed under almost empty conditions (no-fill conditions). Only a clear water stream of 750 GPM ( $4.732 \times 10^{-2} \text{ m}^3/\text{s}$ ) was accounted for in the tunnel's bottom (O. Hawbaker, personal communication, September 30, 2019). The clear water stream is produced by water leaks inside the tunnel (O. Hawbaker, personal communication, September 30, 2019).
- Only steady-state scenarios were analyzed.
- Drop structures' transient effects were not modeled since no-rain conditions were analyzed.

### **1.7 Limitations**

Because the present work relied on field data and depended on the current status of the partially completed DigIndy tunnel, there are several limitations to this work that could not be controlled. The limitations are:

- The current status of the DigIndy tunnel is that only the initial alignment (DRTC+ECT) is operational. Therefore, field data could only be collected for this alignment, and the CFD model was only validated against it. It would be preferable to collect field data and



validate the CFD model against multiple alignments to ensure that the model is accurate and generalizable to a wide range of cases.

- Not all the effects affecting the air circulation inside the tunnel were known. For instance, after CSO events, sand, rocks, tree branches, or larger object can sediment at the bottom of the tunnel (Crabtree, 1989; Murali et al., 2020). Accumulation of sediments reduces flow in the sewer systems (Crabtree, 1989). The objects in the tunnel's bottom will create a blockage, augmentation of the shear stress, or gas emission that will affect air circulation inside the tunnel.
- For no rain conditions, water entry to the DigIndy tunnel through CSO connections cannot be controlled.
- No records of pump activation in the treatment plan were available. The pump activations can induce an airflow that cannot be controlled.

### **1.8 Summary**

The DigIndy tunnel is an extension of DigIndy's combined sewer system to store and transport the CSO (CEG, n.d.). During no-rain conditions, odors are generated inside the tunnel and can escape through the system's different openings, causing safety and health concerns (Pescod & Price, 1982; Qian, 2018). The purpose of this project was first to understand the most important effects influencing the natural air circulation in the DigIndy tunnel; second, to understand the effect of seasonal conditions in the natural air circulation; and third, to explain the effect of different alignment configurations. The CFD model provides insight into the physics of the natural air circulation, and it will be employed as a ventilation tool (Lowe, 2016; Ward et al., 2011).

The literature was reviewed to understand the most relevant effects driving air circulation in sewer systems. The project experimentally measured the temperature, atmospheric pressure, humidity, and air velocity in several tunnel openings. The measurements were used as boundary conditions for the CFD model and to validate the CFD model predictions.

## **CHAPTER 2. REVIEW OF LITERATURE**

The factors affecting air circulation in sewer systems and previous modeling of efforts must be examined to develop the natural air circulation model. Chapter two summarizes the findings pertaining to the project's problem and purpose. Furthermore, the chapter summarizes the methodology used in previous studies that give insight into the methodology used in the problem considered in the present work. The chapter ends with a statement on the uniqueness of the study and a summary of the findings.

### **2.1 Findings Pertaining to the Problem and Purpose.**

The USEPA established the Clean Water Act (CWA) to regulate the discharge of pollutants into water bodies and stated the standards for surface water quality in the United States in 1972 (USEPA, 2020b). Several cities across the midwest that used CSS were mandated to create solutions to mitigate the impact of CSO in water bodies complying with the CWA (USEPA, 2004). The city of Indianapolis proposed the construction of the DigIndy tunnel to mitigate the impact of the CSO events (CEG, n.d.). The DigIndy tunnel stores the CSO and transports the wastewater to a treatment plant where the wastewater is treated before it is disposed of in the water bodies (CEG, n.d.).

The presence of hydrogen sulfide, viruses, and bacteria in CSS systems has been a concern in several cities worldwide due to several negative impacts: repercussion on the aquatic environment (Kim et al., 2009), sewer structure integrity and corrosion (Liang et al., 2019; Madsen et al., 2006; Matias et al., 2017), nuisance odors (Liang et al., 2019; Pan et al., 2020) and in more significant concentration, toxicity (Matias et al., 2017).

Kim et al. (2009) studied the diurnal fluctuation of organic suspended solids, volatile suspended solids, chemical compounds, intestinal viruses, and E. coli bacteria transported by the CSS system in Chiba, Japan. Organic suspended solids, volatile suspended solids, and chemical compounds showed the same diurnal fluctuations having a large concentration in the morning (7:00 am), maintaining constant from noon to midnight, and declining to the lower concentration at 5:00 am (Kim et al., 2009). On the other hand, E.coli bacteria and intestinal viruses showed variable patterns and, in some cases, exceed the concentration of bacteria and chemical

compounds (Kim et al., 2009). Matias et al. (2017) studied the generation of hydrogen sulfide for high turbulence conditions during the wastewater discharge in the city of Ericeira sewer system in Portugal. They found that a high sulfide concentration can be measured downstream of the drop structure after a wastewater discharge (Matias et al., 2017). However, the concentration reduced over the time after the event (Matias et al., 2017). Furthermore, they found that manholes in vertical shafts with drop structures presented higher levels of corrosion than manholes in vertical shafts without drop structures (Matias et al., 2017).

Liang et al. (2019) studied the formation of hydrogen sulfide in the mega-size deep tunnel sewer system in Hong Kong. Liang et al. (2019) found that hydrogen sulfide production was up to 1410 kg per day. They found that sections of the tunnels with the largest sewage flow rates and retention time contribute 89% of the hydrogen sulfide production. Furthermore, increments in temperature and the addition of organic wastes increase hydrogen sulfide production (Liang et al., 2019). However, rainy conditions were found to reduce hydrogen sulfide production (Liang et al., 2019).

One extensive statistical study of odor complaints and the relation with sewer system attributes was carried out by Pan et al. (2020). Pan et al. (2020) performed a statistical analysis of Edmonton, Canada's odor complaint records from 2008 to 2017. They analyzed the statistical relation between the weather conditions, sewer section age, material, presence of drop shaft structures, type of sewer system (combined or sanitary sewer), and pipe slope with the number of complaints. Snow melting and raining events were statistically related to fewer complaints due to the carrying and displacement of the organic compounds inside the tunnel (Pan et al., 2020). However, after rainy months, complaints were increased due to the sedimentation of organic compounds previously carried by the stormwater (Pan et al., 2020). Sewer system age showed a positive relationship with the number of complaints (Pan et al., 2020). Combined sewer systems showed more complaints than sanitary sewer systems (Pan et al., 2020). Drop shaft structure correlated with a higher number of complaints than the sewer sections without it (Pan et al., 2020). Finally, the pipe slope did not significantly correlate with the number of complaints (Pan et al., 2020).

Since the DigIndy tunnel storages and transports the wastewater from the CSO, the presence of chemical compounds, intestinal viruses, and bacteria in the tunnel is awaited (Kim et al., 2009). After rain episodes, in dry weather periods, the emission of sewage gases is expected

to increase from the tunnel (Liang et al., 2019; Pan et al., 2020). The emission of sewage gases such as hydrogen sulfide is a health concern for the Indianapolis inhabitants and affects the tunnel's integrity (Liang et al., 2019; Matias et al., 2017). Understanding the natural air circulation in the DigIndy tunnel allows the creation of ventilation tools to identify odor emission openings and identify hydrogen sulfide concentration location that potentially leads to corrosion of the tunnel structure (Liang et al., 2019; Lowe, 2016).

## **2.2 Findings Pertaining to the Methodology.**

### **2.2.1 Relevant Factors for Air Circulation in Sewer Systems**

Several authors have identified and studied the most relevant factors driving the air circulation in sewer systems (Lowe, 2016; Madsen et al., 2006; Olson et al., 1997; Pan et al., 2020; Parker & Ryan, 2001; Pescod & Price, 1982). The following list summarizes these major factors:

- Liquid drag: The drag force exerted by the wastewater surface to the headspace air creates an air movement inside the tunnel.
- The sewage level fluctuation: Fluctuations in the sewage level ingest air throughout the openings to the tunnel if the sewage level is reduced or exhaust air if the sewage level is raised.
- Buoyancy (thermally-driven): The temperature difference between the atmosphere temperature and the internal tunnel temperature creates a difference of density that leads to air buoyancy forces. If the temperature outside the tunnel is colder than inside the tunnel, the air sinks inside the tunnel. The sinking phenomenon is known as the stack or chimney effect (Lowe, 2016).
- Buoyancy (species-driven): Humid air has less density than dry air (Çengel et al., 2019; Lowe, 2016). Since the humid air inside the tunnel tends to be more humid, differences in density create buoyancy forces that sink the air inside the tunnel (Lowe, 2016).
- Pressure differences: Difference of pressure due to barometric and static pressure fluctuations drives the airflow from the location with higher pressure to the location with lower pressure.

- Wind speed: Wind speed differences across the sewer system openings create suction or pressurization of the openings. Wind blowing perpendicularly over the sewer system openings sucks out air from the system (Pescod & Price, 1982).
- Drop structures: Drop structures introduce a massive amount of air when CSO is transported throughout them (Lowe, 2016; Pan et al., 2020).
- Siphon structures: Siphon structures block sewer sections, not allowing the circulation of the air (Lowe, 2016; Madsen et al., 2006).

All the effects mentioned above were considered in this study, except for the sewage level, drop structures, and siphons structures. The sewage level is not considered due to the delimitation of no-fill conditions in the DigIndy tunnel (p. 24). The drop structures are not considered because the structures only introduce significant air when there are CSO events during rain conditions. Lastly, no siphon structures are presented in the DigIndy tunnel; therefore, the siphon structure effect is discarded.

### **2.2.2 Ventilation Modeling for Sewer Systems**

The ventilation modeling tools can be divided into empirical models, theoretical models, and computational models (Apgar & Witherspoon, 2009; Lowe, 2016). Ventilation modeling efforts have been carried out for several authors in order to separately study the different factors affecting the air circulation in sewer systems (Edwini-Bonsu & Steffler, 2006; Olson et al., 1997; Pescod & Price, 1982; Qian et al., 2017; Wang et al., 2012).

Pescod and Price (1982) studied the suction effect of perpendicular wind passing a sewer opening for different opening terminals. Moreover, they studied the drag force exerted by the wastewater for different sewage levels. They tested three different opening terminals for wind suction: a venturi extractor, a slotted extractor terminal, and a plain open. Figure 2.1 shows the geometrical configuration of each extractor terminal. They found that the venturi extractor increases the airflow sucked out up to 53%, and the slotted extractor increases the airflow educted up to 33%, both with respect to the plain open terminal.

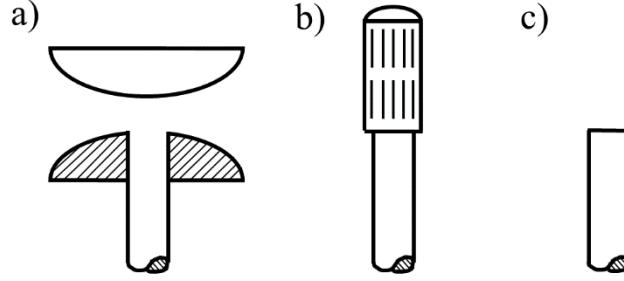


Figure 2.1. Schematic of opening geometries considered by Pescod and Price (1982): a) venturi extractor, b) slotted extractor, and c) plain open.

Based on laboratory experiments and the different extractor terminals, Pescod and Price (1982) defined an empirical model to predict the volumetric flow educted by the wind from the sewer system. Equation 2.1 shows the empirical formulation where  $U_{\infty}$  is the free stream velocity passing across the terminals, and “ $a$ ” is an adjustable factor that accounts for the terminal type.

$$Q = 0.01394 \cdot \frac{U_{\infty}}{a^2} - 1 \text{ (m}^3/\text{s)} \quad (2.1)$$

The authors also performed several experiments in an inclined pipe to measure the air headspace velocity (Pescod & Price, 1982). They found that the air velocity measured in the headspace is affected by the surface velocity of the wastewater and correlates well with the unwetted perimeter of the pipe and the hydraulic fluid radius (Pescod & Price, 1982). The air headspace velocity relates with the unwetted velocity, as is shown in Equation 2.2 and the hydraulic fluid radius correlates with the velocity as is shown in Equation 2.3. Lastly, in their experiments, they found that the velocity induced by the wastewater and the wind suction effect is not additive in all the cases (Pescod & Price, 1982).

$$V_{air} = F \left( \frac{WV_s}{P} \right) \quad (2.2)$$

$$V_{air} = F \left( \frac{WV_s}{R_h} \right) \quad (2.3)$$

Olson et al. (1997) study the air circulation in a multiphase industrial sewer where hot effluents are discharged. Olson et al. (1997) developed a theoretical model using fundamental fluid mechanics and heat transfer relations. The liquid drag, buoyancy forces, convection heat

transfer, evaporation, radiative heat transfer, and wind suction were described using known theoretical equations (Olson et al., 1997). The theoretical model was validated against laboratory experiments (Olson et al., 1997). Wind suction and buoyancy forces were the most important factors for air circulation in multiphase industrial sewers (Olson et al., 1997).

Edwini-Bonsu & Steffler (2006) developed a 3D CFD finite element model to calculate the fully developed steady-state airflow in a sewer system pipe due to the wastewater drag force and pressure gradient. The pipe's wall was considered smooth, and the flow was considered fully developed (Edwini-Bonsu & Steffler, 2006). The authors modeled the turbulence base on the eddy viscosity concept to simulate turbulence-driven secondary currents (Edwini-Bonsu & Steffler, 2006). The CFD model estimated the velocity distribution in the headspace cross-sectional area of the pipe for different sewage levels (Edwini-Bonsu & Steffler, 2006). The model predictions were validated against experimental results. With the model and experimental results, relations to calculated air headspace velocity as a function of longitudinal pressure gradients, wastewater velocity, and sewer headspace were established (Edwini-Bonsu & Steffler, 2006).

Wang et al. (2012) develop a 1D CFD compressible finite element model to calculate the forced ventilation in the North Head Sewerage Ocean Outfall system in Sidney, Australia. Wang et al. (2012) link the air finite element model to the Model for Urban Sewers (MOUSE) hydraulic model to estimate the transient air circulation in the sewer system. Wastewater velocities and sewage level is simulated by the MOUSE model and are used as inputs for the air finite element model (Wang et al., 2012). Qian et al. (2017) simulate a 3D multiphase flow of water and air in a straight pipe and in a pipe with a slope change using ANSYS CFX. Qian et al. (2017) analyzed the velocity profiles produced by the hydraulic jump generated by the slope. The model prediction was compared against experimental results (Qian et al., 2017). Prediction for air circulation during the hydraulic jump was overestimated but agreed when the hydraulic jump was high enough to partially seal the headspace (Qian et al., 2017).

The empirical models are the simplest models to estimate airflow in sewer systems (Apgar & Witherspoon, 2009). However, empirical relations are subjected to the simplifications in which the models were established because they represent specific controlled cases and do not reflect real-world variations (Apgar & Witherspoon, 2009). Moreover, the inclusion of multiple effects, such as wind suction, wastewater drag, pipe roughness, minor pressure losses, and

blockages, are not necessarily additive, requiring reformulation of the empirical models (Pescod & Price, 1982). Theoretical models can account for multiple effects; however, adding effects adds complexity to the model, making the model more difficult to apply (Apgar & Witherspoon, 2009). With the increment of theoretical equations, their relation can become complex, requiring iterative processes that are time-consuming (Apgar & Witherspoon, 2009).

On the other hand, CFD models can incorporate multiple theoretical models in a single framework and solve the iterative calculations using computational resources (Ferziger et al., 2020). The inclusion of multiple effects such as wastewater drag, wind suction, pipe roughness, minor pressure losses, complex structures, and different sewer system configurations can be achieved using CFD models. For the former reasons, due to the complex geometries presented in the DigIndy tunnel, e.g., bulkheads, bifurcation, no constant pipe geometry in vertical shafts, the CFD model was selected as the modeling tool to develop the natural air circulation DingIndy tunnel model.

### 2.2.3 Natural Air Circulation in Long Tunnels

Due to the diameter (5.5 m) and length (43 km) of the DigIndy tunnel, natural air circulation in extra-long tunnels was found of interest for this study (Guo et al., 2016, 2017; Zhang et al., 2018). Guo et al. (2017) defined that the major factors affecting the natural air circulation in straight tunnels are the “ultra-static pressure difference ( $\Delta P_u$ ),” the “thermal potential pressure difference ( $\Delta P_t$ ),” and the “ventilation wall pressure difference ( $\Delta P_w$ )” (p. 3). The pressure difference between the two openings is defined as the sum of the different pressure differences, as is shown in Equation 2.4.

$$\Delta P = \Delta P_u + \Delta P_w + \Delta P_t \quad (2.4)$$

Figure 2.2 shows a schematic example of the properties affecting the natural air circulation in an inclined straight tunnel. The positions at the left and right of the tunnel, points 1 and 2, are external to the tunnel, and the conditions at these points represent the conditions outside the tunnel at the two openings.



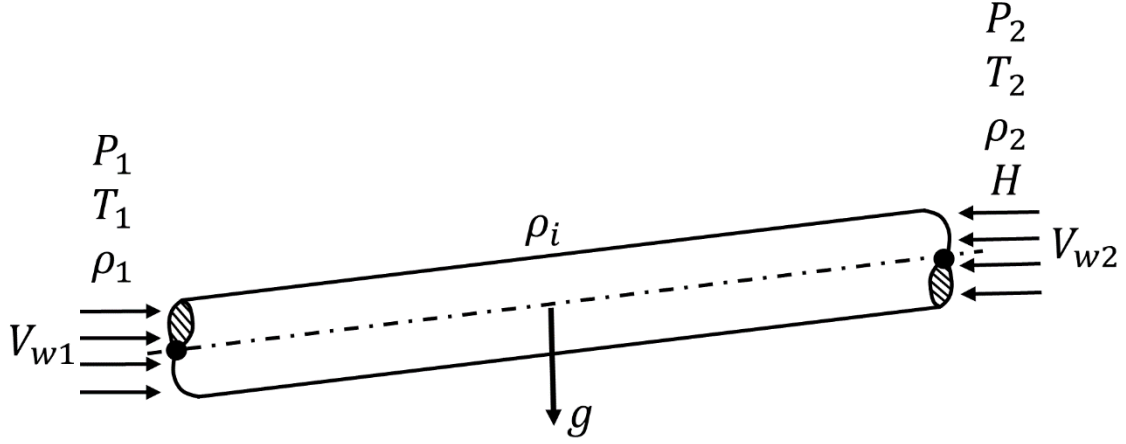


Figure 2.2. Schematic of parameters affecting the natural air circulation in extra-long inclined straight tunnels.

The ultra-static pressure difference is defined as the difference of pressure due to air movement from one opening to another and due to the resistance exerted by the body force of the air (Guo et al., 2016, 2017; Zhang et al., 2018). Equation 2.5 shows an example calculation using the nomenclature used in Figure 2.2, where  $\rho_i$  is the air density inside the tunnel, where location 2 is considered the reference.

$$\Delta P_u = P_1 - P_2 - \rho_i g H \quad (2.5)$$

The thermal potential pressure is defined as the pressure exerted by the density difference between the atmosphere and the tunnel, as shown in Equation 2.6.

$$\Delta P_t = (\rho_{avg} - \rho_i) g H \text{ where } \rho_{avg} = \frac{\rho_1 + \rho_2}{2} \quad (2.6)$$

Lastly, the ventilation wall pressure difference is defined as the dynamic pressure difference exerted by parallel winds entering the tunnel. Equation 2.7 shows an example calculation using the nomenclature used in Figure 2.2, where  $K_L$  is the entrance minor loss coefficient of each tunnel entrance, and  $\alpha$  is the angle between the approaching wind velocity vector and the tunnel axis. For a vertical shaft with flow passing horizontally,  $\alpha = 90^\circ$ , the ventilation wall pressure is zero. If the wind velocity vector is pointing into the tunnel, the ventilation pressure is positive.

$$\Delta P_w = \frac{1}{2} K_{L1} \rho_1 (V_{w1} \cos(\alpha_1))^2 - \frac{1}{2} K_{L2} \rho_2 (V_{w2} \cos(\alpha_2))^2 \quad (2.7)$$

The total pressure difference between the tunnel entrance can be used to calculate the airflow inside the tunnel using viscous theory flow in pipes (White, 2017). Zhang et al. (2018) use the former methodology to set up the boundary conditions for a 3D CFD model of the Yunshan tunnel in Shanxi Province, China, using ANSYS FLUENT (Zhang et al., 2018). The methodology used to calculate the natural air circulation in extra-long tunnels and the significant factors affecting the air circulation in sewer systems are the basement to develop and configure the natural air circulation model of the DigIndy tunnel.

### **2.3 Uniqueness of the Present Work**

The studies found in the literature address the air circulation in sewer systems with partial-fill conditions (Edwini-Bonsu & Steffler, 2006; Olson et al., 1997; Pescod & Price, 1982; Qian et al., 2017; Wang et al., 2012). The water drag force was the most significant factor driving the air circulation in sewer systems in multiple studies (Lowe, 2017; Madsen et al., 2006; Parker & Ryan, 2001; Pescod & Price, 1982). Except for Olso et al. (1997), which found buoyancy force and wind suction the most important factors in industrial sewers.

For the study, the DigIndy tunnel natural air circulation was considered under no-rain no-fill conditions, making wind suction, buoyancy force, and pressure difference factors more important than the water drag force. Additionally, the studies found in the literature addressed airflow circulation in CSSs and not in storage tunnels. Structural characteristics of the DigIndy tunnel, e.g., 5.5 m tunnel diameter and 43 km length, made the study of this type of system unique. Lastly, a one-year campaign of microclimate measurements across the DigIndy tunnel makes this work an extensive resource for future works where atmospheric conditions from the city of Indianapolis will be required.

### **2.4 Summary**

The emission of sewage gases from CSS has been a concern in several cities worldwide (Kim et al., 2009; Liang et al., 2019; Matias et al., 2017; Pan et al., 2020). The hydrogen sulfide presented in CSS can create nuisance odors, generate health concerns, and cause toxicity in large

concentrations (Matias et al., 2017; Pescod & Price, 1982; Qian, 2018). Furthermore, hydrogen sulfide's presence deteriorates the sewer system structures, creating corrosion problems (Liang et al., 2019). Ventilation models can identify venting openings where sewage gases can leak to the atmosphere and locations where hydrogen sulfide can concentrate (Liang et al., 2019; Lowe, 2016).

Three different types of ventilation models exist, empirical models, theoretical models, and computational models (Apgar & Witherspoon, 2009; Pan et al., 2020). Empirical models are based on experimental correlations (Pescod & Price, 1982), theoretical models are based on fluid mechanics and heat transfer fundamentals (Olson et al., 1997), and computational models are based on mathematical algorithms solve by computers (Edwini-Bonsu & Steffler, 2006; Qian et al., 2017). Almost all the ventilation modeling focused on partially fill conditions where the effect of the drag force exerted by the wastewater and the difference in pressure in the air circulation are the most important factors affecting the air circulation (Apgar & Witherspoon, 2009; Edwini-Bonsu & Steffler, 2006; Qian et al., 2017; Wang et al., 2012; Ward et al., 2011). The natural air circulation model for the DigIndy tunnel considers no-fill conditions, having not a significant wastewater drag force.

Due to the geometrical characteristics of the DigIndy tunnel and the no-fill conditions, natural air circulation in extra-long tunnels was of interest for the study purpose. The primary effects affecting the natural air circulation in extra-long tunnels are the ultra-static pressure difference, the thermal potential pressure difference, and the ventilation wall pressure difference (Guo et al., 2016, 2017; Zhang et al., 2018). A modification of the methodology used for extra-long tunnel natural air circulation was used to develop the natural air circulation model for the DigIndy tunnel. The model included the major effects on the air circulation in sewer systems. The methodology used in this project is explained in the following chapter.

## **CHAPTER 3. RESEARCH METHODOLOGY**

The presented project aimed to understand the forces affecting airflow circulation in the DigIndy tunnel for different seasonal conditions and different tunnel alignments. This chapter includes the description of the DigIndy tunnel characteristics and alignments, the experimental procedure, and the numerical modeling procedure.

### **3.1 Introduction of the Research Methodology**

The study consisted of two types of research: quasi-experimental research and developmental research. The quasi-experimental research was carried out to measure the microclimate weather conditions and airflow conditions across the different tunnel openings of the initial tunnel alignment. The developmental research consisted of developing a CFD model to predict the natural air circulation in the DigIndy tunnel.

The field measurements were used as inputs to configure the CFD model as well as to validate the CFD predictions for the initial alignment. The model incorporates the most important effects in natural air circulation. After validation, the model is used to predict the natural air circulation for different tunnel alignment configurations.

### **3.2 DigIndy Tunnel**

The DigIndy tunnel is an extension of Indianapolis' combined sewer system (CEG, n.d.). The tunnel will have an extension of approximately 43 km after the end of its construction in 2025 (CEG, n.d.; Kenyon, 2016). The tunnel is constructed beneath the city of Indianapolis at a depth between 60 – 70 m. As the gravity sewer system, the tunnel has a constant slope of 0.1% towards the pump station, allowing wastewater flow for gravity. The DigIndy tunnel is divided into six tunnel segments: the Deep Rock Tunnel Connector (DRTC), the Eagle Creek Tunnel (ECT), White River Tunnel (WRT), Lower Pagues Run Tunnel (LPgRT), Fall Creek Tunnel (FCT), and Pleasant Run Deep Tunnel (PRDT) (CEG, n.d.; Kenyon, 2016). Figure 3.1 shows the final tunnel layout over the Indianapolis map. Figure 3.1 shows the different alignments and their CSO collectors, utility shafts, vent openings, working shaft, and retrieval shaft locations. Information regarding the structural characteristics of the tunnel was provided by CEG. A

portion of Figure 3.1 is masked to illustrate that only the DRTC+ECT segments are operational as of this writing. The other segments are future alignments of the DigIndy tunnel, and they are described in the upcoming sections.

### **3.2.1 Initial Alignment (DRTC+ECT)**

The tunnel's initial alignment was completed in 2017. The initial alignment consists of two segments: DRTC + ECT (CEG, n.d.). The initial alignment has an extension of approximately 15 km (Kenyon, 2016). The portion of Figure 3.1, which is not masked, shows a schematic of the initial alignment with all the different connections and shafts connected to it. These connections and shafts include CSO collectors, venting shafts, utility shafts, and working shaft locations.

As mentioned in the assumptions (p. 23), only the openings directly connected to the atmosphere were considered. Figure 3.2.a shows a schematic of the alignment DRTC+ECT with the three openings communicated directly with the atmosphere: Eagle Creek, utility shaft No.3, and screen shaft. The Eagle Creek location has two shafts, the Eagle Creek vent shaft and the Eagle Creek drop shaft. The Eagle Creek drop shaft is located to the north of the location, and the Eagle Creek vent shaft is located to the south. The initial alignment is isolated from the rest of the tunnel by two bulkheads located upstream in CSO 118 and CSO 117. The black rectangles in Figure 3.2.a represent the bulkhead locations.

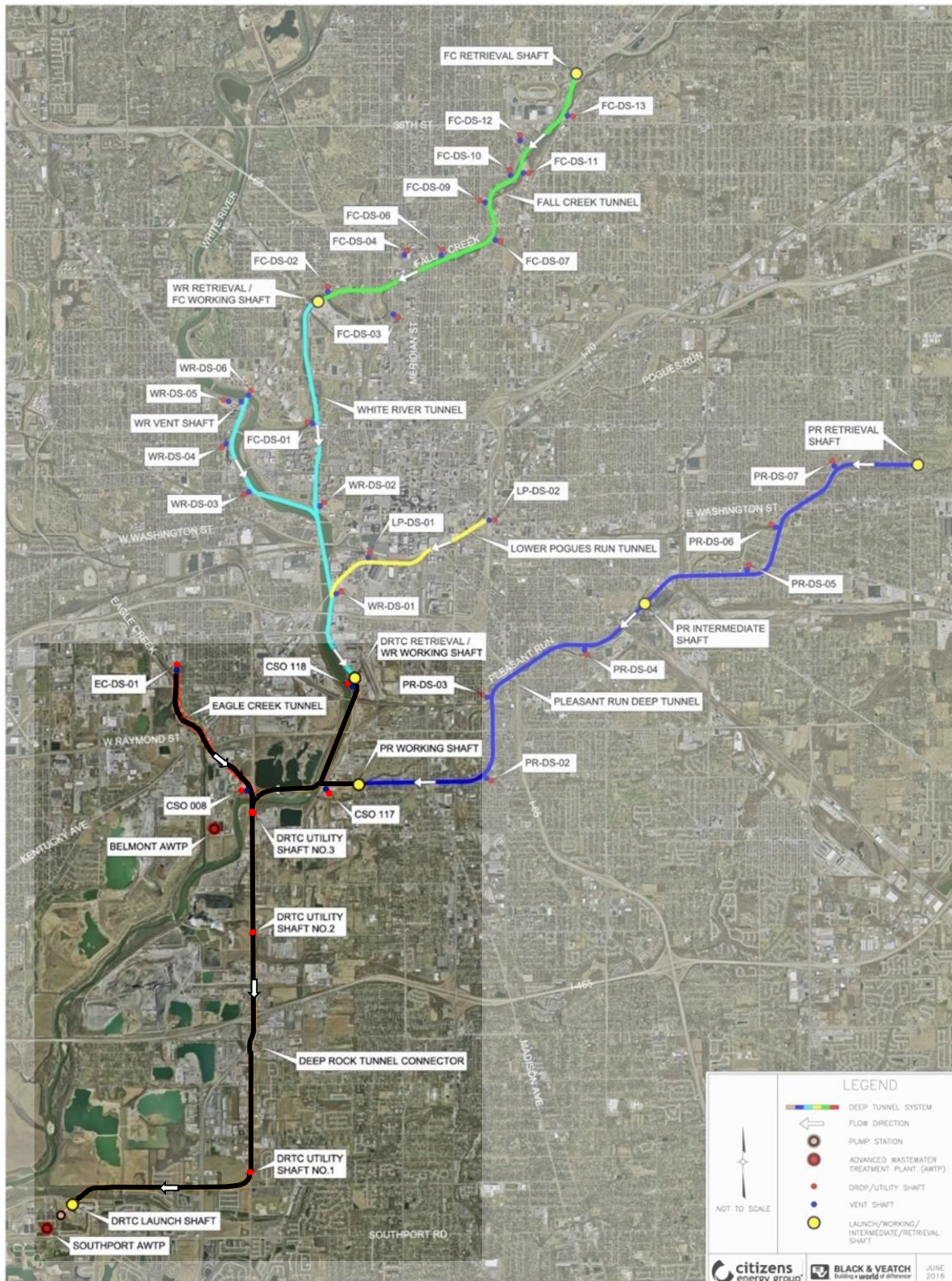
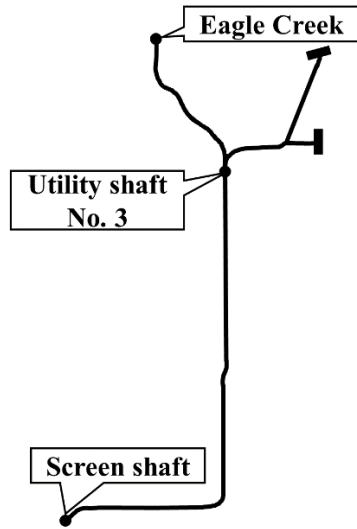
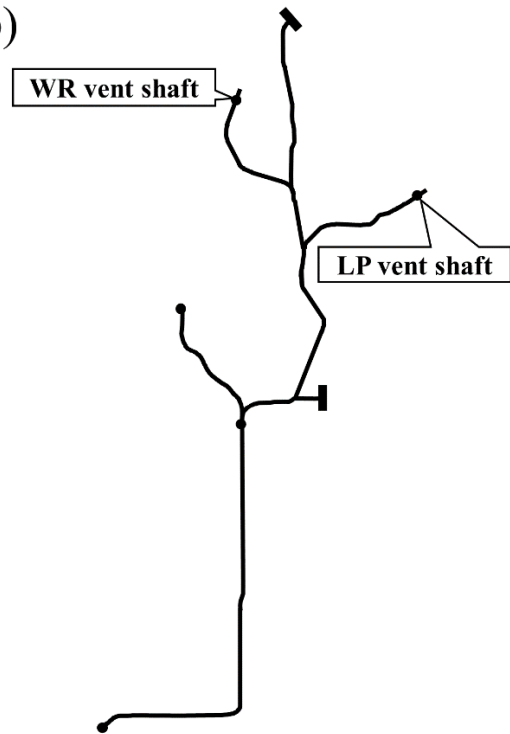


Figure 3.1. DigIndy final tunnel layout over Indianapolis map. *Note.* Black schematic lines represent DRTC+ECT tunnel alignment. Edited from “DigIndy tunnel layout [Handout],” by Citizens Energy Group, 2016. Reprinted with permission.

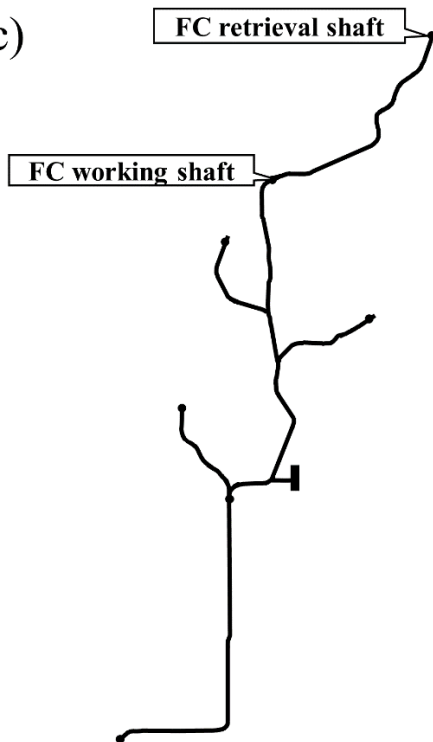
a)



b)



c)



d)

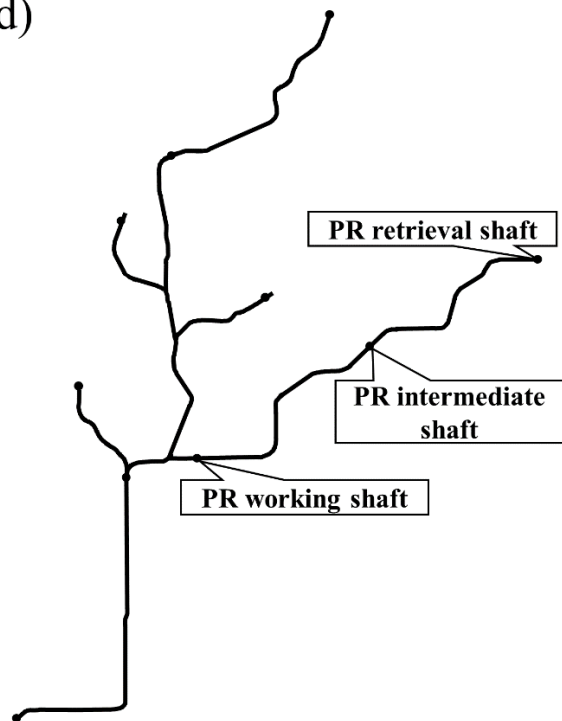


Figure 3.2. DigIndy tunnel alignments with the atmosphere openings: a) DRTC+ECT, b) DRTC+ECT+WRT+LPgRT, c) DRTC+ECT+WRT+LPgRT+WRT, and d) DRTC+ECT+WRT+LPgRT+WRT+PRT. *Note.* Black rectangles represent bulkhead locations.



### **3.2.2 Second Alignment (DRTC+ECT+WRT+LPgRT)**

The second alignment is to be completed at the end of 2021 (CEG, n.d.). The alignment consists of the initial alignment plus WRT+LPgRT (CEG, n.d.). The alignment has an extension of approximately 26 km (Kenyon, 2016). Two more openings are added in addition to the openings in the initial alignment. Figure 3.2.b shows a schematic of the second alignment with the two extra openings: LP vent shaft and WR vent shaft. The alignment is separated from FCT and PRDT by the bulkheads shown in Figure 3.2.b.

### **3.2.3 Third Alignment (DRTC+ECT+WRT+LPgRT+FCT)**

The third alignment is to be completed in 2025 (CEG, n.d.). The alignment consists of the second alignment plus FCT (CEG, n.d.). The alignment has an extension of approximately 32 km (Kenyon, 2016). Additionally to the openings in the initial and second alignment, two more openings are added. Figure 3.2.c shows a schematic of the third alignment with the two extra openings: FC working shaft and FC retrieval shaft. The alignment is separated from PRDT by the bulkhead shown in Figure 3.2.c.

### **3.2.4 Fourth Alignment (DRTC+ECT+WRT+LPgRT+FCT+PRDT)**

The fourth alignment is to be completed in 2025 (CEG, n.d.). The alignment has an extension of approximately 43 km and represents the DigIndy tunnel final extension (Kenyon, 2016). Figure 3.2.d shows a schematic of the fourth alignment with the three extra openings added: PR working shaft, PR intermediate shaft, and PR retrieval shaft. The final extension of the DigIndy tunnel has ten openings directly connected to the atmosphere.

### **3.2.5 DigIndy Tunnel Openings**

All the openings presented in Figure 3.2 are vertical shafts with diameters ranging between 2.438 to 12.192 m. However, utility shaft No.3 has an opening reduction from a cylindrical shaft of diameter 2.44 m to a rectangular opening of 1.22 m by 1.40 m, and the screen shaft has a reduction from a cylindrical shaft of diameter 13.441 m to an irregular opening with an approximately hydraulic diameter of 3.264 m. Table 3.1 presents the hydraulic diameter and area of the openings shown in Figure 3.2.



Table 3.1. Hydraulic diameter and the total opening area of openings.

Opening	$D_H$ (m)	$A(m^2)$
Screen shaft	3.264	12.968
Utility shaft No.3	1.305	1.711
Eagle Creek vent shaft	2.438	4.668
Eagle Creek drop shaft	2.438	4.668
LP vent shaft	2.438	4.668
WR vent shaft	2.438	4.668
FC working shaft	9.144	65.669
FC retrieval shaft	9.144	65.669
PR working shaft	12.192	116.745
PR intermediate shaft	9.144	65.669
PR retrieval shaft	9.144	65.669

### **3.3 Experimental Procedure**

Instrumentation was installed in the three openings of the DigIndy initial alignment shown in Figure 3.2.a. Two instrumentation sets were used in each location. The first set of instrumentation was placed on the surface to measure the atmospheric humidity, precipitation, atmospheric pressure, atmospheric temperature, and wind speed outside the tunnel (surface weather station). The second set of instruments measured the vertical shaft's velocity, temperature, and humidity (in-shaft weather station). The surface measurements were used to inform the CFD model's boundary conditions, and the in-shaft measurements were used to validate the CFD model. Figure 3.3 shows a flow diagram detailing the relationship between the experimental measurements and the CFD model.

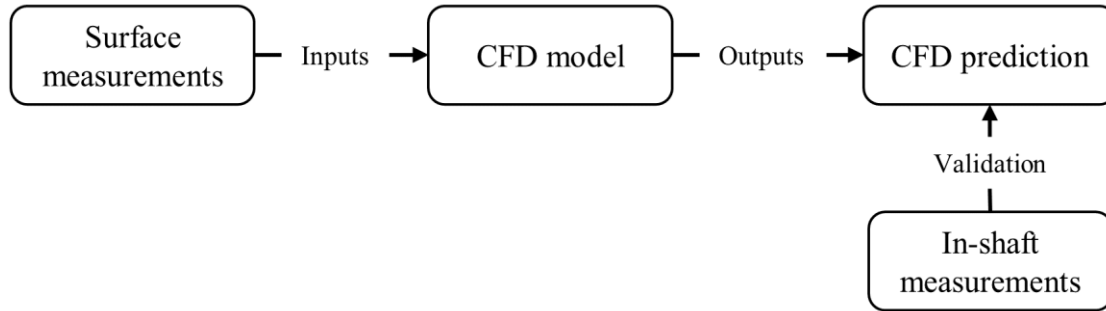


Figure 3.3. Relation between experimental measurements and CFD model.

### 3.3.1 Instrumentation Selection

The surface weather station was installed to measure the atmospheric microclimate conditions, and the in-shaft weather station to measure the internal tunnel's conditions. The surface weather station measured the following intensive properties for modeling configuration:

- The atmospheric pressure was measured to determine static pressure differences (Equation 2.5, p. 33) and calculate humid air properties.
- The atmospheric temperature was measured to calculate the thermal pressure difference (Equation 2.6, p. 33).
- The atmospheric humidity was measured to calculate the density changes that affect the thermal pressure difference (Equation 2.6, p. 33)
- The wind speed magnitude and direction were measured to calculate the wind pressure in the openings (Equation 2.7, p. 34).
- The precipitation rate was measured to identify the rain and no-rain conditions.

The in-shaft weather station measured the following intensive properties, in the shaft openings, for modeling validation:

- The vertical air velocity.
- The temperature.
- The humidity

The former in-shaft measurements were compared against the CFD model predictions.

#### 3.3.1.1 Surface Weather Station Instrumentation Selection

For the instrumentation required to measure atmospheric humidity, precipitation, atmospheric pressure, atmospheric temperature, and wind speed outside the tunnel, a commercial

weather station was considered suitable for the present work. The ATMOS 41 was selected because it contains all the instruments for the measurements required in the study in a single piece of equipment. The ATMOS 41 measures atmospheric humidity, precipitation, atmospheric pressure, atmospheric temperature, wind speed magnitude and direction, solar radiation, and lighting activity. The resolution and accuracy of the ATMOS 41's measurements used in the study are presented in Appendix A.

### **3.3.1.2 In-shaft Weather Station Instrumentation Selection**

Anemometers, flow visualization, and gas tracing measurements are different methods for measuring horizontal and vertical gas transport and ventilation inside sewer systems (Madsen et al., 2006; USEPA, 2004). The primary method found in the literature to measure airflow circulation in sewer systems was the gas tracing due to the practicality of the implementation (Madsen et al., 2006; Parker & Ryan, 2001; Pescod & Price, 1982; Ward et al., 2011). Parker and Ryan, Pescod and Price, and Ward et al. used carbon monoxide to measure the airflow circulation in the sewer system (2001; 1982; 2011). The carbon monoxide tracing consists of an injection of carbon monoxide in an upstream location, and the amount of carbon monoxide is measure in a second downstream location. Based on the convective diffusivity of the carbon monoxide in the air, the velocity is calculated (Parker & Ryan, 2001; Pescod & Price, 1982; Ward et al., 2011). Madsen et al. (2006) use molecular oxygen instead of carbon monoxide. They show that this method is also functional and requires that the molecular oxygen covers 10% of sewer headspace.

Despite the practicality of gas tracing, because of the large dimension of the DigIndy tunnel (5.5 m and 15 km for the initial alignment), the required amount of carbon monoxide and molecular oxygen would require a significant investment. Moreover, the gas tracing technic requires supervision during the measurement and is subjected to the gas supply, making it unsuitable for long periods and multiple parallel tracing locations. For the former reason, ultrasonic anemometers were considered more suitable for this study. The ultrasonic anemometer was located inside the vertical shafts to capture a representative bulk velocity of the shaft.

The ultrasonic anemometer, ATMOS 22, was selected to measure the velocity in the vertical shafts. The ATMOS 22 measures air velocity magnitude and direction, and air temperature. However, the temperature measures are used for internal corrections of the

instrument readings and shall be used cautiously for temperature reports. Consequently, the microclimate measuring station, ATMOS 14, was selected to measure the temperature and the humidity in the vertical shafts. The resolution and accuracy of the ATMOS 22 and ATMOS 14 are presented in Appendix A. More details of the installation are explained in the following sections.

### **3.3.2 Experimental Setup**

The experimental setup consists of two instrumentation pieces of equipment: a surface weather station and an in-shaft weather station. Figure 3.4.a shows a schematic of the proposed instrumentation deployment. The surface weather station consists of the ATMOS 41 weather station to measure the precipitation, atmospheric pressure, atmospheric temperature, atmospheric vapor pressure, and atmospheric wind speed in each location. The ATMOS 41 was installed on a pole at the height of 1.83 m from the surface, as shown in Figure 3.4.b.

The in-shaft weather station consists of the ATMOS 22 to measure the stream velocity in the vertical shaft and the ATMOS 14 to measure the vertical shafts' temperature and vapor pressure. Both sensors are attached to an 8020 aluminum frame located 6 m below the surface level. Figure 3.4.c shows the installation of the internal weather station in Eagle Creek's vent shaft. Technical drawings of the aluminum frame structure used to support the in-shaft sensors are presented in Appendix B for each location. Moreover, the bill of materials for each structure is presented in Appendix C.

To capture a representative bulk velocity in the vertical shafts, the velocity sensor must be located in a region where the fluid is fully developed (White, 2017). The in-shaft instrumentation preferably should be located aligned with the geometrical center of the inlet and a deepness of approximately 30 m (half of the height of the shaft). However, in the Eagle Creek drop shaft, a CSO discharge structure is located at 6.5 m from the surface. If the sensor is lower in that location, e.g., 30 m, the wastewater would hit the sensor and damage it during CSO events. For the former reason, the standard distance of 6 m from surface level was used in all the vertical shafts.

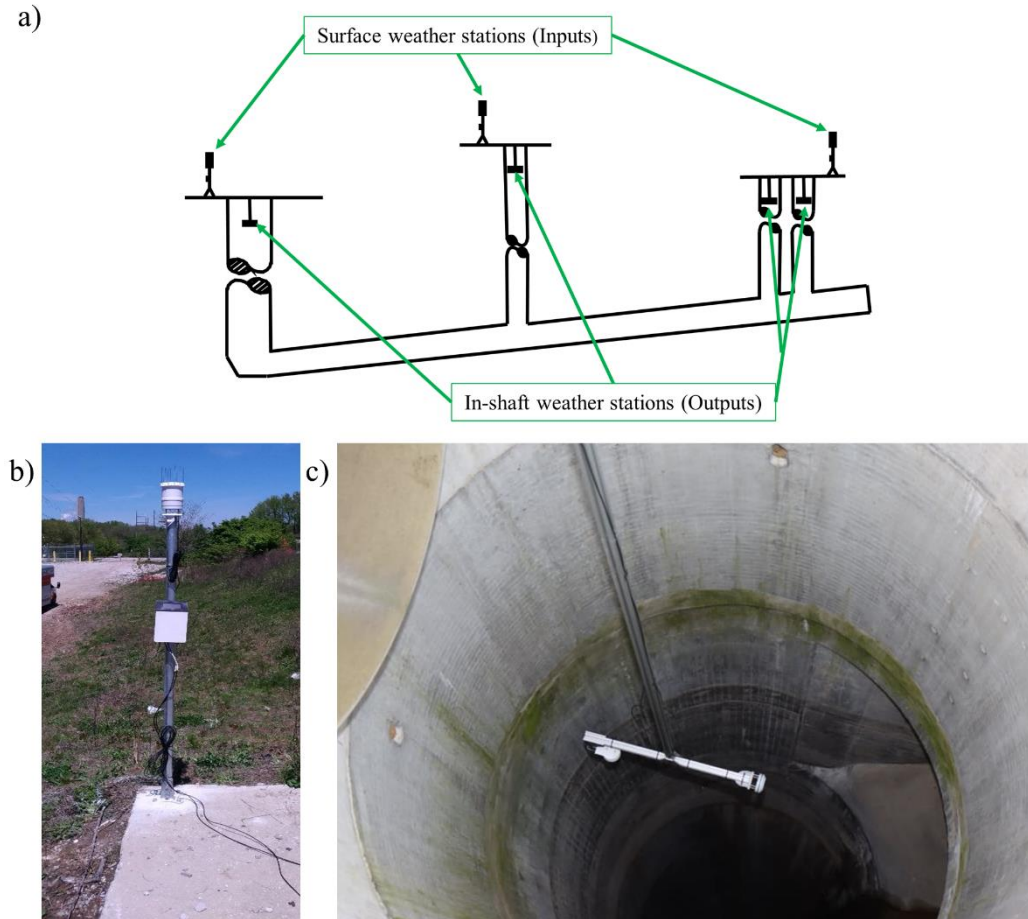


*Figure 3.4.* Instrumentation deployment for DRTC+ECT alignment: a) schematic of instrumentation location for the initial alignment, b) outside weather station installed in utility shaft No.3 location, and c) inside weather station installed in the Eagle Creek drop shaft. *Note.* Figure 3.4.c adapted from “Underground weather forecast: 0% chance of stink,” by John O’Malley, 2021, Purdue Polytechnic Newsroom. (<https://polytechnic.purdue.edu/newsroom/underground-weather-forecast-0-chance-of-stink>). In the public domain.

Due to the operation of a mechanical claw that takes out the garbage collected in the tunnel, the anemometer in the screen shaft location was not located aligned with the center of the opening. Contrarily, the anemometer was located decentered where the mechanical claw does not hit the sensors and debris does not reach the instrumentation. Figure 3.5 shows the final position for the screen shaft’s in-shaft weather station.

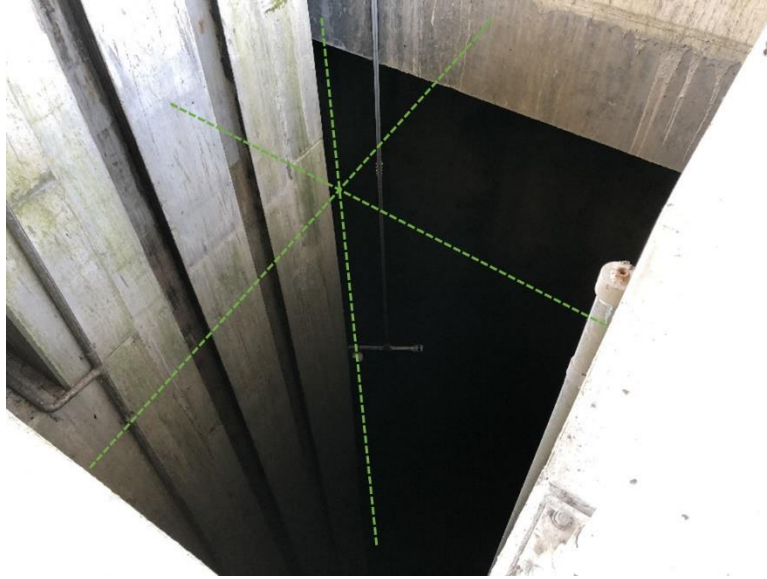


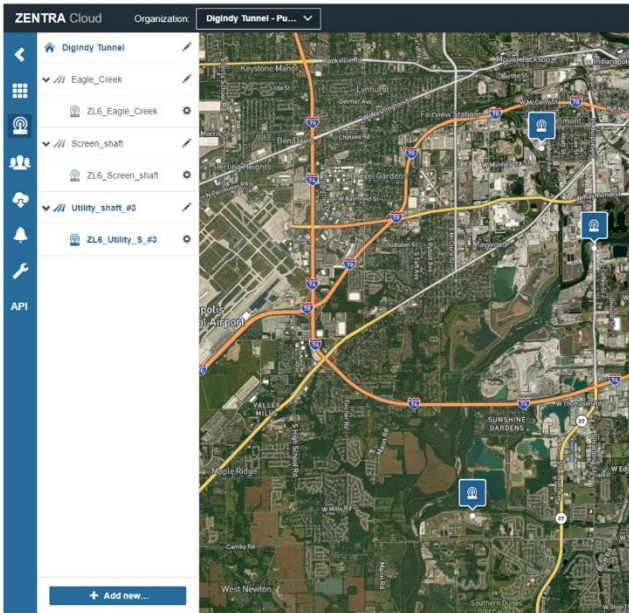
*Figure 3.5.* In-shaft weather final location in screen shaft. *Note.* Dotted lines represent the central geometrical axes of the opening.

Velocity measurements of the in-shaft weather station in the screen shaft location are unreliable since the measurements in that location do not represent the fully fluid-developed characteristics (White, 2017). Recirculation regions or eddies can affect anemometer measurements. However, measurements of temperature and humidity were valuable for the airflow analysis.

### **3.3.3 Data Collection**

The ATMOS 41, ATMOS 22, and ATMOS 14 in each location were connected to a ZL6 data logger. The data logger has a GPS that shows the instrumentation's location and a cellular communication protocol to transfer measured data to the cloud. Measurements were processed, sent, and saved in the cloud repository Zentra cloud each 5 min by the data logger. Measurements were recorded from May 2, 2020, to April 30, 2021. A total of 288 measurements for each intensive property is stored in one day. Figure 3.6 shows the Zentra cloud interface and an example of the temperature measurements for the utility shaft No.3 location. Figure 3.6.a shows the location of the instrumentation, which corresponds to the openings shown in Figure 3.2.a (p. 39).

a)



b)

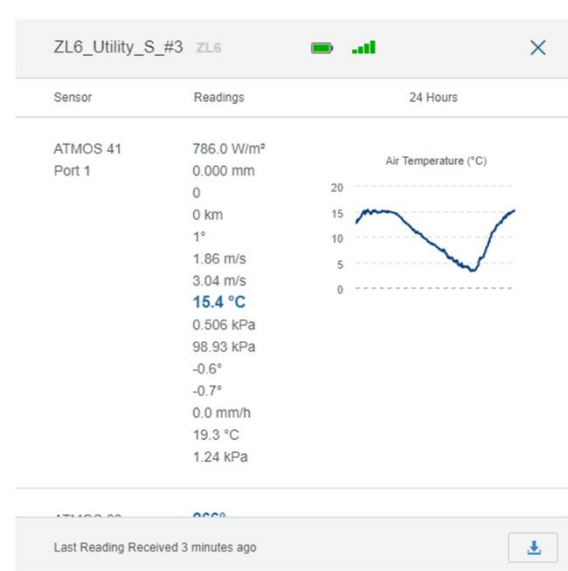


Figure 3.6. Zentra cloud interface: a) Zentra cloud webpage and b) utility shaft No.3 example measurement visualization.

### 3.3.4 Initial Testing of Instrumentation

Additionally to the ATMOS 41's calibration sheet given by the manufacturing company, the ATMOS 41s, ATMOS 22s, and ATMOS 14s were tested in the laboratory at Purdue University, West Lafayette, prior to the field installation. The atmospheric pressure, temperature, and atmospheric vapor pressure measurements were compared between the ATMOS 41s and ATMOS 14s, considering the ATMOS 41 measurements as the control. The ATMOS 41s and ATMOS 22s velocity measurements were tested by forcing air across the anemometer using a fan. The ATMOS 41s and ATMOS 14s temperature and relative humidity measurements were tested by monitoring the conditioned air temperature and humidity in the laboratory. All measurement comparisons between ATMOS 41s, ATMOS 22s, and ATMOS 14s agreed to within the rated accuracy of each instrument.

### 3.4 Numerical Modeling Procedure

A steady-state 3D CFD model of the DigIndy tunnel is developed in the commercial software ANSYS FLUENT (Ansys Inc, 2019). ANSYS FLUENT is a volume finite method

solver that calculates the fluid dynamics based on the continuity, momentum, and energy conservative equations (Ansys Inc, 2019). The CFD solver has been used for several studies to simulate multiphase flow in sewer systems (Cataño-Lopera et al., 2014; Chan et al., 2018) and natural air circulation in extra-long tunnels (Zhang et al., 2018).

Based on the finding from the literature review presented in Chapter 2 (p. 28), the following effects were modeled in this study:

- Pressure differences
- Wind suction
- Buoyancy forces
- Drag force from the clear water stream

Pressure differences, wind suction, and drag forces are modeled as boundary conditions in the numerical domain. Buoyancy forces are modeled by applying a body force throughout the volume of the numerical domain. The pressure-based solver was used in this study. The following section details the modeling implementation of these physical phenomena.

### **3.4.1 Modeled Physics**

#### **3.4.1.3 Buoyancy Forces**

The buoyancy forces were modeled by setting the operating density equal to zero in the CFD solver. When the operating density is equal to zero, the body force term in the continuity equation is accounted for (Ansys Inc, 2021). In order to capture the change of density by changes in temperature and humidity, the ideal gas law was used to compute the density across the center of the volume cells (Ansys Inc, 2021).

##### **3.4.1.3.1 Humid Air Modeling**

The fluid in the tunnel was modeled as humid air. The humid air was modeled as a single-phase fluid mixture where the species transportation model calculates the water vapor mass fraction of dry air and water vapor in the single phase (Ansys Inc, 2021). Table 3.2 shows the configuration that is used to set up the mixture.



Table 3.2. Species transportation model configuration.

Properties	Model
Density	Ideal gas law
Specific heat	Mixing-law
Thermal conductivity	Mass-weighted-mixing-law
Dynamic viscosity	Mass-weighted-mixing-law

In addition to the configuration shown in Table 3.2, the inlet diffusion and diffusion energy source options were activated. Furthermore, the properties of dry air and water vapor used to calculate the properties of the mixture are presented in Table 3.3.

Table 3.3. Air and water vapor properties.

Dry air properties				
Properties	Fitted polynomial/Constant value	Units	Range	R <sup>2</sup>
$C_p(T)$	$1.122x10^3 - 8.817x10^{-1} \cdot T + 2.174x10^{-3} \cdot T^2 - 1.924x10^{-6} \cdot T^3 + 7.658x10^{-10} \cdot T^4 - 1.142x10^{-13} \cdot T^5$	$J/kg \cdot K$	$223.15 \leq T \leq 2273.15 (K)$	0.99
$k(T)$	$9.920x10^{-4} + 9.050x10^{-5} \cdot T - 2.915x10^{-8} \cdot T^2 + 4.761x10^{-12} \cdot T^3 - 4.922x10^{-17} \cdot T^4 + 7.431x10^{-21} \cdot T^5$	$W/m \cdot K$	$223.15 \leq T \leq 2273.15 (K)$	0.99
$\mu(T)$	$5.240x10^{-7} + 7.559x10^{-8} \cdot T - 6.354x10^{-11} \cdot T^2 + 4.221x10^{-14} \cdot T^3 - 1.520x10^{-17} \cdot T^4 + 2.174x10^{-21} \cdot T^5$	$kg/m \cdot s$	$223.15 \leq T \leq 2273.15 (K)$	0.99
$M_{air}$	29.966	$kg/K \cdot mol$		
Water vapor properties				
Properties	Fitted polynomial/Constant value	Units	Range	R <sup>2</sup>
$C_p(T)$	$1563.077 + 1.604 \cdot T - 2.933x10^{-3} \cdot T^2 + 3.216x10^{-6} \cdot T^3 - 1.157x10^{-9} \cdot T^4$	$J/kg \cdot K$	$300 \leq T \leq 1000 (K)$	
$k$	$k = 1.34x10^{-5}$	$W/m \cdot K$		
$\mu$	$\mu = 1.34x10^{-5}$	$kg/m \cdot s$		
$M_v$	18.015	$kg/K \cdot mol$		
$D(T)$	$2.26x10^{-5} \left( \frac{T}{273.15} \right)^{1.81} \left( \frac{100x10^5}{P_{abs}} \right); \{P \text{ in } Pa\}$	$m^2/s$	$253.15 \leq T \leq 313.15 (K)$	

Note. Fitted polynomials for dry air properties were calculated based on the data tabulated by Çengel and Ghajar (2015, p. 926). The mass diffusivity of water vapor in dry air was based on Montgomery's work (1947). The remaining properties were taken from ANSYS FLUENT default library.

### 3.4.1.3.2 Condensation

Humid air can store a maximum amount the water vapor depending on its temperature. When the humid air has the maximum amount of water is considered saturated (Çengel et al., 2019). Vapor pressure is an absolute scale that measures the amount of water vapor in terms of pressure (Buck, 1981). The saturation vapor pressure for a given temperature can be calculated as is shown in Equation 3.1 (Buck, 1981).

$$P_{sat}(T) = a \cdot e^{\left(\frac{bT}{c+T}\right)} (Pa); \{T \text{ in } ^\circ C \text{ and } P \text{ in } Pa\}$$

$$a = 611 \text{ Pa}, b = 17.502, \text{ and } c = 240.97 ^\circ C \text{ when } T > 0 ^\circ C \quad (3.1)$$

$$a = 611 \text{ Pa}, b = 21.87, \text{ and } c = 265.5 ^\circ C \text{ when } T \leq 0 ^\circ C$$

Equation 3.1 can be rewritten in terms of the temperature to calculate the saturation temperature for a given vapor pressure. Equation 3.2 shows the calculation of the saturation temperature as a function of vapor pressure.

$$T_{sat}(P_v) = \frac{c \cdot \ln\left(\frac{P_v}{a}\right)}{b - \ln\left(\frac{P_v}{a}\right)} ; \{T \text{ in } ^\circ C \text{ and } P \text{ in } Pa\}$$

$$a = 611 \text{ Pa}, b = 17.502, \text{ and } c = 240.97 ^\circ C \text{ when } T > 0 ^\circ C \quad (3.2)$$

$$a = 611 \text{ Pa}, b = 21.87, \text{ and } c = 265.5 ^\circ C \text{ when } T \leq 0 ^\circ C$$

When the amount of water vapor in the air exceeds the maximum capacity of air retention, the water vapor starts to condense, the condensation can occur in the bulk of the fluid or walls (Vyskocil et al., 2014). For this study, the wall condensation is not modeled, and only bulk condensation is considered. It should be noted that wall condensation was implemented during model development and was found to have minimal effect on the flow field while negatively affecting the numerical stability of the model. Moreover, to achieve accurate results of condensed water in the wall, a high resolution, i.e.,  $y^+ = 1$ , is required in the first cells of the domain adjacent to the walls, which is forbidden for the model's applicability (Vyskocil et al., 2014). The bulk condensation is modeled according to the model presented by Vyskocil et al. (2014). The condensation process adds heat to the domain according to Equation 3.3.

$$Q_{v1} = C_{p,m} \rho_m \frac{T_{sat}(P_v) - T_m}{\tau} (W/m^3)$$

$$Q_{v2} = \rho_m Y_v \frac{h_{lat}}{\tau} (W/m^3) \quad (3.3)$$

$$Q_v = \min(Q_{v1}, Q_{v2})$$

The term  $\tau$  in Equation 3.3 represents a time scale of droplets' condensation. The value of  $\tau$  was selected as 10 s according to the study of the aerosol particle presented by Rothfuss et al. (2018). The term  $h_{lat}$  represents the latent heat of evaporation if  $T > 273.15$  K or latent heat of sublimation if  $T \leq 273.15$  K. Table 3.4 shows the latent heat of evaporation and sublimation as a function of the temperature.

Table 3.4. Water's latent heat of evaporation, latent heat of sublimation, and enthalpy of saturated liquid water.

Latent heat of evaporation				
Properties	Fitted polynomial/Constant value	Units	Range	R <sup>2</sup>
$h_{lat}(T)$	$3147.100 - 2.364 \cdot T$	$kJ/kg$	$273.15 < T \leq 323.15 (K)$	0.99
Latent heat of sublimation				
Properties	Fitted polynomial/Constant value	Units	Range	R <sup>2</sup>
$h_{lat}(T)$	$2687.100 + 9.992 \times 10^{-1} \cdot T - 4.121 \times 10^{-4} \cdot T^2 - 4.655 \times 10^{-6} \cdot T^3$	$kJ/kg$	$220 \leq T \leq 273.15 (K)$	0.99
Enthalpy of saturated liquid water				
Properties	Fitted polynomial/Constant value	Units	Range	R <sup>2</sup>
$h_l(T)$	$-1143.3 + 4.186 \cdot T$	$kJ/kg$	$273.15 < T \leq 323.15 (K)$	1

*Note.* Fitted polynomial for water's latent heat of evaporation was calculated based on the data tabulated by Çengel and Ghajar (2015, p. 920). Fitted polynomial for water's latent heat of sublimation was calculated based on the data tabulated by Feistel and Wagner (2007, p. 41). Fitted polynomial for the enthalpy of saturated liquid water was calculated based on the data tabulated by Çengel et al. (2019, p. 888).

As described in the modeling assumptions in Chapter 1 (p. 23), the two-phase flow effects of water droplets condensing were not considered. However, the effects of condensation were modeled. For instance, condensation reduces the water vapor mass fraction in the species transportation equation and the total mass in the continuity equation. In order to account for the changing water vapor mass fraction, a source term was applied to the species and continuity

equation in the CFD solver. Equation 3.4 shows the calculation for the species and continuity source term.

$$S_v = S_m = -\frac{Q_v}{h_{lat}} \leq 0 \text{ (kg/m}^3\text{)} \quad (3.4)$$

The effects of condensation were also manifest in the momentum and energy equations and source terms for the respective equations were required. Equation 3.5 shows the calculation for the momentum equation and Equation 3.6 for the energy equation.

$$\vec{S}_{\rho v} = S_v \vec{V} \text{ (N/m}^3\text{)} \quad (3.5)$$

$$S_e = Q_v + S_v h_l \text{ (W/m}^3\text{)} \quad (3.6)$$

The term  $h_l$  in Equation 3.6 is the enthalpy of saturated liquid water, and its value is tabulated in Table 3.4. The source terms presented in Equation 3.4 to Equation 3.6 were implemented via a user defined function (UDF) in the CFD solver. If required, analogous source terms to Equation 3.5 are used for source terms for turbulence models equations or other diffusion-convection equations. For this study, two additional source terms were required for the turbulent kinetic energy ( $k$ ) and turbulent dissipation rate ( $\epsilon$ ) from the RANS  $k$ - $\epsilon$  turbulence model.

#### **3.4.1.1 Pressure Differences**

For the study, outlet and inlet pressures were used to set up the model boundary conditions. The pressure difference between the openings is calculated, as is shown in Equation 3.7.

$$\Delta P_i = \Delta P_{s_i} + \Delta P_{w_i} + \Delta P_{t_i} \quad (3.7)$$

The subscript “i” represents an arbitrary opening in the system, and the differences are calculated against a reference location. For the study, the reference location is the screen shaft tunnel opening shown in Figure 3.2.a (p. 39). The screen shaft opening is the lowest of all the

DigIndy tunnel openings for all alignments considered. The pressure calculated from Equation 3.7 in each location is used to set up inlet-vent and outlet-vent boundary conditions in the model. The three terms in Equation 3.7 correspond to the forces presented in Chapter 2 (p. 32), with minor differences due to how the forces are treated in the CFD solver, are explained in the following subsections.

#### 3.4.1.1.1 Static Pressure Difference

The first term in Equation 3.7 describes the static pressure difference between the tunnel openings. Differences in static pressure come from differences in the local atmospheric pressure and external devices at the openings (i.e., fans, blowers, and extractors in the openings). The static pressure difference is calculated as is shown in Equation 3.8. For the present work, the static pressure difference was assumed to be zero since no external devices modify the static pressure at the openings. Moreover, during the project development, the static pressure differences calculated using the measured atmospheric pressures were found to be smaller than the experimental uncertainty of the measurements, making their use unreliable. The justification of this assumption is discussed further in Section 4.1.1 (p. 69).

$$\Delta P_{s_i} = P_i - P_{ref} \quad (3.8)$$

Equation 3.8 differs from Equation 2.5 (p. 33) because the gravity term is already included in the buoyancy model of the CFD solver.

#### 3.4.1.1.2 Thermal Potential Pressure Difference

The second term in Equation 3.7 describes the effect of height and temperature difference between the opening's entrances. The thermal potential pressure difference is calculated as is shown in Equation 3.9. The term  $H_{i-ref}$  in Equation 3.9 represents the difference in the height of each opening with respect to the reference point.

$$\Delta P_{ti} = -\rho_{avg} g H_{i-ref} \text{ where } \rho_{avg} = \frac{\rho_{ref} + \rho_i}{2} \text{ and } H_{i-ref} = H_i - H_{ref} \quad (3.9)$$

Equation 3.9 differs from Equation 2.6 (p. 33) because the gravity term is already included in the buoyancy model of the CFD solver. Table 3.5 shows the height difference for each opening presented in Figure 3.2 (p. 39).

*Table 3.5. Height difference with respect to screen shaft opening for each opening.*

Opening	$H_{i-ref}(m)$
Screen shaft	0
Utility shaft No.3	6.503
Eagle Creek vent shaft	5.374
Eagle Creek drop shaft	5.374
LP vent shaft	14.532
WR vent shaft	11.933
FC working shaft	11.887
FC retrieval shaft	19.964
PR working shaft	4.998
PR intermediate shaft	24.140
PR retrieval shaft	36.725

#### **3.4.1.1.3 Wind Suction Pressure Difference**

The last term in Equation 3.7 describes the effect of wind suction in each tunnel opening. The wind suction pressure difference is calculated as is shown in Equation 3.10 (Olson et al., 1997).

$$\Delta P_{wi} = \frac{\rho_{ref}}{2} V_{w,ref}^2 - \frac{\rho_i}{2} V_{wi}^2 \quad (3.10)$$

Equation 3.10 differs from Equation 2.7 (p. 34) because, for this study, the wind was perpendicular to the vertical shaft opening. Instead of creating a dynamic pressure in the entrance, the perpendicular wind creates a suction (Olson et al., 1997; Pescod & Price, 1982).

### 3.4.1.4 Clear Water Stream

A clear water stream at the bottom of the tunnel was modeled as a smooth-moving wall (Ward et al., 2011). The clear water stream height was calculated assuming a uniform channel flow with a constant volumetric flow. Figure 3.7 shows a schematic of a uniform channel flow inside a circular pipe.

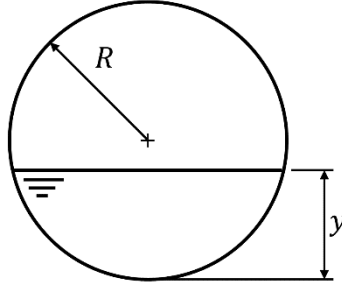


Figure 3.7. Schematic of water height in the tunnel's bottom.

Based on Figure 3.7, the wetted area and wetted perimeter were calculated as described in Equation 3.11 and Equation 3.12, respectively.

$$A = R^2 \cos^{-1} \left( \frac{R-y}{R} \right) - (R-y) \sqrt{2Ry - y^2} \quad (3.11)$$

$$P = 2 \cos^{-1} \left( \frac{R-y}{R} \right) R \quad (3.12)$$

The hydraulic radius of the clear water stream was calculated using the wetted area and wetted perimeter as  $R_h = A / P$ . Knowing the hydraulic radius of the clear water stream and the slope of the channel ( $S_0 = 0.001$ ), the flow velocity of a uniform channel flow was calculated using Equation 3.13.

$$V_0 = V_{ws} = \left( \frac{8g}{f} \right)^{\frac{1}{2}} R_h^{1/2} S_0^{1/2} \quad (3.13)$$

The friction factor was calculated assuming a fully rough turbulent flow, as depicted in Equation 3.14 (White, 2017).

$$f \approx \left( 2.0 \log \frac{14.8 R_h}{\varepsilon} \right)^{-2} \quad (3.14)$$

The roughness height for concrete was assumed to equal 1 mm (White, 2017). Finally, the volumetric flow was calculated as  $Q = A \cdot V_0$ . Because the height of the clear water stream appears in both the wetted area and the velocity of the volumetric flow calculation, an iterative process was carried out to find the velocity and area that results in the required volumetric flow. After the iterative process, the resulted height was subtracted from the computational model, and the resulting flat face has the velocity vector. Table 3.6 shows clear water stream volumetric flow assumed and the respective flow velocity and water height calculated for each of the alignments analyzed in this study.

Table 3.6. Clear water stream volumetric flow, velocity flow, and water height for each alignment.

Alignment	Volumetric flow ( $m^3/s$ )	Flow velocity ( $m/s$ )	Stream height (m)
DRTC+ECT	$4.732 \times 10^{-2}$	0.446	0.105
DRTC+ECT+WRT+LPgRT	$8.202 \times 10^{-2}$	0.525	0.137
DRTC+ECT+WRT+LPgRT+FCT	$1.009 \times 10^{-1}$	0.558	0.150
DRTC+ECT+WRT+LPgRT+FCT+PRDT	$1.356 \times 10^{-1}$	0.609	0.173

Note. The volumetric flows from the second to the fourth alignment were linearly estimated based on the volumetric flow in the initial alignment and the length of the tunnel.

The clear water stream velocity was implemented via user defined function (UDF). The velocity direction was calculated based on the perpendicular vector to the normal face vector of the boundary faces, which is parallel to the clear water stream direction. Figure 3.8 shows a schematic of an arbitrary wall face with the normal face vector ( $\vec{A}$ ) and the clear water stream direction ( $\vec{V}_{ws}$ ).

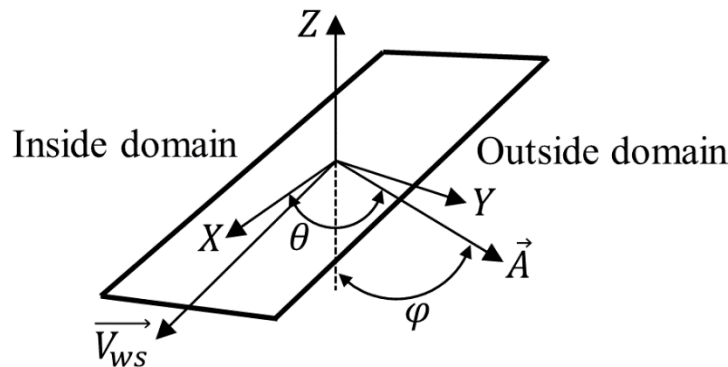


Figure 3.8. Schematic of the velocity vector direction of the clear water stream.



ANSYS FLUENT considers the normal face vector for each boundary face, always pointing out the domain as shown in Figure 3.8 (Ansys Inc, 2021). Since the direction of the normal face vector is known, and the tunnel has a constant slope (0.1%) that points towards the screen shaft location, a coordinate system change can be used to determine the direction of the clear water stream. First, from the cartesian coordinates of the normal face vector, spherical coordinates azimuthal angle ( $\theta$ ) and polar angle ( $\varphi$ ) were calculated as is shown in Equation 3.14 and Equation 3.15, respectively.

$$\theta = \tan^{-1} \left( (A_y/|\vec{A}|) / (A_x/|\vec{A}|) \right) \quad (3.14)$$

$$\varphi = \cos^{-1}(A_z/|\vec{A}|) \quad (3.15)$$

Then, because the slope was known to point towards the screen shaft location and the clear water stream is perpendicular to the normal face vector, the vector director vector can be known by rotating the polar angle  $+\pi/2$  rad. With the azimuthal and polar angle calculated with Equation 3.14 and Equation 3.15, respectively, the velocity component of each boundary face was calculated as is shown in Equation 3.16 to 3.18.

$$U = V_{ws} \sin(\varphi + \pi/2) \cos(\theta) \quad (3.16)$$

$$V = V_{ws} \sin(\varphi + \pi/2) \sin(\theta) \quad (3.17)$$

$$W = V_{ws} \cos(\varphi + \pi/2) \quad (3.18)$$

### 3.4.2 Computational Model Setup

#### 3.4.2.1 Computational Mesh

Because of the geometric complexity and flow physics considered, i.e., buoyancy force, generating the computational mesh required careful consideration. The following sections

explain the meshing strategy in more detail, as well as a mesh independence analysis for the initial alignment.

#### **3.4.2.1.1 Tunnel Geometry Simplification**

To reduce the number of elements required for the model, simplifications of the segments that do not have direct atmosphere openings were performed, as described in the assumptions in Chapter 1 (p. 23). Figure 3.9 shows the schematics of the simplified models that were used in the study.

The dashed lines in Figure 3.9 represent the tunnel segments that were removed from the actual configuration shown in Figure 3.1 (p. 38). The dashed sections in Figure 3.9 are removed because they do not have any openings along the segment, which could contribute to air circulation in the tunnel.

#### **3.4.2.1.2 Meshing Strategy**

The fully-developed velocity profile in the circular pipe was affected by the buoyancy forces (Abdelmeguid & Spalding, 1979; Tian et al., 2019). Additionally to the axial velocity profile present in fully-developed pipe flow, the buoyancy forces create additional secondary flows in the radial and circumferential directions. In order to capture the complex flowfield, the mesh was refined in all three directions: radial, circumferential, and axial (Tian et al., 2019). Also, adjacent to the wall, an inflation layer was used to capture the boundary layer (Ansys Inc, 2021).

The computational domain mesh was assembled using hexahedron, prism, and tetrahedral element types. Figure 3.10 shows an example of the meshing strategy used at the utility shaft No.3 T-junction. The hexahedron elements discretize the outer cylindrical segments of the tunnel, and the tetrahedral elements discretize the T-junction, bifurcation, and vertical shafts. The inflation layer consists of prism elements (not shown in Figure 3.10, which grow radially inward from the tunnel wall toward the tunnel centerline). The hexahedron and prism elements are preferred over the tetrahedral elements because they provide more stability with fewer elements (Ferziger et al., 2020). Again, tetrahedrons were only used in regions with highly complex geometry that prohibited the use of hexahedrons.

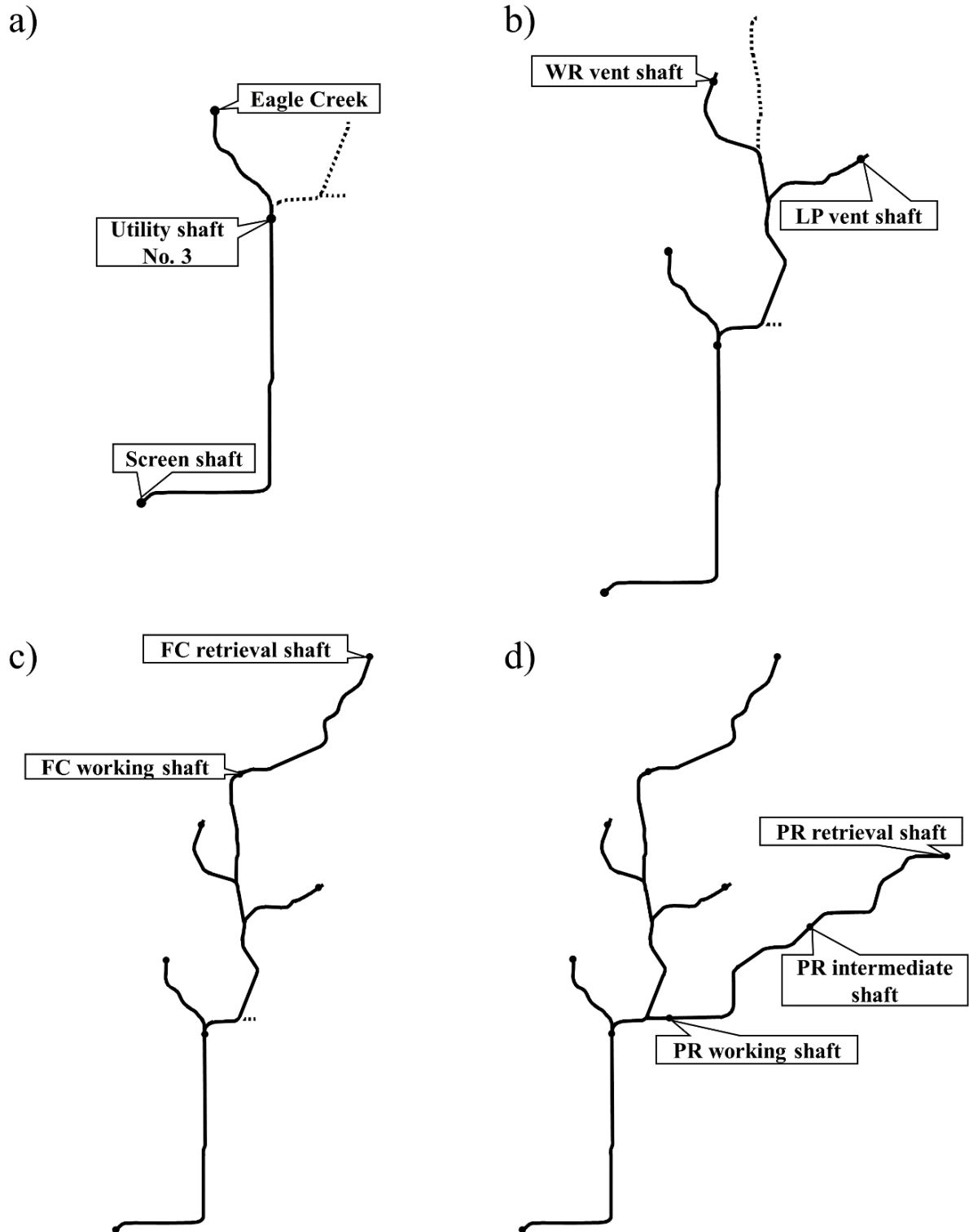
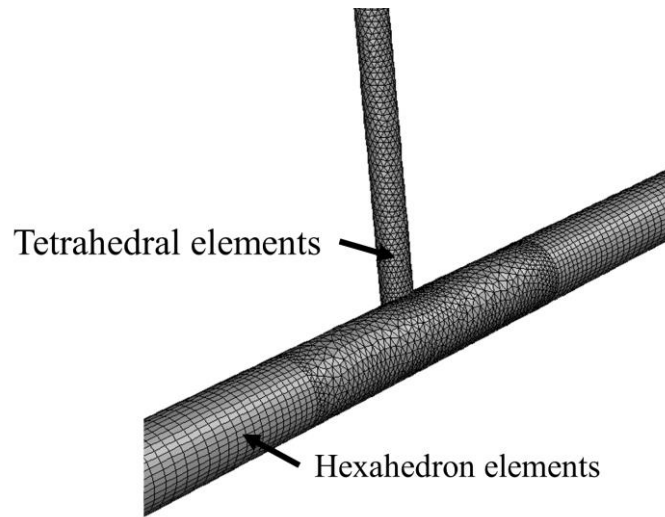


Figure 3.9. Schematics of tunnel alignment mesh simplifications: a) computational mesh for DRTC+ECT alignment, b) computational mesh for DRTC+ECT+WRT+LPgRT, c) computational mesh for DRTC+ECT+WRT+LPgRT+WRT, and d) computation mesh for DRTC+ECT+WRT+LPgRT+WRT+PRT alignment. *Note.* Dashed lines represent sections of the tunnel removed.

Tetrahedrons elements with a characteristic length of 2 m were used in the unstructured section of the meshes. The first cells adjacent to the different walls in the model were set so that the  $y^+$  were between 30 and 300 (Ansys Inc, 2021). For example, the first cells adjacent to the wall in the main section of the tunnel had a thickness of  $3.2 \times 10^{-2}$  m. The  $y^+$  range secures the correct use of the turbulence RANS model and the scalable wall function mentioned in Section 3.4.2.2 (p. 61). The inflation layers consisted of 10 layers with a growth rate of 1.1.



*Figure 3.10. Types of meshes over T-junction.*

The straight sections of the tunnel were discretized with longitudinal elements having a length of 1 m along the tunnel's axis. The circumference of the tunnel was discretized using 40 divisions of equal angular spacing. The perimeter of the utility shaft No.3 opening was discretized with elements of length  $7.5 \times 10^{-2}$  m. The perimeters of the Eagle Creek vent shaft, Eagle Creek drop shaft, LP vent shaft, and WR vent shaft opening were discretized with elements of length  $3 \times 10^{-2}$  m. Finally, the perimeter of the screen shaft, working shafts, retrieval shafts, and intermediate shaft were discretized with elements of length  $1 \times 10^{-1}$  m. Additionally to the careful selection of global element sizing, local refinements were required in complex geometrical sections of the tunnel, e.g., bulkheads and non-cylindrical tunnel sections, to keep the maximum skewness of the meshes below 0.85 and the orthogonal quality above 0.15. Table 3.7 shows the total number of cells used for each of the alignments and the control quality criteria achieved for each mesh.

Table 3.7. Information of the number of cells and control quality values for the different alignment meshes.

Alignment	Number of cells	Maximum Skewness	Minimum Orthogonal Quality
DRTC+ECT	11,161,184	0.85	0.15
DRTC+ECT+WRT+LPgRT	19,911,777	0.85	0.15
DRTC+ECT+WRT+LPgRT+FCT	26,731,416	0.84	0.15
DRTC+ECT+WRT+LPgRT+FCT+PRDT	36,606,913	0.85	0.15

### 3.4.2.1.3 Mesh Independence Analysis

A mesh independence study was carried out for the initial tunnel alignment. Three meshes were used for the independence analysis: a coarse mesh with 6,089,767 elements, a fine mesh with 11,161,184 elements, and an extra-fine mesh with 26,431,747 elements. The mesh density relation between each mesh was approximately 1.5 times. For example, the main tunnel circular edge in the coarse mesh was discretized with 27 divisions, whereas the fine mesh with 40 and the extra-fine with 60 divisions. The boundary conditions used for the mesh independence are the boundary conditions for May 2020, presented in Section 4.1.1 (p. 69).

Figure 3.11 shows the results of the mesh independence analysis. Figure 3.11.a shows vertical velocity, Figure 3.11.b shows temperature, and Figure 3.11.c shows the water vapor mass fraction in each of the openings of the initial alignment. The data presented in Figure 3.11 are local flowfield values collected at the exact physical locations in each vertical shaft as their respective in-shaft measurement stations. These local flowfield values were selected because validation presented in Section 4.1.2 (p. 73) was performed comparing these local flowfield values between the experimental measurements and the CFD predictions.

Relative errors below 1.45% in local flowfield values were observed in Figure 3.11 for the three meshes considered, except for the vertical velocity in utility shaft No.3 that had a relative error of 15% between the fine and the extra-fine mesh. However, the absolute error was  $5.45 \times 10^{-2}$  m/s, and the solution was considered mesh independent. The fine mesh was selected as the final mesh for its balance of improved resolution relative to the coarse mesh and reduced computational expense relative to the extra-fine mesh. All remaining simulations used the same meshing strategy, i.e., global sizing, inflation layers, and local refinements, as the fine mesh considered here and explained in detail in Section 3.4.2.1.2 (p. 58).

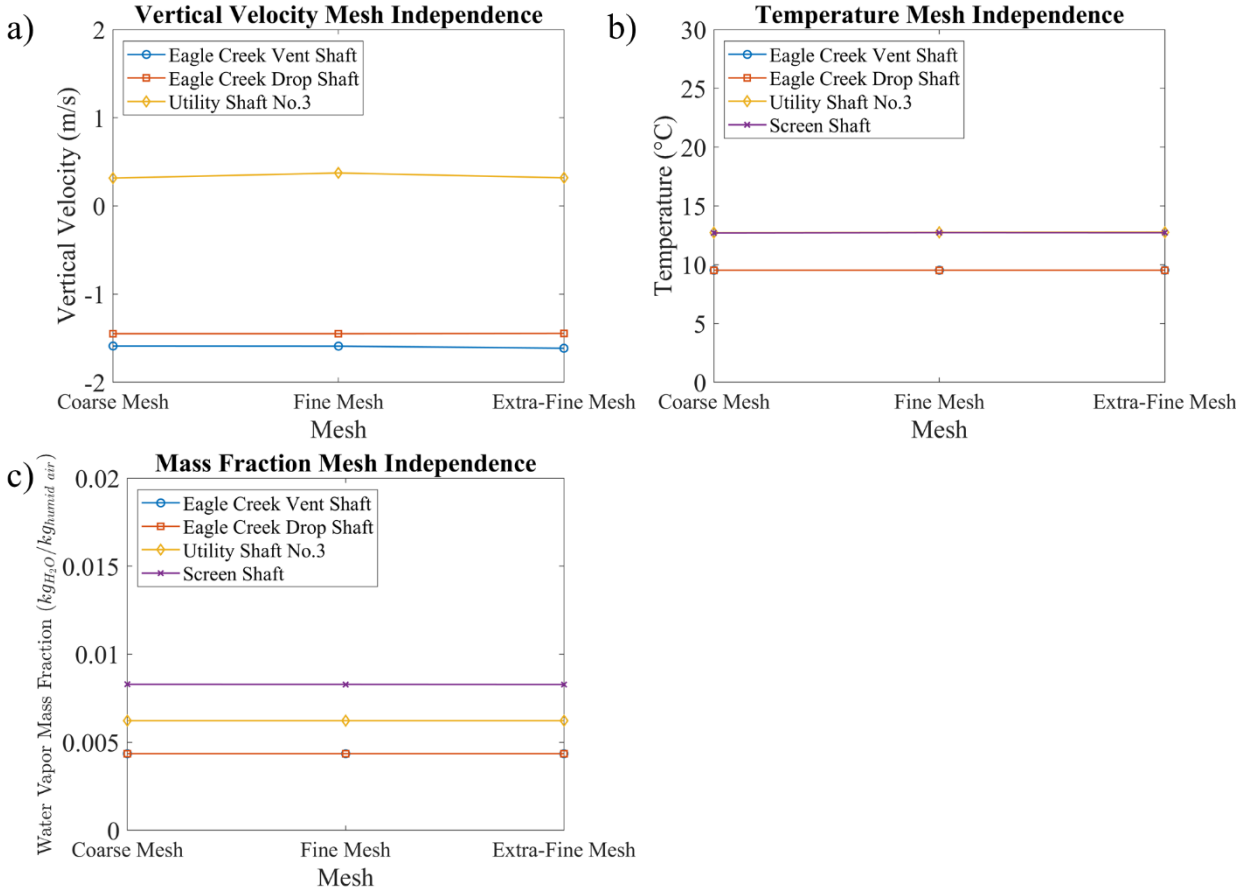


Figure 3.11. Results of mesh independence analysis: a) vertical velocity in-shaft openings mesh independence, b) temperature in-shaft openings mesh independence, and c) mass fraction in-shaft openings mesh independence.

### 3.4.2.2 Computational Model Configuration

The following list provides a summary of all solver settings and discretization schemes:

- The flow was in a steady state.
- The ideal gas equation of state was used.
- The turbulence model RANS k- $\epsilon$  realizable with full buoyancy effects active was used.
- The scalable wall function was used for near-wall treatment.
- The coupled solver scheme was used for pressure-velocity coupling. A flow Courant number of 200 was used.
- The least-square cell-based method was used for the discretization of the gradient terms.

- The PRESTO interpolation method for pressure interpolation was used. The PRESTO scheme is recommended when buoyancy forces are modeled (Ansys Inc, 2021).
- The second-order upwind discretization scheme was used for advection terms.
- The second-order central discretization scheme was used for diffusive terms.
- The under relaxation factors for momentum, pressure, density, body forces, turbulent kinetic energy, turbulent dissipation rate, turbulent viscosity, water vapor species, and energy were 0.8, 0.2, 1, 1, 0.4, 0.4, 1, 0.99, and 0.99, respectively.
- The tunnel walls were considered smooth finished concrete with a roughness  $\varepsilon = 1 \text{ mm} \approx K_s$  (White, 2017).
- The screen shaft's atmospheric pressure was used as the operating pressure in ANSYS FLUENT. The operating pressure is used to calculate fluid properties, e.g., humid air density and mass diffusivity (Ansys Inc, 2021).
- The screen shaft location was used as the reference location for the calculation of pressure differences.

### **3.4.2.3 Momentum Boundary Conditions**

The momentum boundary conditions were considered as outlet-vent and inlet-vent. The boundary conditions inlet-vent and outlet-vent differs from the pressure-inlet and pressure-outlet in that the formers included a minor loss coefficient in the boundary (Ansys Inc, 2021). The pressure magnitudes apply to each opening were calculated according to the procedure explained in Section 3.4.1.1 (p. 52).

#### **3.4.2.3.1 Entries and Exits Minor Loss Coefficients**

When the flow reenters a pipe from a reservoir or is exhaust to a reservoir, a drop of pressure occurs (Çengel & Cimbala, 2018). Furthermore, when the flow passes across a surface with holes, e.g., steel grating, a drop of pressure also occurs (Holt et al., 2012; Malavasi et al., 2012). The drop of pressure can be calculated as is shown in Equation 3.19.

$$\Delta P_{drop} = K_{Li} \frac{\rho_i}{2} V_i^2 \quad (3.19)$$

The term  $K_{Li}$  is known as the minor loss coefficient and depends on the entry or exit condition. For this study, all exits were considered with a minor loss coefficient of 0.8, and all entries were considered with a minor loss coefficient of 1.05 (Çengel & Cimbala, 2018). Besides the entry or exit loss coefficient, if the vertical shafts have a grating, an additional loss coefficient must be calculated. Hotl et al. (2012) describe a method to calculate the minor loss coefficient of a perforated plate base on the equivalent diameter ratio “ $\beta$ ” and the characteristics of the plate. The equivalent diameter ratio relates the effective area opened of the plate with the total area of the pipe, as is shown in Equation 3.20.

$$\beta = \sqrt{\frac{A_{open}}{A_{total}}} \quad (3.20)$$

Based on the equivalent diameter ratio, the minor loss coefficient of the plate was calculated using Equation 3.21.

$$K_L = \begin{cases} \left[ 2.9 - 3.79 \frac{t}{d_h} \beta^{0.4} + 1.79 \left( \frac{t}{d_h} \right)^2 \beta^{0.8} \right] K_{LS} & \frac{t}{d_h} \beta^{0.4} \leq 0.9 \\ \left( 0.876 + 0.069 \frac{t}{d_h} \beta^{0.4} \right) K_{LS} & \frac{t}{d_h} \beta^{0.4} > 0.9 \end{cases} \quad (3.21)$$

$$K_{LS} = 1 - \frac{2}{\beta^2} + \frac{2}{\beta^4} \left( 1 - \frac{1}{C_c} + \frac{1}{2C_c^2} \right) \quad (3.22)$$

The term  $K_{LS}$  represents the minor loss coefficient for a single hole (Equation 3.22). The contraction coefficient,  $C_c$ , is recommended to be set as 0.72 (Holt et al., 2012; Malavasi et al., 2012). The effect of the entry or exit drop pressure is additive. Therefore, the minor loss coefficient for entry or exit and the minor loss coefficient for the gratings are added if both cases are presented. Table 3.8 presents the minor loss coefficients calculated for DigIndy tunnel openings based on the structural characteristics.



Table 3.8. Minor loss coefficients for openings in the DigIndy tunnel.

Opening	Type	$K_{L_{type}}$	$K_{L_{grating}}$	$K_L$
Screen shaft	Exit	1.05		1.05
Utility shaft No.3	Entry	0.8	13.143	14.193
Eagle Creek vent shaft	Entry	0.8	0.818	1.618
Eagle Creek drop shaft	Entry	0.8	0.818	1.618
LP vent shaft	Entry	0.8	0.714	1.514
WR vent shaft	Entry	0.8	0.714	1.514
FC working shaft	Entry	0.8	0.620	1.420
FC retrieval shaft	Entry	0.8	0.620	1.420
PR working shaft	Entry	0.8	0.696	1.496
PR intermediate shaft	Entry	0.8	0.620	1.420
PR retrieval shaft	Entry	0.8	0.620	1.420

#### **3.4.2.4 Thermal Boundary Conditions**

After 15 m below ground, the soil temperature is constant and is not affected by diurnal changes in temperature (Busby et al., 2009; Hanova & Dowlatabadi, 2007). The DigIndy's tunnel is located between 60 – 70 m below ground; therefore, the temperature was considered constant with a value of 12.78 °C (Kusuda & Achenbach, 1965).

For the vertical shafts, diurnal temperature changes change the soil temperature up to a deepness of 15 m (Busby et al., 2009; Hanova & Dowlatabadi, 2007). A decreasing exponential function is used to model the soil's temperature profile (Holmes et al., 2008; Van Wijk & Derksen, 1966). Equation 3.23 shows the piecewise function used to set up the boundary conditions on the vertical shafts. The coordinate  $z$  in Equation 3.23 is considered positive in the direction of gravity and is zero at the top of the opening.

$$T(z_i) = \begin{cases} (285.93 - T_i) * e^{-\frac{z-15}{15z}} + T_i \text{ (K)} & z_i < 15 \text{ m} \\ 285.93 \text{ K} & z_i \geq 15 \text{ m} \end{cases} \quad (3.23)$$

### **3.4.2.5 Species Boundary Conditions**

The ATMOS 41 atmospheric pressure and atmospheric vapor pressure measurements were used to set up the openings' water vapor mass fraction boundary conditions. Equation 3.24 shows the relation between the water vapor mass fraction and the atmospheric pressure and atmospheric vapor pressure (Çengel et al., 2019). The value calculated with Equation 3.24 was directly used in the CFD solver.

$$Y_v = \frac{0.622 \frac{P_v}{P_{atm} - P_v}}{0.622 * \frac{P_v}{P_{atm} - P_v} - 1} (kg_{H_2O}/kg_{humid\ air}) \quad (3.24)$$

#### **3.4.2.5.1 Clear Water Stream Species Boundary Condition**

The wall that represents the clear water stream in the tunnel was considered saturated. In order to calculate the water vapor mass fraction in the clear water stream surface, Equation 3.24 was modified and rewritten, as is shown in Equation 3.25.

$$Y_{v,ws} = \frac{0.622 \frac{P_s(T_{ws})}{P_{abs} - P_s(T_{ws})}}{0.622 * \frac{P_s(T_{ws})}{P_{abs} - P_s(T_{ws})} - 1} (kg_{H_2O}/kg_{humid\ air}) \quad (3.25)$$

Equation 3.25 was implemented in a UDF. The CFD solver calculates the water vapor mass fraction in the clear water stream based on the estimated total pressure and temperature.

### **3.4.3 Computational Model Validation Procedure**

The simulated air circulation within the DigIndy tunnel was compared against the experimental results. The recorded values were examined each month from May 2020 to April 2021 to identify time segments with no-rain and no-fill conditions. The precipitations measurements were used to determine when it was raining or not. A value less than 1 mm/h is considered no-rain conditions, and any amount of precipitation greater than this threshold was considered rain conditions. After a rain, the tunnel fills, and the flow patterns within the tunnel are affected. Any data collected within 1 - 2 days of rain events were neglected. After 1 - 2 days of no-rain conditions, the tunnel was considered to be under no-fill conditions.

After marking the beginning of the time segment for no-rain and no-fill conditions, the precipitation data was checked for at least two additional days beyond the start of the time segment. If no precipitation was observed, data collected during this time window was selected as the month's no-rain and no-fill representative steady-state conditions. Over the time segment, the average surface weather station measurements, atmospheric pressure, atmospheric temperature, atmospheric vapor pressure, and atmospheric wind speed, were used as the input boundary conditions for the CFD model. The in-shaft weather station's average values were used as the validation data for the CFD outputs estimations (Figure 3.3, p. 42). The standard deviations over the time segment selected were used to determine the instrumentation readings' total uncertainty, which is explained in the following section.

#### **3.4.3.1 Experimental Measurement Uncertainty**

The uncertainty of measurements from the ATMOS 41, ATMOS 22, and ATMOS 14 was calculated based on the zeroth-order uncertainty depicted by Moffat (1988). The zeroth-order uncertainty calculation is shown in Equation 3.26.

$$\delta X_{i,0} = \left\{ (\delta X_{i,fixed})^2 + (2\sigma_{i,0})^2 \right\}^{\frac{1}{2}} \quad (3.26)$$

The term  $\delta X_{i,fixed}$  in Equation 3.26 represents the fixed bias calculated by comparing the instrument measure against a calibration scale. The manufacturer reported the fixed bias for the ATMOS 41, whereas the fixed biases for ATMOS 22 and ATMOS 14 were not reported and are considered zero. The instrument's accuracy was assumed as the term  $2\sigma_{i,0}$ . The former assumes that the manufacturer's accuracy has a confidence interval of 95% (Moffat, 1988). The instruments' fixed bias and precision are presented in Appendix A.

The uncertainty of the averaged experimental sample values was calculated considering the zeroth-order uncertainty as a fixed bias. This strategy is known as fossilization (Moffat, 1988). The uncertainty of the averaged experimental measurements was calculated, as is shown in Equation 3.27. The uncertainty was calculated using the corresponding value of the t-statistic given the number of samples  $n$  and degrees of freedom  $n-1$  for a confidence interval of 95%.

$$X = \left\{ (B_{x_i})^2 + (tS_{\bar{x}_i})^2 \right\}^{\frac{1}{2}} \quad (3.27)$$

$$B_{x_i} = \delta X_{i,0} \text{ (Equation 3.26) and } S_{\bar{x}_i} = \frac{S_{x_i}}{\sqrt{n}}$$

## **CHAPTER 4. RESULTS**

Experimental and CFD simulation results presented in this chapter are divided into two sections. Experimental results collected during the initial alignment (DRTC+ECT) phase of the DigIndy project are presented in Section 4.1, along with CFD model validation and discussion about the effect of seasonal conditions. After validation, the CFD model was exercised to investigate the effect of tunnel alignment. The numerical results and a discussion of the alignment effect are presented in Section 4.2.

### **4.1 Effect of Seasonal Condition**

The effect of seasonal conditions was studied for the initial alignment (DRTC+ECT) by exercising the CFD model under different atmospheric weather conditions. The surface weather station measurements were used as boundary conditions for the CFD model as described in Section 3.4 (p. 47). A discussion of the surface weather station experimental results is given in Section 4.1.1. After applying boundary conditions to the model, simulations were conducted to predict the air circulation patterns within the tunnel. The resulting output from the CFD simulations, presented in Section 4.1.2, includes velocity, temperature, and water vapor mass fraction. Model validation was then conducted by comparing the CFD outputs to the experimental measurements of the in-shaft stations. A discussion of seasonal effect and model validation is given in Section 4.1.3.

#### **4.1.1 Surface Weather Station Experimental Results**

The surface weather station experimental measurements were divided into monthly time segments from May 2020 to April 2021. Each monthly time segment was analyzed to identify a minimum two-day period with no-rain and no-fill conditions, as described in Section 3.4.3 (p. 66). Table 4.1 shows the identified time segments that fulfill the requirements for no-rain/no-fill conditions and the number of instantaneous time samples used in the averaging procedure for each no-rain/no-fill time segment. The resulting average values of atmospheric pressure, atmospheric temperature, wind speed, and atmospheric vapor pressure for the time segments

presented in Table 4.1 are shown in Figure 4.1. The measurements shown in Figure 4.1 are also presented in tabular form in Table D.1 to Table D.3 in Appendix D.

*Table 4.1. Dry weather times (no-rain/no-fill conditions).*

Month	Time segment			
	From	To	Duration (days)	Samples
May, 2020	5/11/2020 0:00	5/14/2020 0:00	3	864
June, 2020	6/16/2020 0:00	6/20/2020 0:00	4	1152
July, 2020	7/13/2020 0:00	7/15/2020 0:00	2	576
August, 2020	8/20/2020 0:00	8/23/2020 0:00	3	864
September, 2020	9/15/2020 0:00	9/23/2020 0:00	8	2304
October, 2020	10/8/2020 0:00	10/11/2020 0:00	3	864
November, 2020	11/5/2020 12:00	11/9/2020 12:00	4	1152
December, 2020	12/16/2020 0:00	12/19/2020 0:00	3	864
January, 2021	1/7/2021 0:00	1/12/2021 0:00	5	1440
February, 2021	2/6/2021 0:00	2/10/2021 0:00	4	1152
March, 2021	3/4/2021 0:00	3/8/2021 0:00	4	1152
April, 2021	4/13/2021 0:00	4/19/2021 0:00	6	1728

The surface weather station measurements were used to calculate momentum, thermal, and species boundary conditions for the CFD model. Specifically, the atmospheric pressure, atmospheric temperature, wind speed, and atmospheric vapor pressure were used to calculate the thermal pressure difference, wind suction pressure difference, and water vapor mass fraction in each opening. Table E.1 of Appendix E shows the calculated values used as boundary conditions for each month.

From the surface experimental measurements of Figure 4.1.a, the atmospheric pressure did not show any discernable pattern and remained nearly constant throughout the year at approximately 995 hPa. Inspection of Figure 4.1.a shows that there are small differences in atmospheric pressure between tunnel openings, therefore, small differences in static pressure. Before conducting CFD simulations, it was expected that the difference in static pressure

between openings would affect the natural air circulation, as discussed in the literature review in Section 2.2.1 (p. 28). For example, higher static pressure at one opening would drive flow toward another opening at lower static pressure. However, the uncertainty in the atmospheric pressure measurements was around  $\pm 100$  Pa. A closer inspection of Figure 4.1.a shows that the differences in atmospheric pressure between openings were within the error bars.

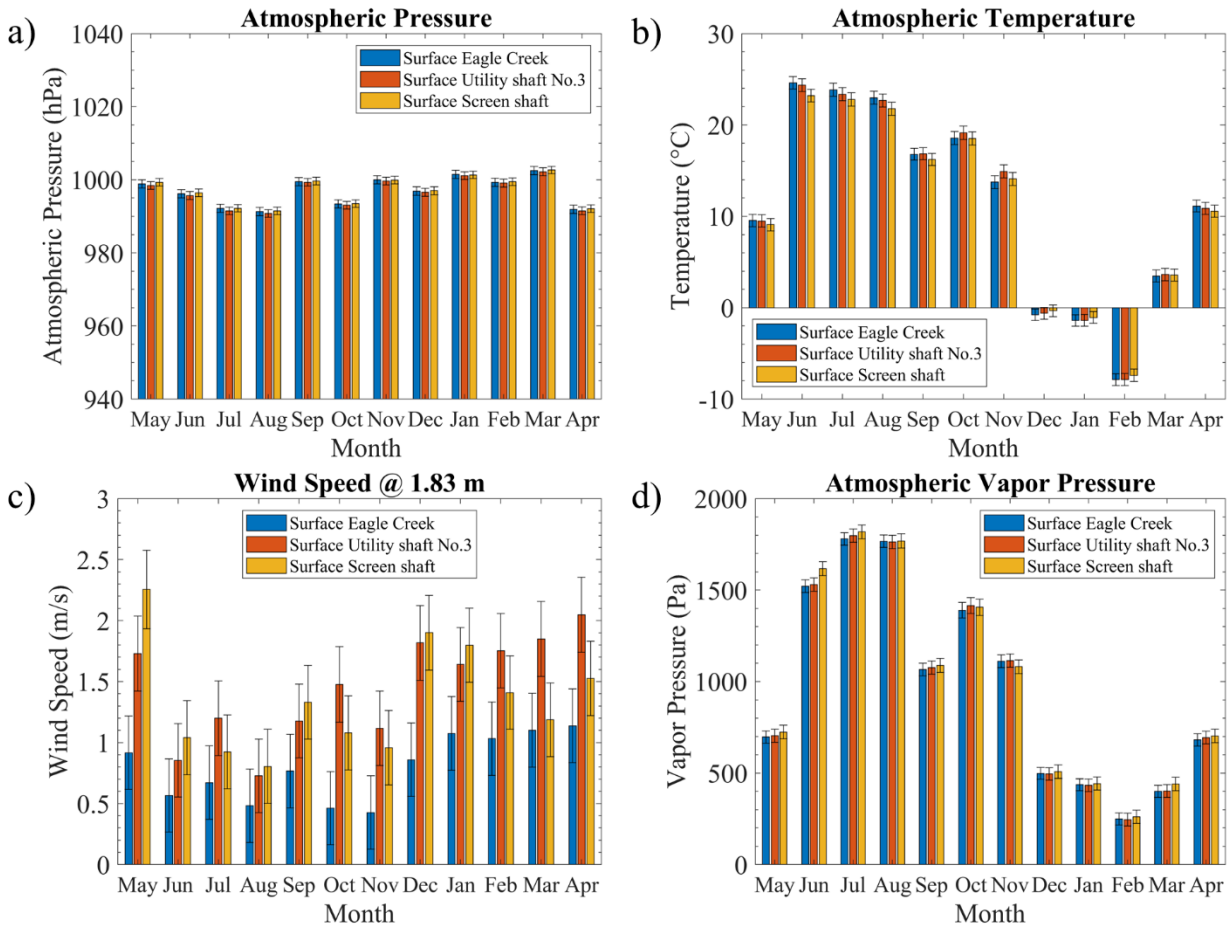


*Figure 4.1.* Atmospheric conditions in the DRTC+ECT alignment openings from May 2020 to April 2021: a) atmospheric pressure over the DRTC+ECT alignment openings, b) atmospheric temperature over the DRTC+ECT alignment openings, c) wind speed magnitude at 1.83 m over DRTC+ECT alignment openings, and d) atmospheric vapor pressure over the DRTC+ECT alignment openings.

During July 2020, for example, the atmospheric pressure difference between Eagle Creek and the screen shaft was approximately -4.8 Pa, and between utility shaft No.3 and screen shaft was approximately -69.7 Pa. Since the barometric readings include the difference in height between the locations, to find the static pressure, the hydrostatic or in this study, the thermal

potential difference pressure calculated for each location (Table E.1) needs to be subtracted. After subtracting the thermal potential difference pressure, the static pressure difference between Eagle Creek and the screen shaft is 56.3 Pa, and between utility shaft No.3 and screen shaft is 4.29 Pa. Both values were below the uncertainty of the instrumentation.

During CFD model development, it was found that applying the experimentally measured static pressure differences resulted in significant discrepancies in the air velocity within the tunnel. The discrepancies were attributed to errors in the applied static pressure differences. The instrumentation should have an uncertainty less than the measured static pressure difference between the openings, which was not possible with the selected instrumentation for this study. In a previous study, Apgar and Witherspoon found that the difference in static pressure between two sewer manholes, for a typical sewer system, was between 0 and 9 Pa (2009). To capture the difference in pressure between 0 and 9 Pa, the instrument should have an uncertainty of approximately 1 Pa, which suggests that instrumentation with a much higher resolution is needed for capturing static pressure differences between openings. For these reasons, the static pressure was considered zero for this study, as mentioned in Section 3.4.1.1.1 (p. 53).

Although the uncertainty of atmospheric pressure measurements was too large for applying static pressure differences to the model, the atmospheric pressure in each location was still used to calculate the density and water vapor mass fraction in each opening of the initial alignment. An uncertainty of  $\pm 100$  Pa in the atmospheric pressure yields an uncertainty of  $\pm 0.09\%$  for density and water vapor mass fraction calculations, which was considered acceptable for this study.

The atmospheric temperature in Figure 4.1.b shows a rise and a decrease in temperature as expected from seasonal conditions: spring (May, March, April), summer (June - August), fall (September - November), and winter (December - February). The maximum temperature was 24.6 °C in the Eagle Creek location in June, and the lowest temperature was -7.9 °C in the Eagle Creek location in February.

The wind speed measurements in Figure 4.1.c show larger values in the colder months (May and December - April) than the hotter months (June - November). The trend of wind speed throughout the year aligns with the average wind speeds reported by the National Weather Service for the city of Indianapolis from May 2020 to April 2021 (2021). Some local differences in wind speed were observed between the surface station locations. For example, the measured



wind speed in the Eagle Creek location was always lower than the other two locations. One possible reason for the reduced wind speed at Eagle Creek is because this location is in an urban area. In contrast, utility shaft No.3 and screen shaft are in open areas with a minimum number of houses and buildings.

The vapor pressure measurements in Figure 4.1.d show a similar pattern to the atmospheric temperature due to the seasonal condition. However, July and August show a larger humidity despite similar temperatures than June, around 24 °C.

#### **4.1.2 In-Shaft Station Experimental Results and Model Validation**

The CFD model was used to predict the vertical velocity, temperature, and water vapor mass fraction in the vertical shafts of the initial tunnel alignment: Eagle Creek vent shaft, Eagle Creek drop shaft, utility shaft No.3, and screen shaft from May 2020 through April 2021. As explained in Section 3.3.2 (p. 44), all in-shaft measurements were located at the geometric center of the vertical shaft except for the screen shaft. Due to machinery used to clean debris from the screen shaft, the instrumentation at this location was offset from the geometric center. All in-shaft weather stations were located six meters below surface level. To directly compare with experimental measurements, in-shaft data from CFD simulations are reported at the exact locations as their physical counterpart, including the offset of the screen shaft instrumentation.

##### **4.1.2.1 In-Shaft Vertical Velocity Results**

Figure 4.2 shows the experimental and numerically predicted vertical velocities in each shaft for the initial alignment. A positive value for vertical velocity means that the air is exhausted from the tunnel to the atmosphere. A negative value means that air is ingested from the atmosphere into the tunnel. The experimental measurements presented in Figure 4.2 are also tabulated in Table F.1 of Appendix F. In general, good agreement was observed between the experiments and numerically predicted vertical velocity.

The experimental measurements in Figure 4.2 show large values of negative vertical velocities in the coldest months (December - March) at the two Eagle Creek shafts and utility shaft No.3. The negative vertical velocities appear from September to November but at a reduced magnitude. In May and April, negative vertical velocities are only noticeable in Eagle Creek

shafts but not in utility shaft No.3. Comparing the CFD predictions with the experimental measurements at the Eagle Creek vent shaft (Figure 4.2.a) and drop shaft (Figure 4.2.b), the vertical velocities were predicted in the correct direction, except for September and October.

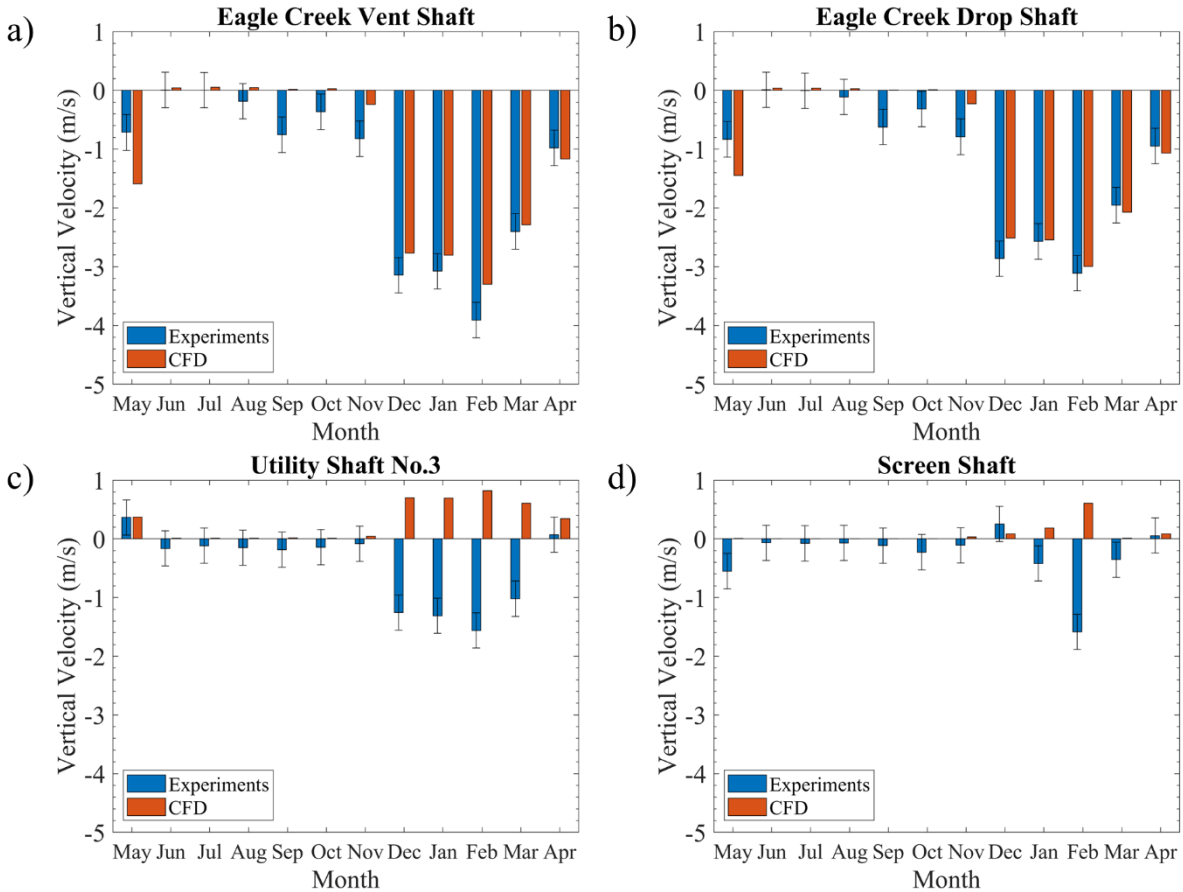


Figure 4.2. Experimental and CFD in-shaft vertical velocity results from May 2020 to April 2021: a) vertical air velocity in Eagle Creek vent shaft, b) vertical air velocity in Eagle Creek drop shaft, c) vertical air velocity in utility shaft No.3 shaft, and d) vertical air velocity in screen shaft.

As shown in Figure 4.2.c, utility shaft No.3 vertical velocity directions and magnitudes were correctly predicted within the instrument uncertainty, except for the coldest months (December – March). For the discrepancies observed in the coldest months, the CFD model predicts air exhausted from the utility shaft No.3, but experimental measurements show cold air ingesting into the tunnel.

The vertical velocity in the screen shaft, Figure 4.2.d, did not add valuable information for the analysis due to the offset position of the in-shaft weather station, as explained in Section

3.3.2 (p. 44). The offset of the instrumentation from the geometric center of the shaft made it susceptible to turbulent fluctuations and recirculation zones, which do not represent the true vertical velocity in the shaft. Therefore, the screen shaft vertical velocity is not used to infer the flow direction and magnitude. The temperature and water vapor mass fraction measurements, on the other hand, were a more reliable indicator for the flow direction at the screen shaft location. Flow direction at the screen shaft location was inferred from these two field variables, as described in the following section.

#### **4.1.2.2 In-Shaft Temperature Results**

Figure 4.3 shows the experimental in-shaft, surface temperature measurements, and the numerically predicted temperature values for the initial alignment. As with vertical velocity, good agreement was observed between experiments and the numerically predicted values.

Several of the temperature recording instruments (ATMOS 14 sensor) failed during the field measurement, most likely due to water infiltration into the sensor housing. Therefore, data reported in Figure 4.3 includes measurements from the anemometer ATMOS 22, which also includes an onboard temperature sensor. Before September, the in-shaft temperature measurements in the Eagle Creek vent shaft were taken with the ATMOS 14 and the remaining with the ATMOS 22. In the Eagle Creek drop shaft, the measurements before August were taken with the ATMOS 14 and the remaining with the ATMOS 22. For the screen shaft, the measurements starting from December were taken with the ATMOS 22. Finally, all the utility shaft No.3 measurements were taken with the ATMOS 14. The experimental measurements are presented in tabular format in Table F.2 of Appendix F.

Figure 4.3 shows that overall, all the temperature predictions agree with the seasonal temperature pattern. At the Eagle Creek location, Figure 4.3.a and Figure 4.3.b show that the measured and numerically predicted in-shaft temperature values were close to the atmospheric temperature measured at the surface. This observation supports the measured and numerically predicted vertical velocity values presented in Figure 4.2.a and Figure 4.2.b (p. 74). For example, in the winter months, the cold air at the surface is ingested into the tunnel leading to cold temperatures measured and predicted at the in-shaft stations.

The in-shaft temperature at utility shaft No.3 is shown in Figure 4.3.c. Good agreement was observed between numerically predicted and experimental results with the exception of the

months of December to March. The CFD model prediction shows a higher temperature during these months, around 12 °C, whereas the experimental value shows values below or close to zero. Comparing the in-shaft temperature in utility shaft No.3 against the surface temperature in this location, the experimentally measured temperature inside the vertical shaft is close to the measured temperature outside the shaft, suggesting that air is ingested into the tunnel. This observation supports the experimental vertical velocity measurements presented in Figure 4.2.c (p. 74), which show a negative velocity at utility shaft No.3 in the coldest months.

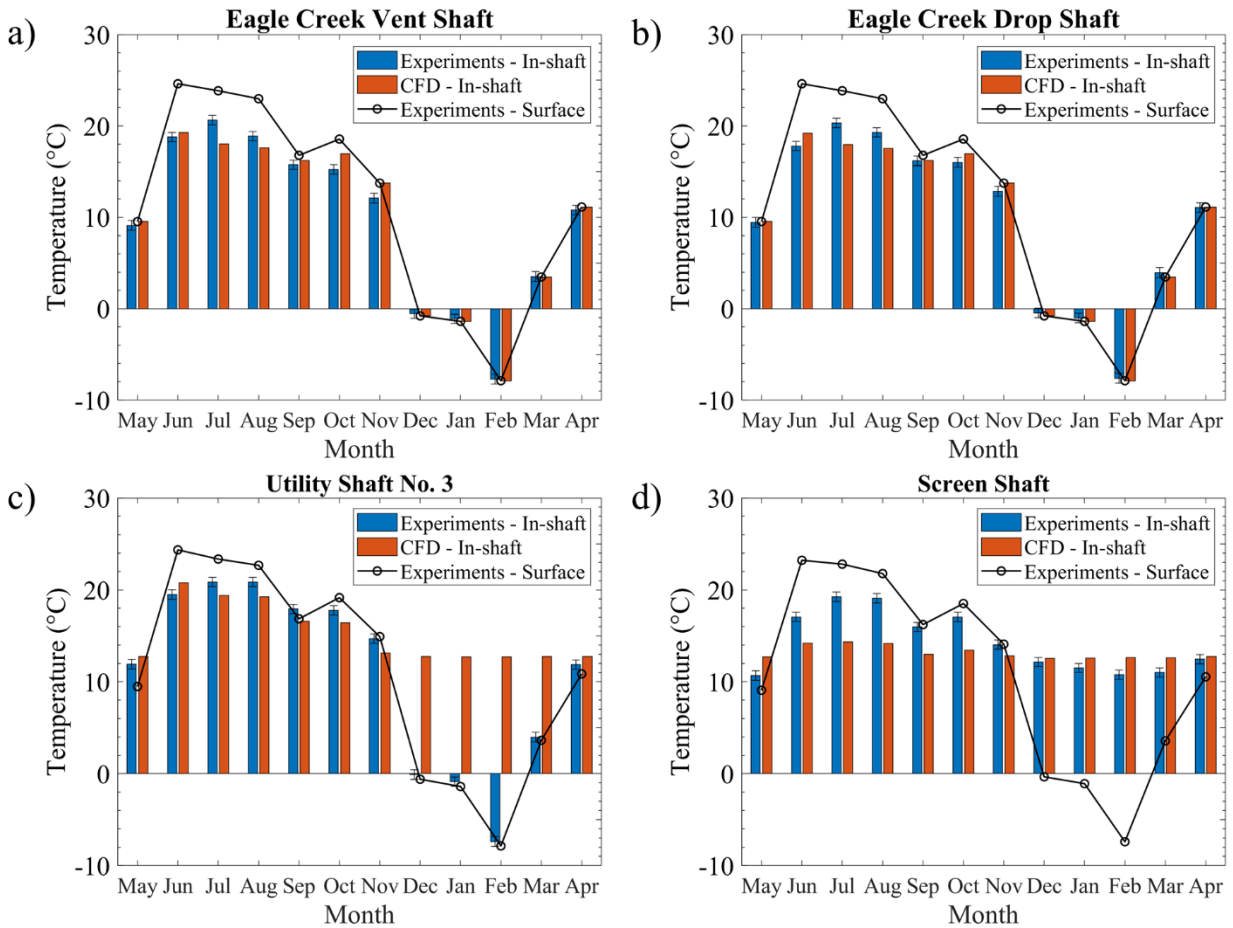


Figure 4.3. Surface experimental temperature measurements and experimental and CFD in-shaft temperature results, from May 2020 to April 2021: a) air temperature in Eagle Creek vent shaft, b) air temperature in Eagle Creek drop shaft, c) air temperature in utility shaft No.3 shaft, and d) air temperature in screen shaft.

The in-shaft temperature at the screen shaft location is shown in Figure 4.3.d. As mentioned in the previous section, in-shaft temperature measurements at this location were used to infer the flow direction rather than the vertical velocity measurement. For example, in the

winter months, both the numerically predicted and experimental temperatures were close to the constant temperature used for the tunnel's wall (12.78 °C, p. 65). Since the experimentally measured surface temperature was much lower, the in-shaft temperatures suggest that flow is exhausted at the screen shaft. This result is consistent with the vertical velocity CFD predictions at the screen shaft in the colder months, shown previously in Figure 4.2.d (p. 74).

#### **4.1.2.3 In-Shaft Water Vapor Mass Fraction Results**

Figure 4.4 presents the in-shaft and surface experimental water vapor mass fraction values for each opening, as well as the CFD predictions. Again, good agreement was observed between experimental numerically predicted values. As explained in the previous section, three of the four ATMOS 14 sensors failed during the data collection. Therefore, the data in Figure 4.4 is incomplete. The ATMOS 14 in utility shaft No.3 was the only sensor that did not fail and recorded all twelve months.

Figure 4.4.a through Figure 4.4.c shows that the two Eagle Creek shafts and utility shaft No.3 in-shaft measurements and predictions follow the atmospheric water vapor mass fraction pattern with good agreement. As with the vertical velocity and temperature, however, the CFD prediction in utility shaft No.3 from December to March shows a discrepancy with experimental measurements of water vapor mass fraction. The discrepancy in the vertical velocity causes the discrepancy in the water vapor mass fraction. On the contrary, for the screen shaft location (Figure 4.4.d), the experimental in-shaft water vapor mass fraction was larger than the outside water vapor mass fraction almost during all the months. The larger water vapor mass fraction at the screen shaft location is due to its downstream location. The screen shaft receives the total accumulated clear water that has infiltrated throughout the length of the tunnel. The standing clear water at the bottom of the screen shaft location, which is not captured in the CFD model, may lead to a larger experimental measurement of water vapor mass fraction.

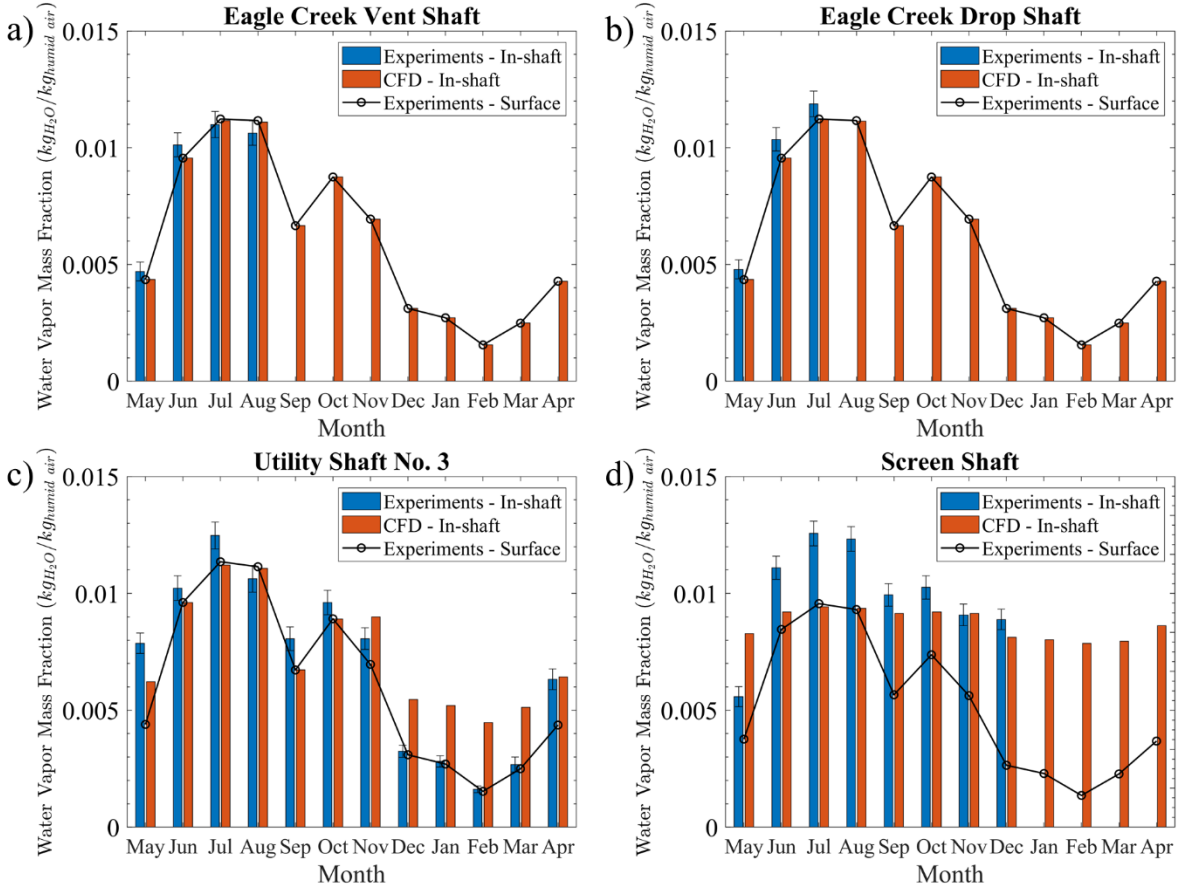


Figure 4.4. Surface experimental water vapor mass fraction measurements and experimental and CFD in-shaft water vapor mass fraction results, from May 2020 to April 2021: a) water vapor mass fraction in Eagle Creek vent shaft, b) water vapor mass fraction in Eagle Creek drop shaft, c) water vapor mass fraction in utility shaft No.3 shaft, and d) water vapor mass fraction screen shaft.

#### 4.1.3 Discussion of Seasonal Effect and Model Validation

Overall, the CFD model showed good agreement with experimental results. Comparisons of vertical velocity, temperature, and water vapor mass fraction showed that the direction and magnitude of air circulation patterns were captured reasonably well. For example, the CFD model predicted larger flow rates in colder months and lower flow rates in warmer months, which matched the experimental results. Furthermore, the CFD model predicted that air ingestion occurs at the Eagle Creek drop shaft and Eagle Creek vent shaft, which agreed with the experimental results.

#### **4.1.3.1. Sinking Effect**

The observed flow magnitude and circulation direction are attributed to a sinking effect caused by temperature-induced buoyancy forces. In the colder months, the atmospheric air is colder, denser than the air in the tunnel. The density gradient creates an unstable condition that tends to sink the air downwards into the tunnel. However, as cold air sinks into the tunnel, the mass balance must be conserved by air displacement out of another tunnel opening. There may be a balance of forces for static conditions where the cold air pushing down at one tunnel opening may be balanced by the cold air pushing down at another tunnel opening. One factor that tips the balance and creates a driving flow is the clear water stream infiltrating the tunnel and traveling south towards the screen shaft. The drag force from the clear water stream may assist the sinking effect. For example, cold air at Eagle Creek, which sinks into the tunnel, is assisted by the clear water stream moving towards the screen shaft.

During warmer months, the atmospheric air is warmer and less dense than the air inside the tunnel creating a stable condition. The outside air with a larger temperature than the air in the tunnel, approximately 12.78 °C, tends to be outside and the colder air inside the tunnel tends to stay inside. Flow during warm conditions is mainly attributed to internal factors inside the tunnel, as the evaporation and condensation processes and the clear water stream drag force. The clear water stream drags the air horizontally towards the screen shaft. In contrast, the condensation and evaporation process change the density by removing and adding water vapor, creating a difference of densities that leads to a vertical circulation.

#### **4.1.3.1. Discrepancy at Utility Shaft No.3**

The discrepancy in the vertical velocity results at Eagle Creek and utility shaft No.3, especially in the flow direction, can be for several reasons. During CSO events, objects are carried into the tunnel and obstruct the airflow, as mentioned in the project's limitations (p. 24). Also, sediments in the bottom of the tunnel can change the pressure drop across the tunnel. Moreover, during the coldest months, December to February, the melted snow creates a source of clear water in the CSS and may influence the airflow and temperature distribution within the tunnel. The effects of obstructions, sediments, and snow melting were not considered in the present work. Additionally, differences in static pressure between the openings (which were not

captured due to the experimental uncertainty of the instruments used) may also contribute to the difference between numerical predictions and experimental measurements.

Another possibility leading to a discrepancy between vertical velocity predictions and experiments is that the tunnel wall temperature is not necessarily constant, as was defined in the assumptions (p. 23). The soil surrounding the tunnel can store and release heat into the air (Liu et al., 2014). Depending on the airflow or wastewater temperature flowing during CSO events, the tunnel wall temperature has a non-uniform distribution across the tunnel length (Liu et al., 2014).

The effect of non-uniform temperature distribution along the deeply buried tunnel was investigated by Liu et al. (2014). The authors developed a transient heat transfer 1D model to predict the air temperature and relative humidity in an underground ventilation tunnel. They found that the wall temperature has a non-uniform distribution, and it has a specific profile due to the tunnel's characteristics, airflow, and seasonal cycling. In order to find the temperature profile, they set up an initial constant value in the wall, and they simulated the case for six months. After the sixth month, the 1D model prediction was compared against the experimental measurement. Results show that ventilation rates were dependent on the tunnel's wall temperature. In order to determine if non-uniform wall temperature distribution plays a role in the present work, a series of numerical experiments were conducted. The model setup and results are presented in the following section.

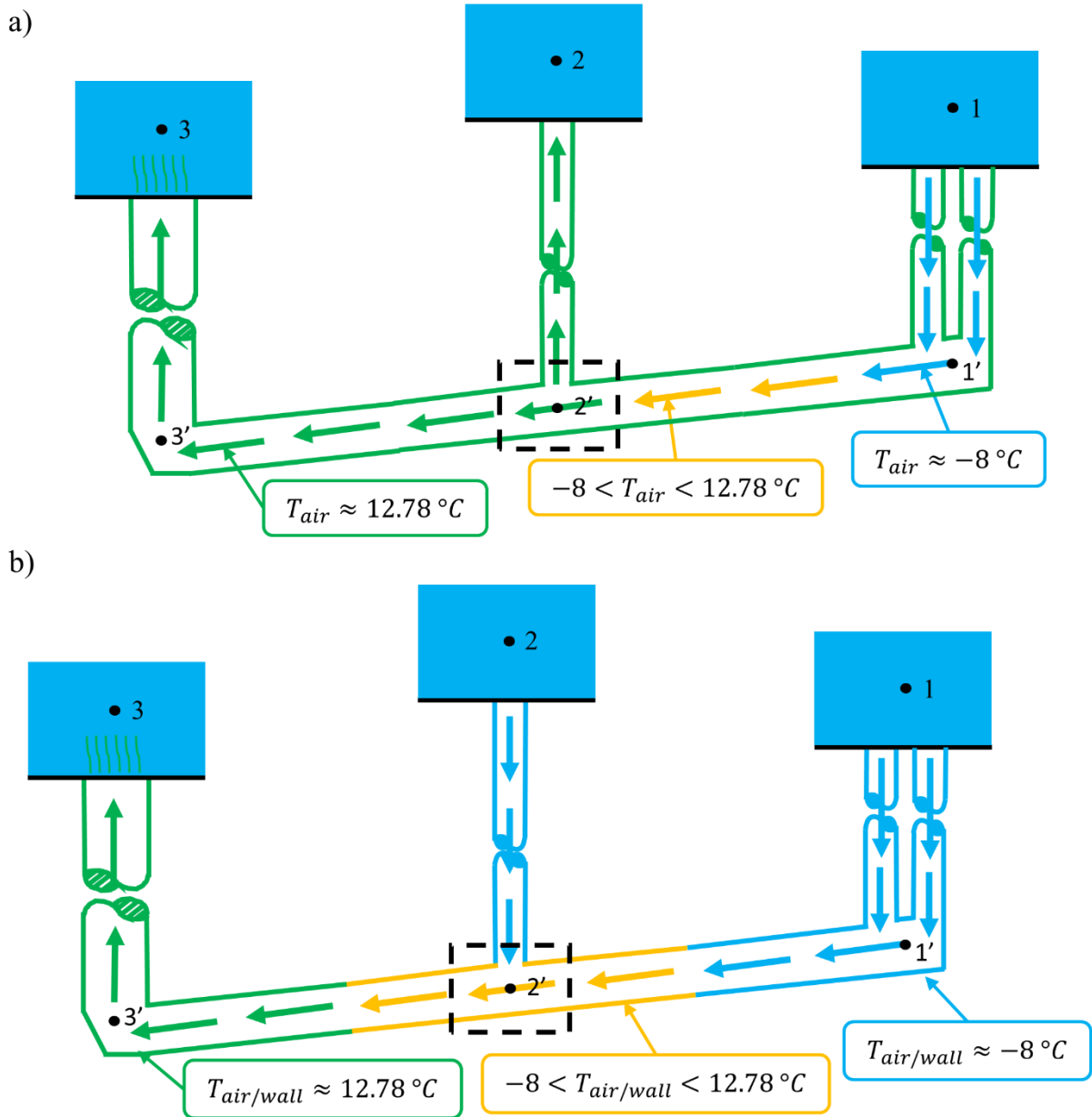
#### **4.1.3.1. Longitudinal Temperature Distribution from Cold Air Ingestion**

During the coldest months, December to March, the air is ingested into the tunnel through the Eagle Creek vent shaft and the Eagle Creek drop shaft, as shown in the experimental results in Figure 4.2.a and Figure 4.2.b (p. 74). The air temperature ingested into the tunnel is below 12.78 °C, approximately -0.5 °C in December, -1 °C in January, -8 °C in February, and 4 °C in March. Because the air is at a lower temperature than the soil temperature, 12.78 °C, the cold air ingestion will cool the tunnel wall.

Figure 4.5.a shows a schematic example of the air temperature distribution throughout the tunnel for February for the scenario with constant wall temperature, which was defined for this study in the assumptions (p. 23). On the other hand, Figure 4.5.b shows a schematic example of the air and wall temperature distribution throughout the tunnel for February for the scenario with non-uniform wall temperature. Looking at Figure 4.5.a and Figure 4.5.b, the location number one



represents Eagle Creek location, location two the utility shaft No.3, and location three the screen shaft.



When the air is ingested through the Eagle Creek vent shaft and the Eagle Creek drop shaft in location 1, the air exchanges heat with the wall through convection and conduction. For the scenario shown in Figure 4.5.a, with a constant wall temperature, only the air changes

temperature. Contrarily, in Figure 4.5.b, the temperature of both the air and the tunnel wall are changing. With a constant wall temperature, the air reaches the soil temperature faster than the case where the tunnel wall temperature has a non-uniform distribution.

A consequence of the heat exchange between the air and the wall is manifest in the location where the air temperature comes to equilibrium with the wall. Consider the control volume around location 2' as shown in Figure 4.5.a and Figure 4.5.b. Looking at Figure 4.5.a, the air reaches soil temperature before or close to location 2'. For this case, a difference in air temperature inside the horizontal section of the tunnel is only seen between 1' and 2'. The temperature difference creates a buoyancy force pointing from 1' to 2' due to density difference, which generates a higher pressure in the control volume interface between 1' and 2'. The flow in the interface has to find equilibrium between the interface between 2' and 2 and the interface between 2' and 3'. From the CFD results in Figure 4.2, the equilibrium leads to airflow from 2' to 2 and from 2' to 3'.

On the other hand, in Figure 4.5.b, the air reaches soil temperature after the location 2'. For this case, a difference in air temperature inside the horizontal section of the tunnel is seen between 1' and 2' and between 2' and 3'. The temperature difference creates a buoyancy force pointing from 1' to 2' and from 2' to 3'. For the former scenario, the buoyancy force assists the flow moving from 2' to 3' where there was no assisting force in Figure 4.5.a. Furthermore, there is a larger temperature difference between 2 and 2' in Figure 4.5.a than in Figure 4.5.b. More concisely, the temperature at 2' is lower, and the air is denser in Figure 4.5.b. The reduced temperature difference in Figure 4.5.b results in a reduced buoyancy force acting in the downward direction at location 2'.

To test the hypothesis that decreased wall temperature from cold air ingestion affects the airflow pattern, a linear temperature profile was applied to the tunnel wall instead of the previously assumed constant wall temperature. The linear temperature profile was defined using linear interpolation along the length of the DRCT+ECT tunnel alignment. The linear interpolation was applied along the Y-direction presented in Figure 4.6. Because cold air was ingested at Eagle Creek, the interpolation was calculated using the surface weather station temperature at the Eagle Creek location, labeled  $T_{\text{Eagle Creek}}$  in Figure 4.6, and using the soil temperature, 12.78 °C, at the screen shaft location.

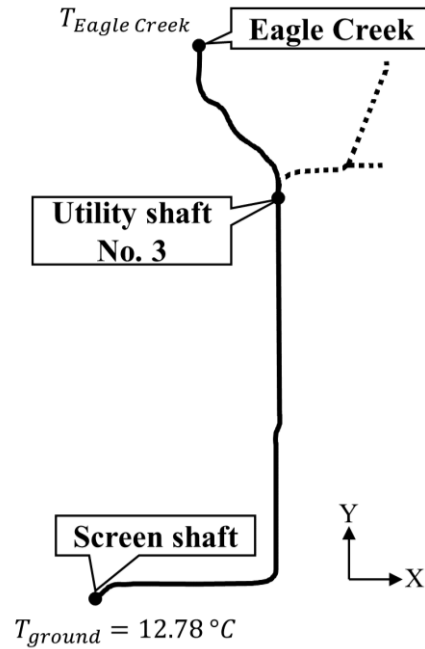


Figure 4.6. Considerations for linear temperature profile in the tunnel.

Figure 4.7 compares the vertical velocity results in the Eagle Creek vent shaft, Eagle Creek drop shaft, utility shaft No.3, and screen shaft from the linear profile in the CFD model against the experimental and CFD results shown in Figure 4.2 (p. 74). Figure 4.7.a and Figure 4.7.b show that the linear temperature profile does not substantially change the vertical velocity at the Eagle Creek vent shaft and Eagle Creek drop shaft. On the other hand, Figure 4.7.c shows that linear temperature profile results in a much better agreement of vertical velocity at utility shaft No.3. The flow direction changed from exhausting to ingesting, and the magnitude matched the experimental results with substantially better accuracy.

A comparison of numerically predicted and experimental temperatures is shown in Figure 4.8. Figure 4.8.a, Figure 4.8.b, and Figure 4.8.d show that the temperature predictions in the Eagle Creek vent shaft, the Eagle Creek drop shaft, and screen shaft do not change with the two wall temperature distributions. Because the use of the linear temperature profile resulted in the correct flow direction at utility shaft No.3, the numerically predicted temperatures were in better agreement with experiments, as shown in Figure 4.8.c.

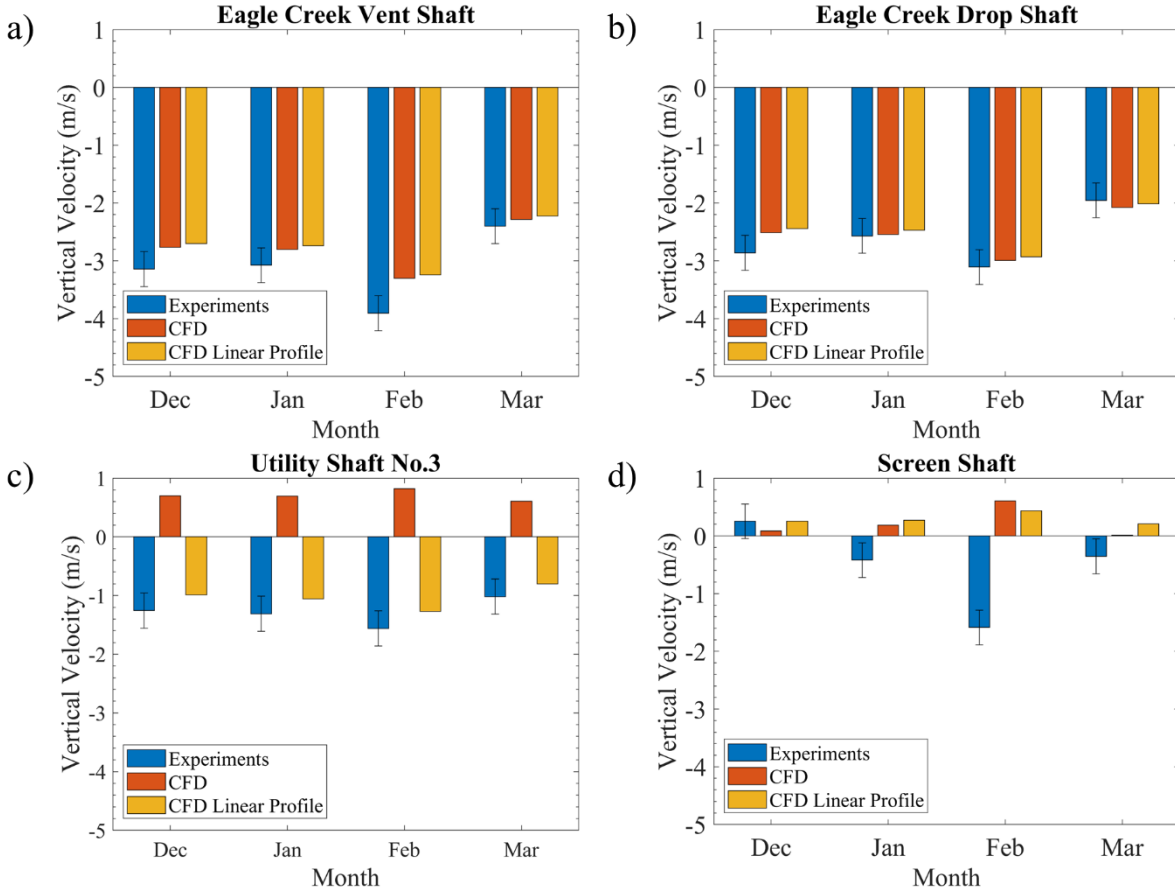


Figure 4.7. Experimental, CFD, and CFD linear profile in-shaft vertical velocity results from December 2020 to March 2021: a) vertical air velocity in Eagle Creek vent shaft, b) vertical air velocity in Eagle Creek drop shaft, c) vertical air velocity in utility shaft No.3 shaft, and d) vertical air velocity in screen shaft.

Figure 4.9 compares the numerically predicted and experimental water vapor mass fraction. Figure 4.9.a and Figure 4.9.b show that the water vapor mass fraction predictions in the Eagle Creek vent shaft and the Eagle Creek drop shaft do not change using the linear profile. As with the numerically predicted temperatures, the numerically predicted water vapor mass fraction showed better agreement with experiments at utility shaft No.3 because the flow direction is captured correctly using the linear temperature profile. The improvement in water vapor mass fraction prediction is shown in Figure 4.9.c.

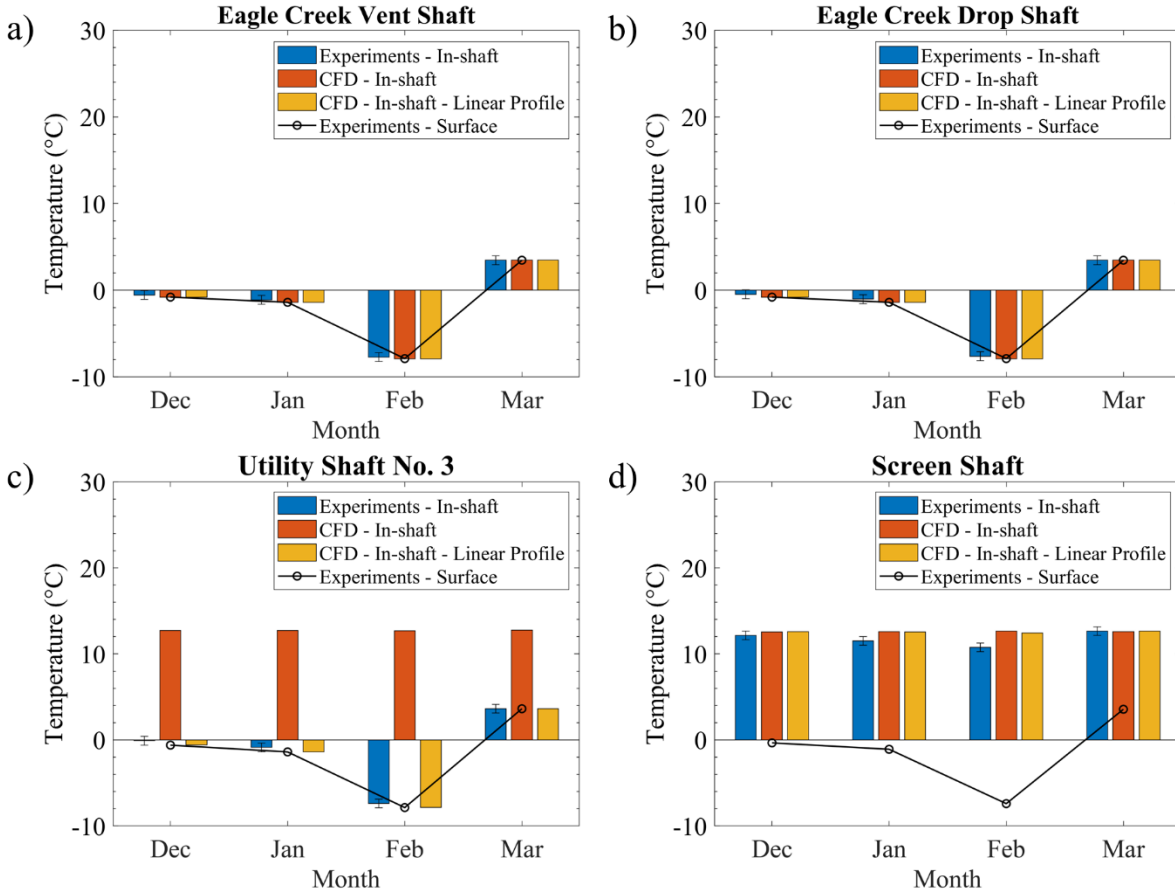


Figure 4.8. Surface experimental temperature measurements and experimental, CFD, and CFD linear profile in-shaft temperature results, from December 2020 to March 2021: a) air temperature in Eagle Creek vent shaft, b) air temperature in Eagle Creek drop shaft, c) air temperature in utility shaft No.3 shaft, and d) air temperature in screen shaft.

The CFD prediction in Figure 4.7, Figure 4.8, and Figure 4.9 show that the temperature distribution in the tunnel wall plays an important role in predicting the correct vertical velocity, temperature, and water vapor mass fraction. Accounting for wall temperature distribution only applied to the colder months because the atmospheric temperature during these months was constantly below the soil temperature, 12.78 °C. The increased air density outside the tunnel creates a temperature-driven buoyancy force, leading to cold air ingestion into the tunnel.

During warmer months, there is generally less air circulation in the tunnel. Therefore, there is no significant hot air ingestion into the tunnel and no significant heat transfer with the tunnel wall. The temperature in the tunnel is stable, and the assumption of constant wall temperature equal to the soil temperature is valid. Intermediate conditions in spring and fall must

be considered carefully and are likely subjected to dynamic effects where transient analysis is necessary.

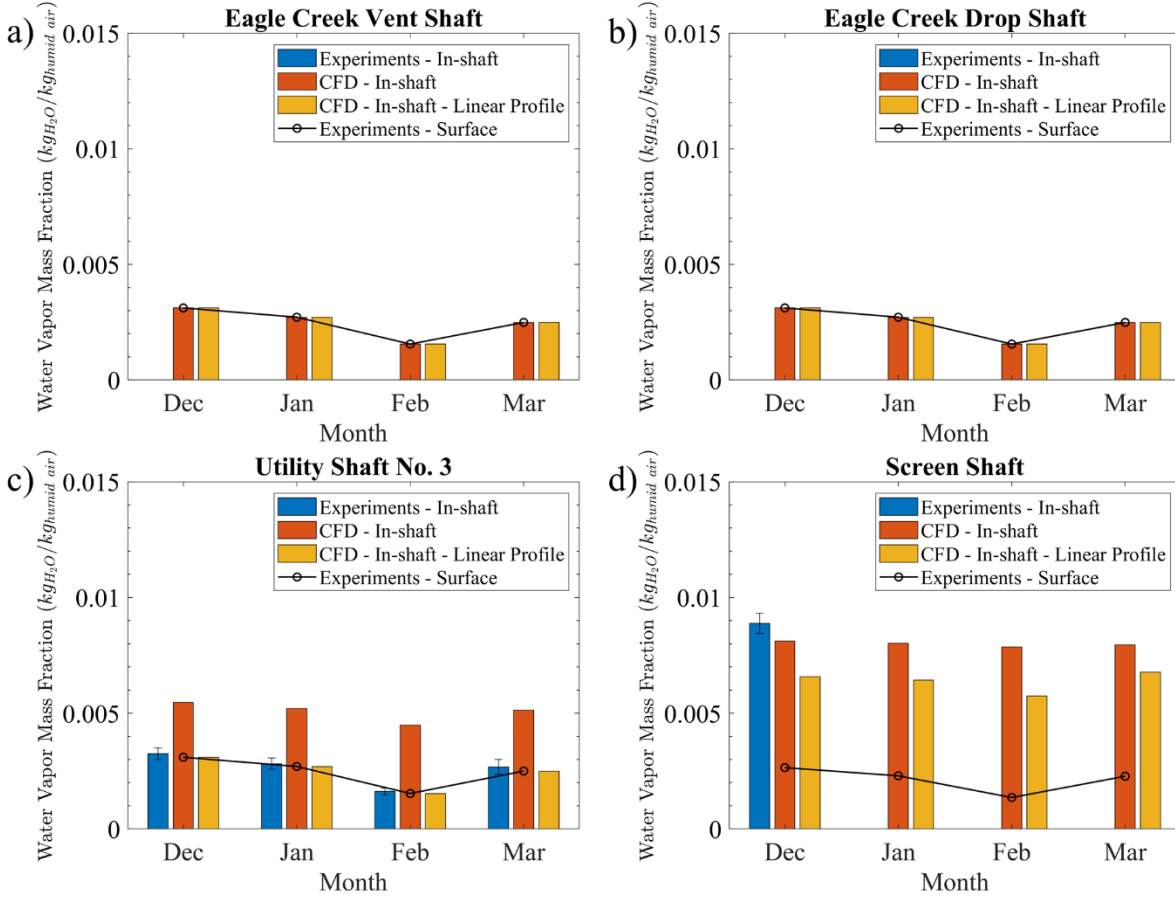


Figure 4.9. Surface experimental water vapor mass fraction measurements and experimental, CFD, and CFD linear profile in-shaft water vapor mass fraction results, from December 2020 to March 2021: a) water vapor mass fraction in Eagle Creek vent shaft, b) water vapor mass fraction in Eagle Creek drop shaft, c) water vapor mass fraction in utility shaft No.3 shaft, and d) water vapor mass fraction screen shaft.

Despite the discrepancy in utility shaft No.3 for the coldest months, December to March, the author considers that the CFD model captures the seasonal effect correctly. The CFD model and the modeled physics can be considered validated and used for future alignments.

## **4.2 Effect of Tunnel Alignment**

After validating the CFD model across the range of seasonal conditions, the numerical procedure was extrapolated for the future alignments of the DigIndy tunnel. Since data were not

available to calculate boundary conditions for the future alignments, a strategy was developed in Section 4.2.1 to synthesize representative boundary conditions for simulating flow in the future tunnel alignments. CFD results are presented for the initial alignment (Section 4.2.2), second alignment (Section 4.2.3), third alignment (Section 4.2.4), and fourth alignment (Section 4.2.5). Finally, a discussion of the effect of tunnel alignment is given in Section 4.2.6.

#### 4.2.1 Boundary Conditions for Future Alignments

The analysis of seasonal effect showed that temperature-induced buoyancy forces play a major role in the natural air circulation within the DigIndy tunnel. During colder months, the denser air outside the tunnel sinks into the tunnel and leads to large magnitudes of air circulation. During warmer months, the air outside the tunnel is less dense, and there is no sinking effect to drive flow in the tunnel. Based on this observation, two different conditions were considered to analyze the future alignments: a cold condition and a warm condition. The coldest conditions represent the conditions of the more extensive air circulation produced by the atmospheric conditions, winter months, and the warmer conditions represent the more stable conditions in the tunnel, summer months.

The cold condition parameters were selected to represent February 2021 conditions where the highest sinking effect was seen in the Eagle Creek vent shaft and the Eagle Creek drop shaft, as shown in Figure 4.2.a and Figure 4.2.b (p. 74). Table 4.2 presents the values used to set up the cold condition simulation for the different tunnel alignments.

Table 4.2. Value configurations for cold conditions simulations.

Parameter	Value	Opening
$\Delta P_g$ (Pa)	0	All openings
$W$ (m/s)	0	All openings
$T$ (°C)	-8	All openings
$P_{atm}$ (hPa)	999.479	All openings
$RH$ (%)	50	All openings
$Y_v$ ( $kg_{H_2O}/kg_{humidair}$ )	$9.643 \times 10^{-4}$	All openings
$\rho$ ( $kg/m^3$ )	1.313	All openings

The warm condition parameters were selected to represent July 2020, shown in Figure 4.1 (p. 71). Table 4.3 shows the values used to set up the warm condition simulations for the different tunnel alignments.

Table 4.3. Value configurations for warm conditions simulations.

Parameter	Value	Opening
$\Delta P_g$ (Pa)	0	All openings
$W$ (m/s)	0	All openings
$T$ (°C)	24	All openings
$P_{atm}$ (hPa)	992.200	All openings
$RH$ (%)	50	All openings
$Y_v$ ( $kg_{H_2O}/kg_{humid\ air}$ )	$9.400 \times 10^{-3}$	All openings
$\rho$ ( $kg/m^3$ )	1.159	All openings

#### 4.2.2 Initial Alignment Effect (DRTC+ECT)

To analyze the effect of tunnel alignment, the cold and warm conditions described in the previous section were applied to the initial alignment: DRTC+ECT, to obtain a control case for comparison with the three future alignments. Table 4.4 shows the mass flow, vertical velocity, temperature, and water vapor mass fraction predictions in the initial alignment for the cold conditions.

Table 4.4. DRTC+ECT alignment cold conditions results.

Cold conditions				
Opening	Mass flow ( $kg/s$ )	Vertical velocity ( $m/s$ )	Temperature (°C)	Mass fraction ( $kg_{H_2O}/kg_{humid\ air}$ ) ( $1 \times 10^{-4}$ )
Screen shaft	-32.646	0.594	12.641	77.690
Utility shaft No.3	-3.491	0.933	12.292	41.280
Eagle Creek vent shaft	18.461	-3.293	-8.006	9.640
Eagle Creek drop shaft	17.679	-2.987	-8.004	9.640

The vertical velocity, temperature, and water vapor mass fraction are local flowfield values taken at the exact physical location of the in-shaft measurement stations, as discussed



previously in Section 3.3.2 (p. 44). On the other hand, the air mass flow was calculated as the surface integral of mass flux across the face of the opening. A positive mass flow value means that the system gains mass through that opening (flow is ingested into the tunnel). A negative mass flow value means that the system loses mass through that opening (flow is exhausted from the tunnel).

The sign convention for vertical velocity is opposite that of mass flow. A positive vertical velocity means that the air is flowing opposite to the gravity direction (upwards). A negative vertical velocity means that the air is flowing in the direction of gravity (downwards). Typically, a positive vertical velocity suggests that flow is exhausted, and a negative vertical velocity suggests that flow is ingested. However, the direction of flow indicated by vertical velocity may not always match the mass flow. For example, a recirculation zone can appear in the vertical shafts, resulting in a positive vertical velocity (locally upward point value) and a positive mass flow (ingesting air). The mass flow in the surface of the opening must be used, instead of vertical velocity, to determine if the flow is exhausting or ingesting at a given location.

The mass flow predictions in Table 4.4 indicate that the flow is ingested into the tunnel through the Eagle Creek vent shaft and the Eagle Creek drop shaft, and the flow is exhausted through utility shaft No.3 and screen shaft. The predictions in vertical velocity, temperature, and the water vapor mass fraction are similar to the predicted in February, shown previously in Figure 4.2 (p. 74).

Table 4.5 shows the mass flow, vertical velocity, temperature, and water vapor mass fraction predictions in the initial alignment for the warm conditions. The mass flow predictions in Table 4.5 indicate that the flow is ingested into the tunnel through the Eagle Creek vent shaft, the Eagle Creek drop shaft, and utility shaft No.3, and that the flow is exhausted through screen shaft.

Table 4.5. DRTC+ECT alignment warm conditions results.

Warm conditions				
Opening	Mass flow (kg/s)	Vertical velocity (m/s)	Temperature (°C)	Mass fraction ( $kg_{H_2O}/kg_{humid\ air}$ ) ( $1 \times 10^{-4}$ )
Screen shaft	-0.553	0.001	14.322	92.220
Utility shaft No.3	0.106	0.013	20.782	94.000
Eagle Creek vent shaft	0.200	0.044	18.920	94.000
Eagle Creek drop shaft	0.167	0.034	18.853	94.000

To compare the effect of season effect in terms of standardized volumetric flow rate units, the mass flow in Table 4.4 and Table 4.5 was expressed in standard cubic feet per minute (SCFM). To calculate the SCFM, the standard: atmospheric pressure of 101325 Pa, the temperature of 19 °C, and the relative humidity of 36 %, was used. Figure 4.10 shows the SCFM results for the cold and warm conditions in the DRTC+ECT alignment. It should be noted that the reported SCFM values will differ slightly from the actual cubic feet per minute (ACFM) since the pressure and temperature in the tunnel differ from the standard conditions.

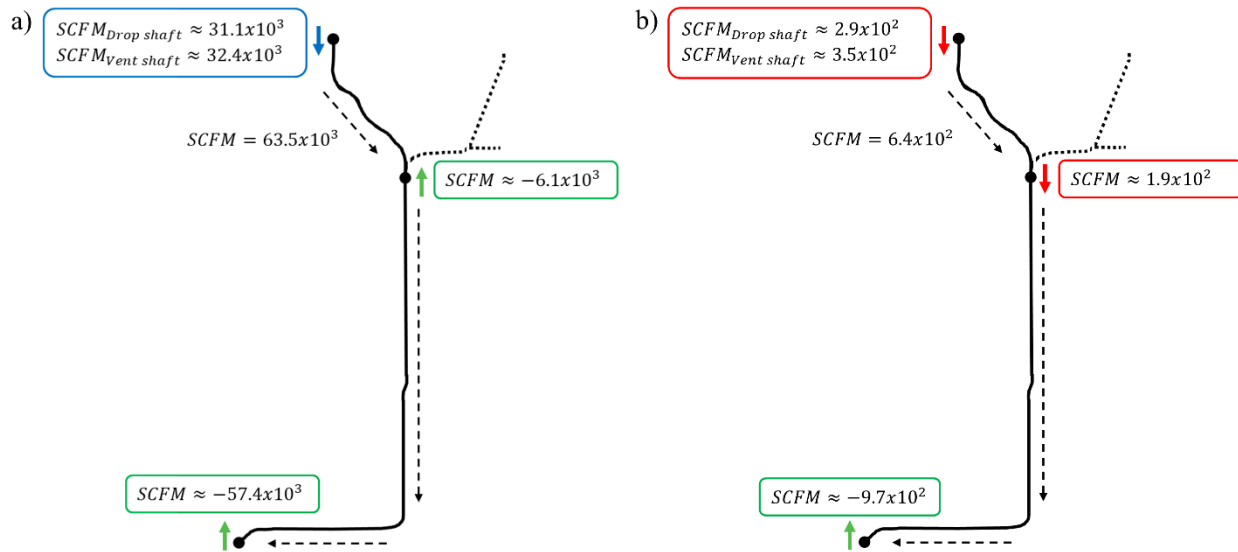


Figure 4.10. SCFM predictions for the DRTC+ECT alignment: a) cold conditions and b) warm conditions.

Looking at Figure 4.10, the black circles represent the tunnel openings. At Eagle Creek (northernmost opening), the circle represents both the vent shaft and the drop shaft, as mentioned

in Section 3.2.1 (p. 37). The arrows close to each black circle represent if the air is ingested into the tunnel, an arrow pointing downwards, or if the air is exhausted, an arrow pointing upwards, in that opening. The green color in Figure 4.10 means that the air in that location is approximately the tunnel air temperature, i.e., 12.78 °C. The blue color means that the air in that location has a lower temperature than the tunnel air temperature. A red color means that the air has a higher temperature than the tunnel air temperature in that location. Finally, the dotted black lines in Figure 4.10 represent the mass flow direction inside the tunnel.

Figure 4.10 shows that in both conditions, the air is exhausted in the screen shaft and that the mass flow in the cold conditions is between one and two orders of magnitude larger than the mass flow in warm conditions. Additionally, the utility shaft No.3 mass flow is different for each condition, exhausting air during cold conditions and adding air in warm conditions.

#### 4.2.3 Second Alignment Effect (DRTC+ECT+WRT+LPgRT)

The second alignment, DRTC+ECT+WRT+LPgRT, consists of the initial alignment plus two more openings, LP vent shaft and WR vent shaft, as shown in Figure 3.9.b (p. 59). Table 4.6 shows the mass flow, vertical velocity, temperature, and water vapor mass fraction predictions in the second alignment for the cold conditions. Notice that the mass flow magnitude in the Eagle Creek vent shaft and the Eagle Creek drop shaft was increased with respect to the initial alignment and that the mass flow was reduced in utility shaft No.3 and screen shaft.

Table 4.6. DRTC+ECT+WRT+LPgRT alignment cold conditions results.

Cold conditions				
Opening	Mass flow ( $kg/s$ )	Vertical velocity ( $m/s$ )	Temperature ( $^{\circ}C$ )	Mass fraction ( $kg_{H_2O}/kg_{humid\ air}$ ) ( $1 \times 10^{-4}$ )
Screen shaft	-18.378	0.201	12.369	78.850
Utility shaft No.3	-2.267	0.564	11.776	44.490
Eagle Creek vent shaft	23.879	-4.239	-8.008	9.640
Eagle Creek drop shaft	22.874	-3.849	-8.007	9.640
LP vent shaft	-13.859	2.808	12.775	87.310
WR vent shaft	-12.248	2.417	12.776	89.120

Table 4.7 shows the mass flow, vertical velocity, temperature, and water vapor mass fraction predictions in the second alignment for the warm conditions. The mass flows presented in Table 4.7 show that all openings are ingesting air into the tunnel and exhausting at the screen shaft. Moreover, shafts contributing more to the airflow are the LP vent shaft and the WR vent shaft.

*Table 4.7. DRTC+ECT+WRT+LPgRT alignment warm conditions results.*

Warm conditions				
Opening	Mass flow ( $kg/s$ )	Vertical velocity ( $m/s$ )	Temperature ( $^{\circ}C$ )	Mass fraction ( $kg_{H_2O}/kg_{humid\ air}$ ) ( $1 \times 10^{-4}$ )
Screen shaft	-1.079	-0.002	13.822	92.170
Utility shaft No.3	0.072	-0.013	19.695	94.000
Eagle Creek vent shaft	0.158	0.037	18.264	94.000
Eagle Creek drop shaft	0.130	0.044	18.080	94.000
LP vent shaft	0.385	-0.036	21.478	94.000
WR vent shaft	0.277	-0.001	21.049	94.000

Figure 4.11 presents the comparison between the cold and warm conditions in the second alignment in SCFM. Figure 4.11.a shows that the air is ingested into the tunnel through the Eagle Creek location and exhausting in the other openings for the cold conditions. Due to air exhaust from the LP working shaft and WR vent shaft, the air ingestion at Eagle Creek was increased relative to the first alignment. Under warm conditions, Figure 4.11.b shows that the flow goes from all the openings towards the screen shaft, following the clear water stream direction, increasing the mass flow in the screen shaft with respect to the initial alignment.

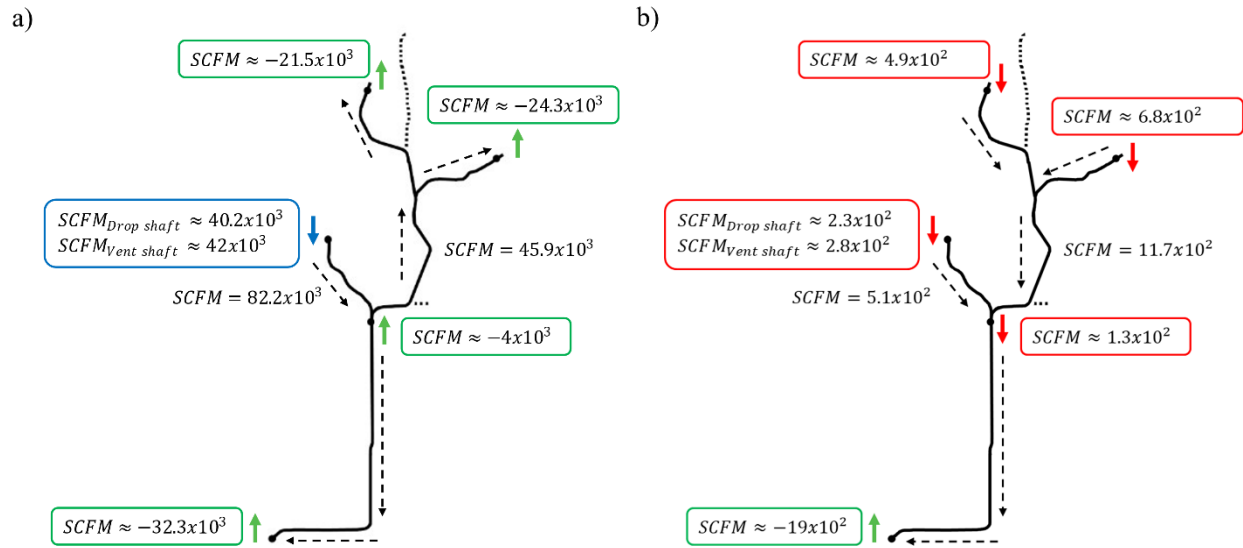


Figure 4.11. SCFM predictions for the DRTC+ECT+WRT+LPgRT alignment: a) cold conditions and b) warm conditions.

#### 4.2.4 Third Alignment Effect (DRTC+ECT+WRT+LPgRT+WRT)

The third alignment, DRTC+ECT+WRT+LPgRT+WRT, consists of the second alignment plus two more openings, FC working shaft and FC vent shaft, as shown in Figure 3.9.c (p. 59). Table 4.8 shows the mass flow, vertical velocity, temperature, and water vapor mass fraction predictions in the third alignment for the cold conditions.

Table 4.8. DRTC+ECT+WRT+LPgRT+WRT alignment cold conditions results.

Cold conditions				
Opening	Mass flow ( $kg/s$ )	Vertical velocity ( $m/s$ )	Temperature ( $^{\circ}C$ )	Mass fraction ( $kg_{H_2O}/kg_{humid\ air}$ ) ( $1 \times 10^{-4}$ )
Screen shaft	-33.790337	0.069	12.430	80.490
Utility shaft No.3	-3.588843	0.871	12.563	47.060
Eagle Creek vent shaft	18.04588	-3.216	-8.006	9.640
Eagle Creek drop shaft	17.256049	-2.917	-8.004	9.640
LP vent shaft	-22.956289	4.622	12.769	78.660
WR vent shaft	-22.323903	4.457	12.769	73.680
FC working shaft	119.303419	-1.900	-7.906	9.6400
FC retrieval shaft	-71.840558	1.080	12.772	64.830

From Table 4.8, it can be seen that the mass flow magnitude in the Eagle Creek vent shaft, the Eagle Creek drop shaft, utility shaft No.3, and screen shaft is similar to the mass flow obtained in the initial alignment in Table 4.4 (p. 88). For the two new shafts in the third alignment, the FC working shaft ingested air, and the FC retrieval shaft exhausted air from the tunnel. Moreover, the mass flow ingested into the FC working shaft was approximately three times larger than the mass flow ingested at the Eagle Creek vent and drop shafts combined. The increased mass flow rate is associated with the area of the vertical shaft opening. For example, the FC working shaft and FC retrieval shaft area are seven times larger than the combined area of the Eagle Creek vent and drop shaft openings (Table 3.1, p. 41).

Table 4.9 shows the mass flow, vertical velocity, temperature, and water vapor mass fraction predictions in the third alignment for the warm conditions. Comparing the mass flow results against the initial alignment, there is a new location, besides the screen shaft, that exhausts air during warm conditions, the FC working shaft. All other shafts ingest air into the tunnel. Table 4.9 shows that the mass flow ingested in the FC retrieval shaft is more than five times larger than the other locations due to its larger opening area. However, despite its large opening area, the mass flow exhausted in the FC working shaft was approximately six times less than the air exhausted in the screen shaft. During warm conditions, air circulation in the tunnel is driven by the direction of the clear water stream. The flow pattern results in a larger amount of air exhausted from the screen shaft than the FC working shaft.

*Table 4.9. DRTC+ECT+WRT+LPgRT+WRT alignment warm conditions results.*

Warm conditions				
Opening	Mass flow ( $kg/s$ )	Vertical velocity ( $m/s$ )	Temperature ( $^{\circ}C$ )	Mass fraction ( $kg_{H_2O}/kg_{humid\ air}$ ) ( $1 \times 10^{-4}$ )
Screen shaft	-2.654	0.006	13.283	92.190
Utility shaft No.3	0.031	-0.028	19.009	93.950
Eagle Creek vent shaft	0.114	0.040	17.472	94.000
Eagle Creek drop shaft	0.092	0.020	17.357	94.000
LP vent shaft	0.345	-0.030	21.150	94.000
WR vent shaft	0.228	-0.008	20.371	94.000
FC working shaft	-0.406	0.017	17.875	93.470
FC retrieval shaft	1.917	0.038	20.321	94.000

Finally, Figure 4.12 presents the comparison between the cold and warm conditions in the third alignment in SCFM. Figure 4.12.a shows that the air is ingested into the tunnel through the Eagle Creek location and the FC working shaft during cold conditions. The air coming through the Eagle Creek vent shaft and the Eagle Creek drop shaft circulate down towards utility shaft No.3 and screen shaft. On the other hand, air circulating from the FC working shaft goes to the FC retrieval shaft, WR vent shaft, and LP vent shaft, and to the openings of the initial alignment as shown in Figure 4.12.a.

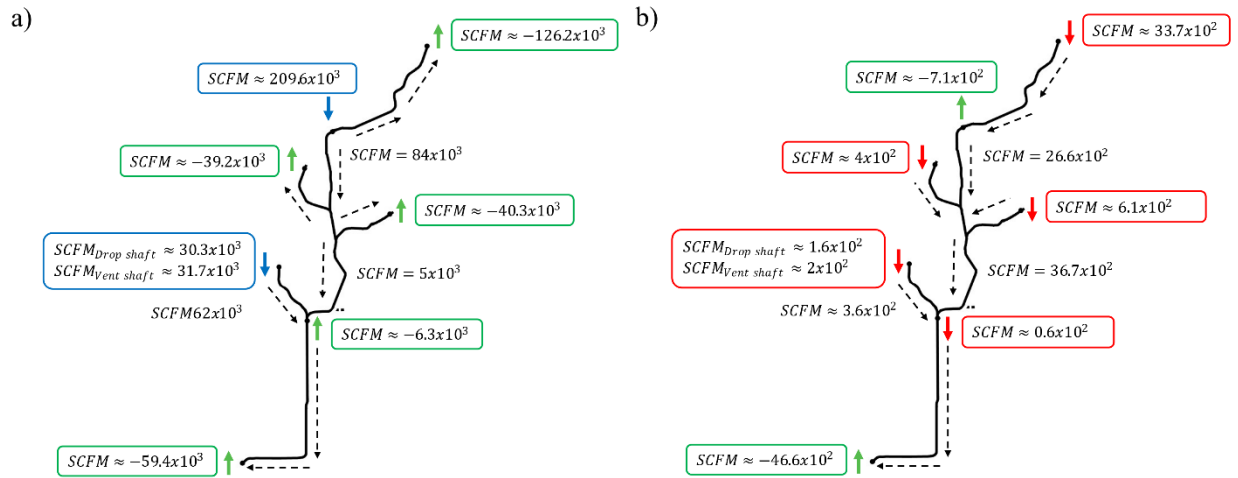


Figure 4.12. SCFM predictions for the DRTC+ECT+WRT+LPgRT+WRT alignment: a) cold conditions and b) warm conditions.

For warm conditions, the air is coming inside the tunnel through all the openings, except for the screen shaft and FC working shaft, as shown in Figure 4.12.b. Some of the air coming from the FC retrieval shaft is exhausted at the FC working shaft, and the remaining flow travels south to the screen shaft. Furthermore, the mass flow exhausted in the screen shaft increases with respect to the mass flow exhausted in the second alignment.

#### 4.2.5 Fourth Alignment Effect (DRTC+ECT+WRT+LPgRT+WRT+PRDT)

Finally, the fourth alignment, DRTC+ECT+WRT+LPgRT+WRT+PRDT, consists of the third alignment plus three more openings, PR working shaft, PR intermediate shaft, and PR retrieval shaft, as shown in Figure 3.9.c (p. 59). The fourth alignment represents the full extension of the tunnel after construction in 2025. Table 4.10 shows the mass flow, vertical

velocity, temperature, and water vapor mass fraction predictions in the fourth alignment for the cold conditions.

From Table 4.10, it can be seen that the mass flow in the Eagle Creek vent shaft and Eagle Creek drop shaft change direction, and now these locations are exhausting air during cold conditions. The mass flow in the Eagle Creek drop shaft and the Eagle Creek vent shaft is the opposite that was found in the initial, second, and third alignment. Now the shafts that ingest air into the tunnel are the PR working shaft, the PR retrieval shaft, and the FC working shaft.

The mass flow results in Table 4.10 show that the largest ingestion point is in the PR working shaft, which is the largest opening in the tunnel. The mass flow ingested at the PR working shaft is approximately 1.4 times the air ingested at the FC working shaft and approximately 2.3 times the air ingested at the PR retrieval shaft. The PR working shaft opening area is approximately 1.7 times larger than the other working, intermediate, and retrieval shaft openings (Table 3.1, p. 41).

*Table 4.10. DRTC+ECT+WRT+LPgRT+WRT+PRDT alignment cold conditions results.*

Cold conditions				
Opening	Mass flow ( $kg/s$ )	Vertical velocity ( $m/s$ )	Temperature ( $^{\circ}C$ )	Mass fraction ( $kg_{H_2O}/kg_{humid\ air}$ ) ( $1 \times 10^{-4}$ )
Screen shaft	-33.719	0.411	12.477	78.880
Utility shaft No.3	-3.503	0.847	11.877	39.170
Eagle Creek vent shaft	-16.967	3.534	12.760	65.790
Eagle Creek drop shaft	-15.940	3.244	12.694	65.860
LP vent shaft	-25.228	5.157	12.767	84.250
WR vent shaft	-24.451	4.890	12.767	75.040
FC working shaft	107.734	-1.972	-7.818	9.640
FC retrieval shaft	-71.654	1.031	12.772	67.040
PR working shaft	153.924	-1.414	-7.818	9.650
PR intermediate shaft	-136.327	1.978	12.767	63.050
PR retrieval shaft	66.340	-1.046	-6.709	9.640

Table 4.11 shows the mass flow, vertical velocity, temperature, and water vapor mass fraction predictions in the fourth alignment for warm conditions. From Table 4.11, it can be seen



that adding the PR segment did not change the mass flow trend with respect to the first, second, and third alignment. However, the amount of mass flow exhausted from the screen shaft was increased. Furthermore, Table 4.11 shows that the PR working shaft is the largest exhausting opening in the tunnel, and the PR retrieval shaft is the largest ingesting opening in the tunnel.

*Table 4.11. DRTC+ECT+WRT+LPgRT+WRT+PRDT alignment warm conditions results.*

Cold conditions				
Opening	Mass flow ( $kg/s$ )	Vertical velocity ( $m/s$ )	Temperature ( $^{\circ}C$ )	Mass fraction ( $kg_{H_2O}/kg_{humid\ air}$ ) ( $1 \times 10^{-4}$ )
Screen shaft	-3.19	0.017	13.131	92.19
Utility shaft No.3	0.026	-0.014	19.041	93.91
Eagle Creek vent shaft	0.108	0.032	17.191	94
Eagle Creek drop shaft	0.086	0.03	17.392	94
LP vent shaft	0.335	-0.032	20.987	94
WR vent shaft	0.245	-0.009	20.553	94
FC working shaft	-0.219	-0.002	17.934	93.56
FC retrieval shaft	1.844	0.036	20.221	94
PR working shaft	-4.849	0.027	15.945	92.46
PR intermediate shaft	1.667	-0.013	19.991	94
PR retrieval shaft	3.646	0.005	22.149	94

Finally, Figure 4.13 compares the cold and warm conditions in the fourth alignment in SCFM. Figure 4.13.a shows that in cold conditions, the air ingested into the tunnel through the FC working shaft, the PR working shaft, and the PR retrieval shaft, and the air is exhausted for all the other shafts. The flow pattern changes with respect to the previous alignments making the Eagle Creek shafts tunnel's exhausts during cold conditions. Figure 4.13.b shows that flow is exhausted through the FC working shaft, the PR working shaft, and the screen shaft for warm conditions. Independent of the conditions, the screen shaft exhausts flow, and the PR retrieval shaft ingest air into the tunnel.

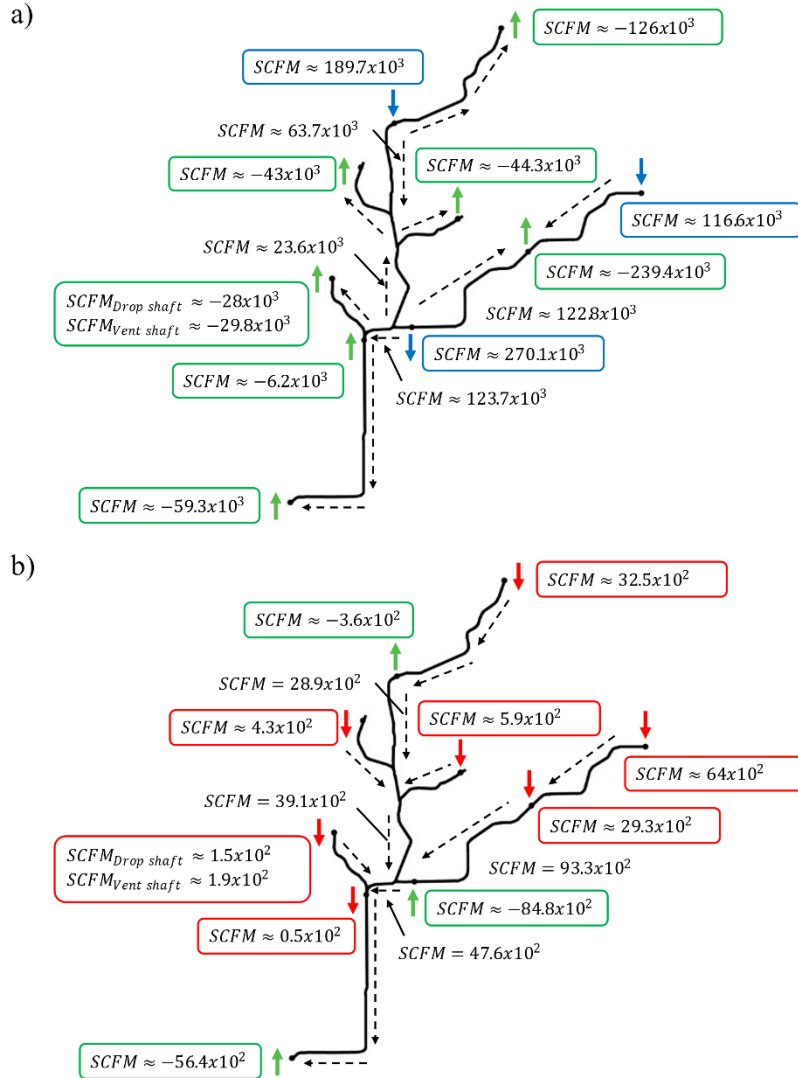


Figure 4.13. SCFM predictions for the DRTC+ECT+WRT+LPgRT+WRT+PRDT alignment: a) cold conditions and b) warm conditions.

#### 4.2.6 Discussion of Alignment Effect

From the CFD results presented in Sections 4.2.2 through 4.2.5, it was observed that the screen shaft served as an exhaust location under all conditions and for all the tunnel alignments. Furthermore, for all the alignments, the mass flow during the coldest months was one to two orders of magnitude larger than the mass flow achieved with warm conditions.

For cold conditions, the results showed that depending on the configuration, the flow patterns could change, e.g., the Eagle Creek shaft was ingesting air in the domain for the initial, second, and third alignment, but in the fourth alignment was exhausting air. The change in

pattern is due to the inclusion of a larger opening area: the PR working shaft (Table 3.1, p. 41). The larger opening creates a larger body force which drives more air into the tunnel. Nevertheless, balancing of force due to relative height is also important and must be analyzed carefully.

The results showed that the air circulates from the different tunnel openings and flows south to the nearest exhaust point for warm conditions. Depending on the pressure balance in the tunnel, the nearest exhaust point may be the screen shaft or another location, i.e., the FC working shaft and the PR working shaft. Because there is not considerable air circulation produced for the sinking effect, the circulation patterns follow the shear force created from the clear water stream.

The results in Sections 4.1 and 4.2 show that the air circulation within the DigIndy tunnel changes due to the atmospheric conditions and the tunnel alignment. Higher natural air circulation is expected in the DigIndy tunnel in colder months, coming from the largest openings and exhausting in the other tunnel openings and always in the screen shaft. During warm conditions, a more stable system is expected, resulting in lower flow circulation. The circulation during warm conditions tends to flow toward the system's lowest point, following the clear water stream and slope direction.

The analysis given in this section shows the applicability of the CFD model to identify the location where the emission of odor may be expected. Furthermore, the model can test different strategies to change the air circulation within the tunnel. One option is the inclusion of new vertical shafts or the closing of openings.

## **CHAPTER 5. SUMMARY, CONCLUSIONS, AND RECOMMENDATIONS**

### **5.1 Summary**

Natural air circulation in the DigIndy tunnel for different seasonal conditions and alignment configurations was investigated for the present work. A literature review was conducted on this topic to identify the major factors affecting the natural air circulation in sewer systems and long tunnels. The factors affecting the air circulation were: static pressure difference between openings, thermal potential pressure difference, buoyancy force due to the difference in temperature and water vapor, wind suction, and liquid drag force from the clear water stream. A physical model, which included these physical effects, was developed and implemented in a commercially available CFD software. The CFD model was used to predict the vertical velocity, temperature, and water vapor mass fraction throughout the tunnel network.

The CFD model was validated by comparing numerical predictions to experimental measurements. At the time of this study, the DigIndy tunnel was configured in its initial alignment consisting of two tunnel segments (DRTC+ECT) and four tunnel openings (Eagle Creek vent shaft, Eagle Creek drop shaft, utility shaft No.3, and screen shaft). Surface measurements were taken at the tunnel openings to calculate and apply boundary conditions for the CFD model. Furthermore, in-shaft measurements were taken at the center of the vertical shafts of the four tunnel openings to validate the CFD model. The model was validated against experimental data, segmented monthly, from May 2020 to April 2021.

After model validation, the CFD model was used to predict the natural air circulation in four different tunnel alignments, following the construction timeline. The different alignments were analyzed for two extreme conditions: a cold condition resembling the atmospheric conditions in February 2021 and a warm condition that resembled the atmospheric conditions in July 2020.

### **5.2 Conclusions**

The seasonal effect plays an important role in the natural air circulation, creating a larger air circulation in the coldest months and a stable system with lower air circulation in the warmer months. The flow in the coldest months is mainly produced for the sinking effect due to the

temperature difference between the atmospheric temperature and the tunnel wall temperature, i.e., 12.78 °C. For the fall and spring months, the sinking effect is observed by it varies depending on the temperature cycling during the day. To capture the complete phenomenology during these months, it is recommended to use a transient model that captures the storage and release of energy from the tunnel walls depending on the time of the day. In this manner, the temperature distribution in the tunnel is correctly captured.

A good agreement was observed between the CFD model and the experimental data collected from the in-shaft weather stations. Some discrepancies were noted in the winter months at the utility shaft No.3 location. The discrepancies were attributed to the non-uniform temperature distribution in the tunnel, as was studied in Section 4.2.6 (p. 97). Despite the discrepancies, the CFD model captures the sinking effect during the coldest months, predicting in close agreement the vertical velocity, temperature, and water vapor mass fraction in the Eagle Creek vent shaft, Eagle Creek drop shaft, and screen shaft. Regardless of the prediction for the coldest months in utility shaft No.3, the model is considered to capture the main force driving the air into the DigIndy tunnel.

Results show that for cold conditions, the alignment configuration plays an important in the air circulation within the tunnel, having the possibility of changing the flow direction by adding new openings. On the other hand, results from the warm condition show that the flow goes from the tunnel openings towards the screen shaft, but it can be exhausted in large diameter shafts, i.e., the FC working shaft and the PR working shaft. Regardless of the atmospheric condition, the screen shaft was an exhaust of the system.

The alignment effect study showed that the model is useful as a ventilation tool to estimate the natural air circulation in the DigIndy tunnel. The ventilation tool allows the evaluation of different mitigation strategies, including new vertical shafts or closing or opening different openings across the tunnel. Also, strategies that change microclimate conditions can be incorporated into the model by changing the boundary conditions, i.e., wind suction extractors, as shown in Figure 2.1 (p. 30).

### **5.3 Answer to Research Questions**

The following section presents the research question and the answers found during the development of this study.

**First research question:**

For developing a computational model to predict natural air circulation in CSO storage tunnels, what physical phenomena must be included in the model and what phenomena may be disregarded?

**Answer to the first research question:**

The physical phenomena required to provide accurate results in the CFD model are wind suction, minor losses in openings, the thermal potential pressure difference between openings, buoyancy forces within the tunnel system due to temperature and humidity differences, and drag force from the clear water stream. On the other hand, the static pressure could be disregarded.

**Second research question:**

What is the effect of seasonal conditions in the natural air circulation in the DigIndy tunnel?

**Answer to the second research question:**

The seasonal effect has a significant influence on air circulation within the tunnel. During the winter months (December - February), there is a temperature inversion (cold at the surface and warm in the tunnel) which causes a sinking effect at the Eagle Creek location. The sinking effect acts over the large area of the Eagle Creek drop and vent shafts and drives flow along with the grade of the tunnel towards the lowest point at the screen shaft location. During the summer months (June - August), the buoyancy effects are minimal because the direction of the thermal gradient creates a stable system (warm at the surface and cool in the tunnel). As a result, there is little-to-no air circulation within the tunnel in the warmer months. For spring (March - May) and fall (September - November), the magnitude of the sinking effect depends on the atmospheric temperature that changes during the day.

**Third research question:**

What is the effect of different alignment configurations in the natural air circulation in the DigIndy tunnel?

**Answer to the third research question:**

During cold conditions, the alignment configuration has an important role in determining the openings that exhaust air from the tunnel or ingest air in the tunnel. The larger opening showed a more significant effect in determining the direction of the flow. Larger openings account for large amounts of air that, in cold conditions, sink inside the tunnel.

During warm conditions, the alignment configuration showed no significant effect in the natural air circulation since the airflow tries to go from the different openings to the closest largest shaft and the screen shaft location. The trend is related to the direction of the clear water stream and the slope orientation that points out to the lowest location in the tunnel, which is the screen shaft.

#### **5.4 Recommendations**

The primary recommendation for future work is to improve model prediction in cold conditions by modeling heat conduction in the tunnel wall. The temperature of the tunnel wall was found to have a significant effect on the flow distribution during cold conditions, as described in Section 4.1.3 (p. 78). Conduction in the tunnel wall, surface condensation, and transient effects should be considered for model improvements.

A secondary recommendation is to obtain experimental measurements from the future alignments to extend the model validation. This additional validation will improve the model generalizability for future trade, optimization, or case studies.

A final recommendation is to implement a 1-D model in the long, straight runs of the tunnel. The 1D model would significantly reduce computational expense.

## LIST OF REFERENCES

- Abdelmeguid, A. M., & Spalding, D. B. (1979). Turbulent flow and heat transfer in pipes with buoyancy effects. *Journal of Fluid Mechanics*, 94(2), 383–400.  
<https://doi.org/10.1017/S0022112079001087>
- Ansys Inc. (2019). *Ansys Fluent* (Version 2019R3) [Computer software]. Ansys Inc.
- Ansys Inc. (2021). *Ansys Fluent, Release 2021R1, Help system, Fluent user's guide*. Ansys Inc.
- Apgar, D., & Witherspoon, J. (2009). *Collection system ventilation* (No. 04-CTS-1A). IWA Publishing. <https://www.iwapublishing.com/books/9781843392880/collection-system-ventilation>
- Buck, A. L. (1981). New equations for computing vapor pressure and enhancement factor. *Journal of Applied Meteorology and Climatology*, 20(12), 1527–1532.  
[https://doi.org/10.1175/1520-0450\(1981\)020<1527:NEFCVP>2.0.CO;2](https://doi.org/10.1175/1520-0450(1981)020<1527:NEFCVP>2.0.CO;2)
- Busby, J., Lewis, M., Reeves, H., & Lawley, R. (2009). Initial geological considerations before installing ground source heat pump systems. *Quarterly Journal of Engineering Geology and Hydrogeology*, 42(3), 295–306. <https://doi.org/10.1144/1470-9236/08-092>
- Cataño-Lopera, Y. A., Tokyay, T. E., Martin, J. E., Schmidt, A. R., Lanyon, R., Fitzpatrick, K., Scalise, C. F., & García, M. H. (2014). Modeling of a transient event in the tunnel and reservoir plan system in Chicago, Illinois. *Journal of Hydraulic Engineering*, 140(9), 05014005. [https://doi.org/10.1061/\(ASCE\)HY.1943-7900.0000888](https://doi.org/10.1061/(ASCE)HY.1943-7900.0000888)
- Çengel, Y. A., Boles, M. A., & Kanoglu, M. (2019). *Thermodynamics: An engineering approach* (9th ed.).
- Çengel, Y. A., & Cimbala, J. M. (2018). *Fluid mechanics: Fundamentals and applications: Vol. 4th ed.* McGraw-Hill Education.
- Çengel, Y. A., & Ghajar, A. J. (2015). *Heat and mass transfer: Fundamentals & applications* (5th ed.).
- Chan, S. N., Cong, J., & Lee, J. H. W. (2018). 3D Numerical modeling of geyser formation by release of entrapped air from horizontal pipe into vertical shaft. *Journal of Hydraulic Engineering*, 144(3), 04017071. [https://doi.org/10.1061/\(ASCE\)HY.1943-7900.0001416](https://doi.org/10.1061/(ASCE)HY.1943-7900.0001416)
- Citizens Energy Group [CEG]. (n.d.). *DigIndy*. Citizens Energy Group. Retrieved on April 12, 2021, from <https://www.citizensenergygroup.com/Our-Company/Our-Projects/Dig-Indy/>
- Crabtree, R. W. (1989). Sediments in sewers. *Water and Environment Journal*, 3(6), 569–578.  
<https://doi.org/10.1111/j.1747-6593.1989.tb01437.x>



- Edwini-Bonsu, S., & Steffler, P. M. (2006). Dynamics of air flow in sewer conduit headspace. *Journal of Hydraulic Engineering*, 132(8), 791–799. [https://doi.org/10.1061/\(ASCE\)0733-9429\(2006\)132:8\(791\)](https://doi.org/10.1061/(ASCE)0733-9429(2006)132:8(791))
- Feistel, R., & Wagner, W. (2007). Sublimation pressure and sublimation enthalpy of H<sub>2</sub>O ice Ih between 0 and 273.16K. *Geochimica et Cosmochimica Acta*, 71(1), 36–45. <https://doi.org/10.1016/j.gca.2006.08.034>
- Ferziger, J. H., Peric, M., & Street, R. L. (2020). *Computational methods for fluid dynamics* (4th ed.). Springer.
- Guo, C., Wang, M., Yang, L., Sun, Z., Zhang, Y., & Xu, J. (2016). A review of energy consumption and saving in extra-long tunnel operation ventilation in China. *Renewable and Sustainable Energy Reviews*, 53, 1558–1569. <https://doi.org/10.1016/j.rser.2015.09.094>
- Guo, C., Xu, J., Yang, L., Guo, X., Zhang, Y., & Wang, M. (2017). Energy-saving network ventilation technology of extra-long tunnel in climate separation zone. *Applied Sciences*, 7(5), 454. <https://doi.org/10.3390/app7050454>
- Hanova, J., & Dowlatabadi, H. (2007). Strategic GHG reduction through the use of ground source heat pump technology. *Environmental Research Letters*, 2(4), 1–8. <https://doi.org/10.1088/1748-9326/2/4/044001>
- Hirsch, C. (2009). *Numerical computation of internal and external flows* (2nd ed.). Elsevier/Butterworth-Heinemann.
- Holmes, T. R. H., Owe, M., Jeu, R. A. M. D., & Kooi, H. (2008). Estimating the soil temperature profile from a single depth observation: A simple empirical heatflow solution. *Water Resources Research*, 44(2), 1–11. <https://doi.org/10.1029/2007WR005994>
- Holt, G. J., Maynes, D., & Blotter, J. (2012). *Cavitation at Sharp Edge Multi-Hole Baffle Plates*. 6, 401–410. <https://doi.org/10.1115/IMECE2011-64203>
- Kenyon, P. (2016, May). *Indianapolis awards 28km of deep-level tunnels*. Retrieved on April 6, 2021, from <https://www.tunneltalk.com/Indianapolis-19May2016-Kiewit-Shea-JV-wins-remainder-of-DigIndy-tunnels.php>
- Kim, W. J., Managaki, S., Furumai, H., & Nakajima, F. (2009). Diurnal fluctuation of indicator microorganisms and intestinal viruses in combined sewer system. *Water Science and Technology*, 60(11), 2791–2801. <https://doi.org/10.2166/wst.2009.732>
- Kusuda, T., & Achenbach, P. R. (1965). *Earth temperature and thermal diffusivity at selected stations in the united states* (OCD-0S-62-44). National Bureau of Standards Building Research Division. <https://apps.dtic.mil/sti/citations/AD0472916>

- Liang, Z., Sun, J., Chau, H. K., Leong, E. I.-M., Wu, D., Chen, G., & Jiang, F. (2019). Experimental and modelling evaluations of sulfide formation in a mega-sized deep tunnel sewer system and implications for sewer management. *Environment International*, 131, 105011. <https://doi.org/10.1016/j.envint.2019.105011>
- Liu, X., Xiao, Y., Inthavong, K., & Tu, J. (2014). A fast and simple numerical model for a deeply buried underground tunnel in heating and cooling applications. *Applied Thermal Engineering*, 62(2), 545–552. <https://doi.org/10.1016/j.applthermaleng.2013.10.017>
- Lowe, S. (2016). Sewer ventilation: Factors affecting airflow and modeling approaches. *Journal of Water Management Modeling C395*, 24, 1–5. <https://doi.org/10.14796/JWMM.C395>
- Lowe, S. (2017). Sewer ventilation modeling. *Journal of Water Management Modeling C415*, 25, 1–8. <https://doi.org/10.14796/JWMM.C415>
- Madsen, H. I., Hvitved-Jacobsen, T., & Vollertsen, J. (2006). Gas phase transport in gravity sewers: A methodology for determination of horizontal gas transport and ventilation. *Water Environment Research*, 78(11), 2203–2209.
- Malavasi, S., Messa, G., Fratino, U., & Pagano, A. (2012). On the pressure losses through perforated plates. *Flow Measurement and Instrumentation*, 28, 57–66. <https://doi.org/10.1016/j.flowmeasinst.2012.07.006>
- Matias, N., Matos, R. V., Ferreira, F., Vollertsen, J., & Matos, J. S. (2017). Release of hydrogen sulfide in a sewer system under intermittent flow conditions: The Ericeira case study, in Portugal. *Water Science and Technology*, 75(7), 1702–1711. <https://doi.org/10.2166/wst.2017.040>
- Moffat, R. J. (1988). Describing the uncertainties in experimental results. *Experimental Thermal and Fluid Science*, 1(1), 3–17. [https://doi.org/10.1016/0894-1777\(88\)90043-X](https://doi.org/10.1016/0894-1777(88)90043-X)
- Montgomery, R. B. (1947). Viscosity and thermal conductivity of air and diffusivity of water vapor in air. *Journal of the Atmospheric Sciences*, 4(6), 193–196. [https://doi.org/10.1175/1520-0469\(1947\)004<0193:VATCOA>2.0.CO;2](https://doi.org/10.1175/1520-0469(1947)004<0193:VATCOA>2.0.CO;2)
- Murali, M. K., Hipsey, M. R., Ghadouani, A., & Yuan, Z. (2020). SewerSedFoam: A model for free surface flow, sediment transport, and deposited bed morphology in sewers. *Water*, 12(1), 270. <https://doi.org/10.3390/w12010270>
- National Academy of Engineering. (n.d.). *14 Grand Challenges for Engineering in the 21st Century*. NAE Grand Challenges for Engineering. Retrieved on April 12, 2021, from <http://www.engineeringchallenges.org/challenges.aspx>
- National Weather Service. (2021). *Indianapolis Monthly Summaries 1996-Present*. Central Indiana Local Climate Info. Retrieved on July 8, 2021, from <https://www.weather.gov/media/ind/julf62020.pdf>

- Olson, D., Rajagopalan, S., & Corsi, R. L. (1997). Ventilation of industrial process drains: Mechanisms and effects on VOC emissions. *Journal of Environmental Engineering*, 123(9), 939–947. [https://doi.org/10.1061/\(ASCE\)0733-9372\(1997\)123:9\(939\)](https://doi.org/10.1061/(ASCE)0733-9372(1997)123:9(939))
- Pan, G., Wang, B., Guo, S., Zhang, W., & Edwini-Bonsu, S. (2020). Statistical analysis of sewer odour based on 10-year complaint data. *Water Science and Technology*, 81(6), 1221–1230. <https://doi.org/10.2166/wst.2020.217>
- Parker, W. J., & Ryan, H. (2001). A tracer study of headspace ventilation in a collector sewer. *Journal of the Air & Waste Management Association*, 51(4), 582–592. <https://doi.org/10.1080/10473289.2001.10464290>
- Pescod, M. B., & Price, A. C. (1982). Major factors in sewer ventilation. *Journal (Water Pollution Control Federation)*, 54(4), 385–397.
- Qian, Y. (2018). *Numerical study on air movement in sewer systems* [Doctoral dissertation, University of Alberta]. <https://doi.org/10.7939/R38C9RK9M>
- Qian, Y., Zhu, D. Z., Zhang, W., Rajaratnam, N., Edwini-Bonsu, S., & Steffler, P. (2017). Air movement induced by water flow with a hydraulic jump in changing slope pipes. *Journal of Hydraulic Engineering*, 143(4), 04016092. [https://doi.org/10.1061/\(ASCE\)HY.1943-7900.0001252](https://doi.org/10.1061/(ASCE)HY.1943-7900.0001252)
- Rosenberg, N. J., Blad, B. L., & Verma, S. B. (1983). *Microclimate: The biological environment* (2nd ed.). J. Wiley.
- Rothfuss, N. E., Marsh, A., Rovelli, G., Petters, M. D., & Reid, J. P. (2018). Condensation kinetics of water on amorphous aerosol particles. *The Journal of Physical Chemistry Letters*, 9(13), 3708–3713. <https://doi.org/10.1021/acs.jpclett.8b01365>
- Tian, R., Wei, M., Dai, X., Song, P., & Shi, L. (2019). Buoyancy effect on the mixed convection flow and heat transfer of supercritical R134a in heated horizontal tubes. *International Journal of Heat and Mass Transfer*, 144, 1–13. <https://doi.org/10.1016/j.ijheatmasstransfer.2019.118607>
- United States Environmental Protection Agency [USEPA]. (1999). *Combined sewer overflow management fact sheet: Sewer separation* (EPA 832-F-99-041). Office of Water. <https://www3.epa.gov/npdes/pubs/sepa.pdf>
- United States Environmental Protection Agency [USEPA]. (2002). *Collection systems technology fact sheet. Sewers, conventional gravity* (EPA 832-F-02-007). Office of Water. <https://nepis.epa.gov/Exe/ZyPDF.cgi/P10053D9.PDF?Dockey=P10053D9.PDF>
- United States Environmental Protection Agency [USEPA]. (2004). *Report to Congress on impacts and control of combined sewer overflows and sanitary sewer overflows* (EPA 833-R-04-001). Office of Water. [https://www.epa.gov/sites/production/files/2015-10/documents/csosortc2004\\_full.pdf](https://www.epa.gov/sites/production/files/2015-10/documents/csosortc2004_full.pdf)

- United States Environmental Protection Agency [USEPA]. (2020a, August). *Sanitary sewer overflows (SSOs)*. National Pollutant Discharge Elimination System (NPDES). Retrieved on April 15, 2021, from <https://www.epa.gov/npdes/sanitary-sewer-overflows-ssos>
- United States Environmental Protection Agency [USEPA]. (2020b, September). *Summary of the Clean Water Act*. Laws and Regulations. Retrieved on April 15, 2021, from <https://www.epa.gov/laws-regulations/summary-clean-water-act>
- Van Wijk, W. R., & Derksen, W. J. (1966). Thermal properties of a soil near the surface. *Agricultural Meteorology*, 3(5), 333–342. [https://doi.org/10.1016/0002-1571\(66\)90015-X](https://doi.org/10.1016/0002-1571(66)90015-X)
- Vyskocil, L., Schmid, J., & Macek, J. (2014). CFD simulation of air–steam flow with condensation. *Nuclear Engineering and Design*, 279, 147–157. <https://doi.org/10.1016/j.nucengdes.2014.02.014>
- Wang, Y. C., Nobi, N., Nguyen, T., & Vorreiter, L. (2012). A dynamic ventilation model for gravity sewer networks. *Water Science and Technology*, 65(1), 60–68. <https://doi.org/10.2166/wst.2011.771>
- Ward, M., Hamer, G., McDonald, A., Witherspoon, J., Loh, E., & Parker, W. (2011). A sewer ventilation model applying conservation of momentum. *Water Science and Technology*, 64(6), 1374–1382. <https://doi.org/10.2166/wst.2011.481>
- White, F. M. (2017). *Fluid mechanics* (8th ed. in SI units). Mc Graw Hill Education.
- Zhang, Z., Zhang, H., Tan, Y., & Yang, H. (2018). Natural wind utilization in the vertical shaft of a super-long highway tunnel and its energy saving effect. *Building and Environment*, 145, 140–152. <https://doi.org/10.1016/j.buildenv.2018.08.062>

## APPENDIX A – INSTRUMENTS RESOLUTION, ACCURACY, AND UNCERTAINTY

*Table A.1. ATMOS 41 resolution, accuracy, and fixed uncertainty.*

Measure	Units	Resolution	Accuracy	Fixed uncertainty screen shaft*	Fixed uncertainty utility shaft No.3*	Fixed uncertainty Eagle Creek*
Air temperature	°C	0.1	± 0.6	± 0.2	± 0.2	± 0.1
Barometric pressure	kPa	0.01	± 0.1	± 0.02	± 0.03	± 0.05
Precipitation	mm/h	0.017	± 5%	**	**	**
Vapor pressure	kPa	0.01	***	***	***	***
Wind speed	m/s	0.01	0.3 or greater than 3%	± 0.01	± 0.01	± 0.01

Note. The accuracy is assumed as  $2\sigma$ , which represents a confidence interval of 95%. The value  $2\sigma$  is used for the random error part of the zeroth-order error uncertainty analysis detailed by Moffat (1988). \* Calibration values from the manufacturer. \*\* Not reported by the manufacturer. \*\*\* Values are dependent on the temperature and vapor pressure according to manufactured specifications.

*Table A.2. ATMOS 22 resolution and accuracy.*

Measure	Units	Resolution	Accuracy
Air velocity	m/s	0.01	0.3 or greater than 3%

Note. The accuracy is assumed as  $2\sigma$ , which represents a confidence interval of 95%. The value  $2\sigma$  is used for the random error part of the zeroth-order error uncertainty analysis detailed by Moffat (1988).

*Table A.3. ATMOS 14 resolution and accuracy.*

Measure	Units	Resolution	Accuracy
Air temperature	°C	0.1	± 0.5
Vapor pressure	kPa	0.001	*

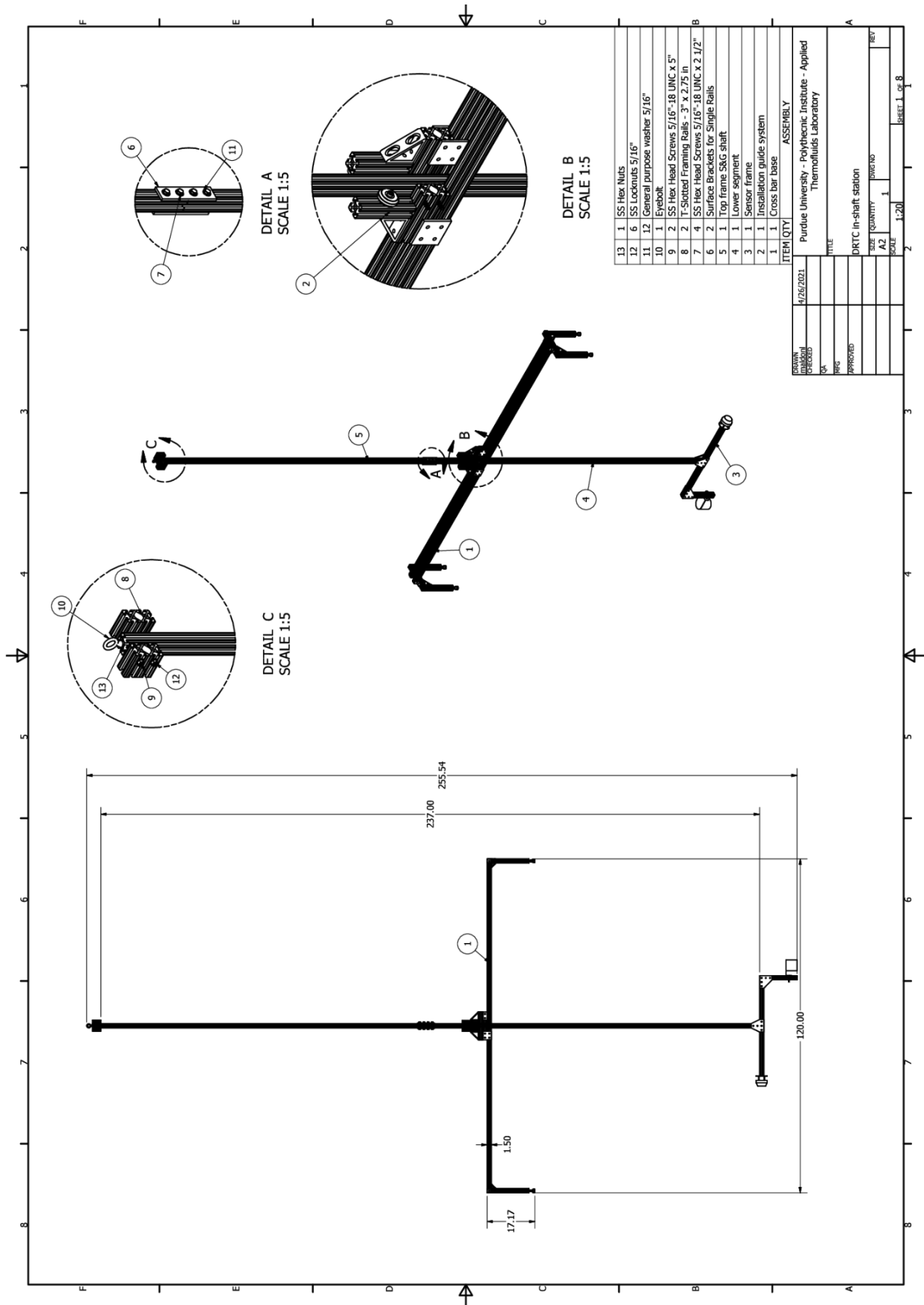
Note. The accuracy is assumed as  $2\sigma$ , which represents a confidence interval of 95%. The value  $2\sigma$  is used for the random error part of the zeroth-order error uncertainty analysis detailed by Moffat (1988). \* Values are dependent on the temperature and vapor pressure according to manufactured specifications.

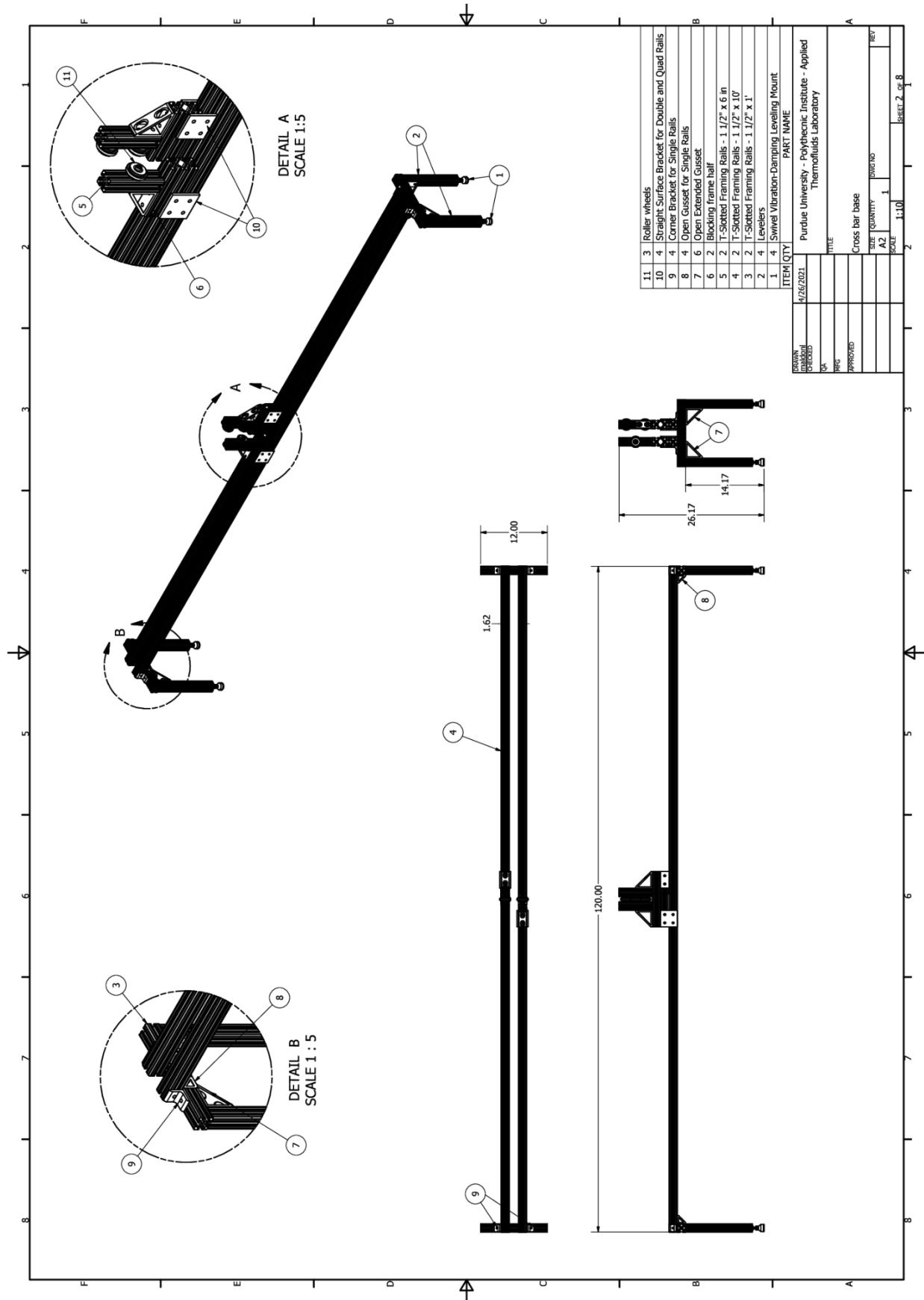
## **APPENDIX B – TECHNICAL DRAWING OF 8020 ALUMINUM STRUCTURES**

The following appendix contains the drawing of the aluminum structures used for each location in the following order:

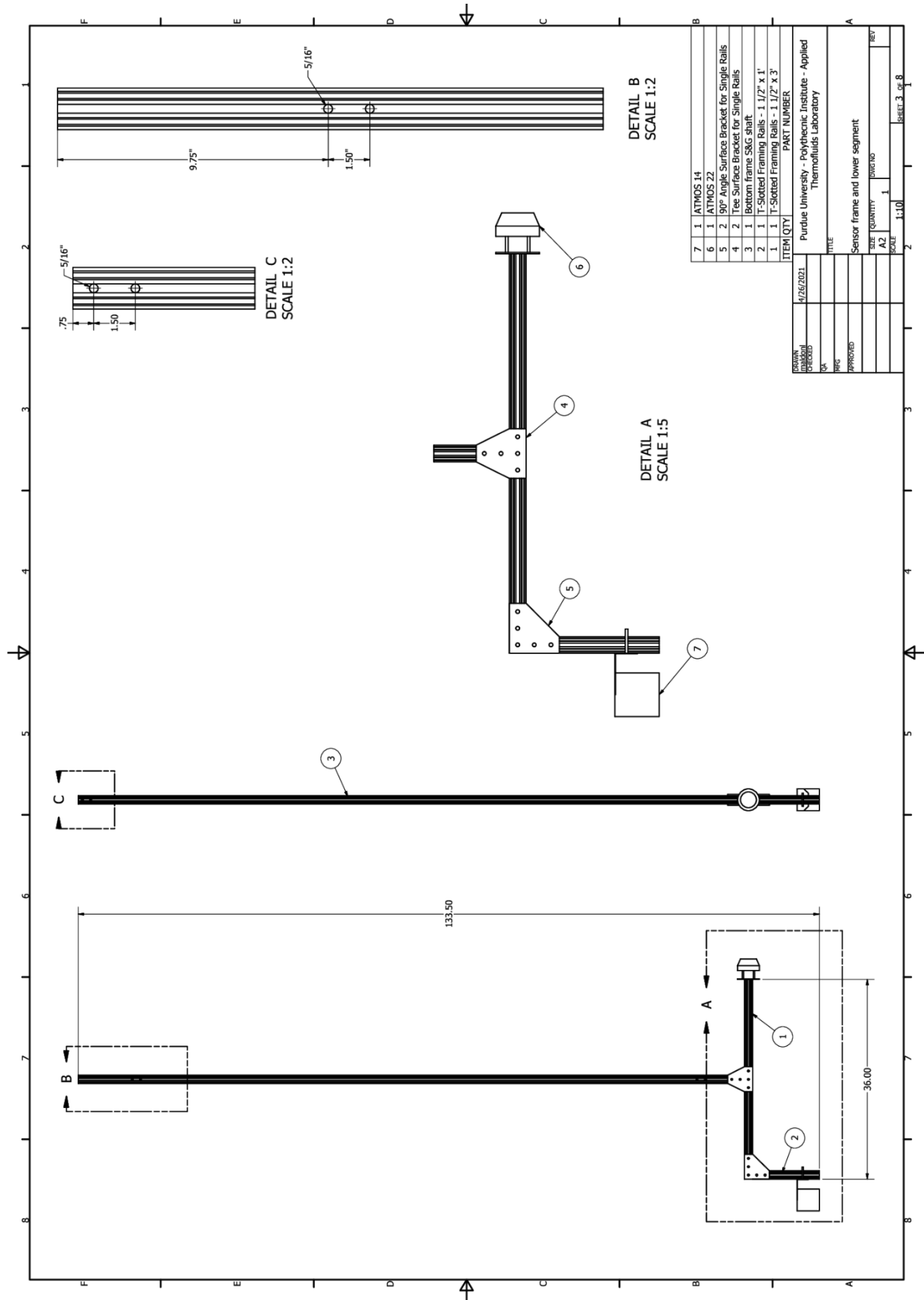
- Screen shaft mounting system drawings.
- Utility shaft No.3 mounting system drawings.
- Eagle Creek vent shaft and drop shaft mounting system drawings.

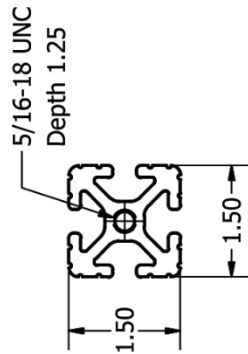
*Note.* The drawings have units of inches.





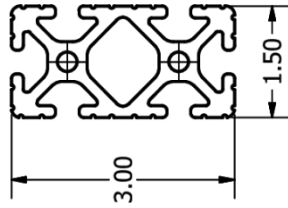
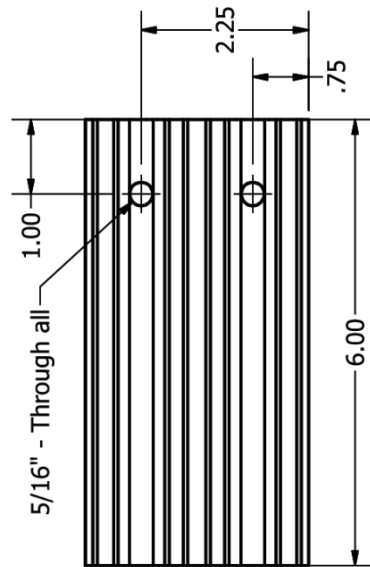






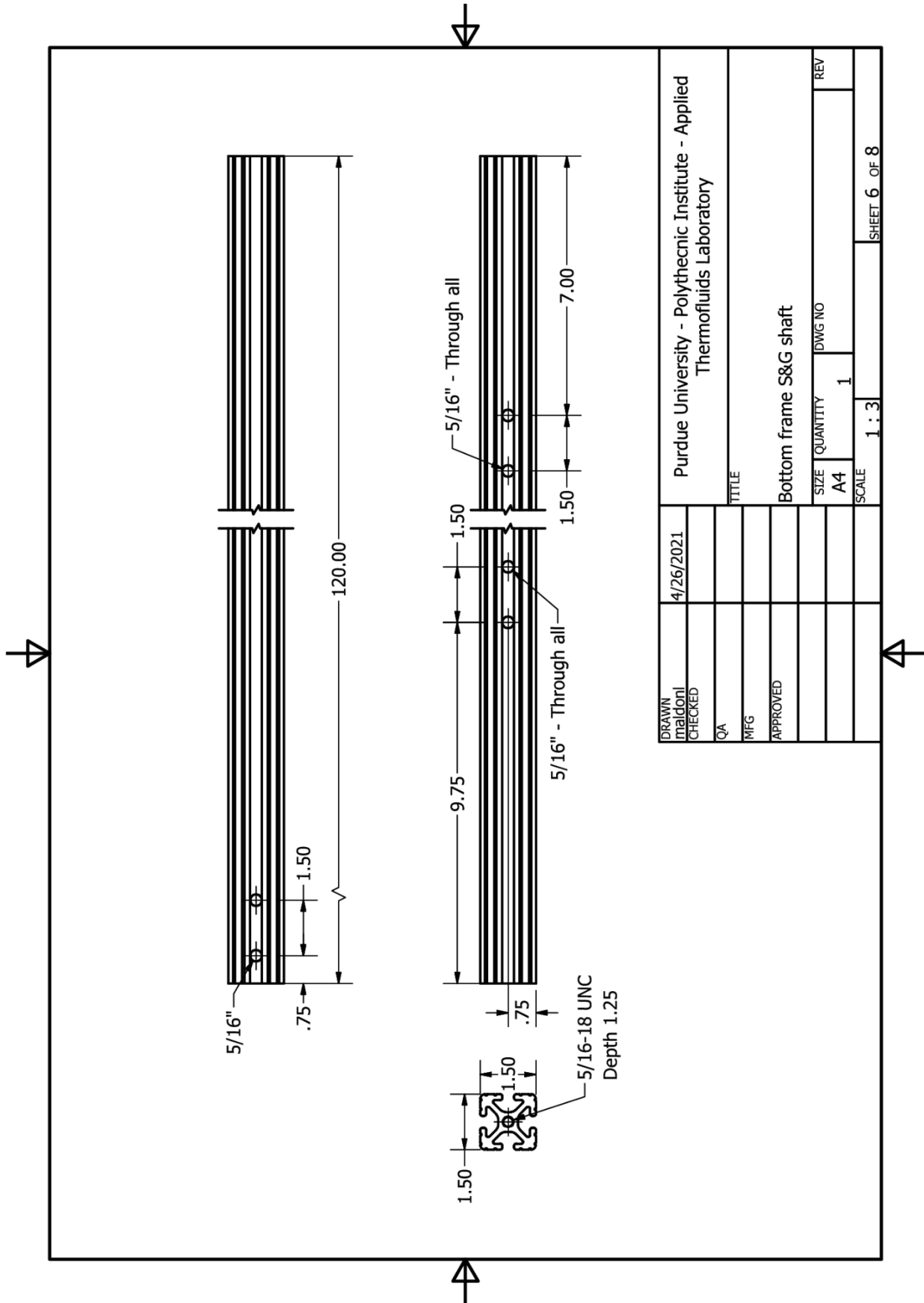
DRAWN maldonl	4/26/2021	Purdue University - Polytechnic Institute - Applied Thermofluids Laboratory			
CHECKED		TITLE			
QA		Levelers			
MFG					
APPROVED					
		SIZE	QUANTITY	DWG NO	REV
		A4	4		
		SCALE	1 : 2	SHEET 4 OF 8	



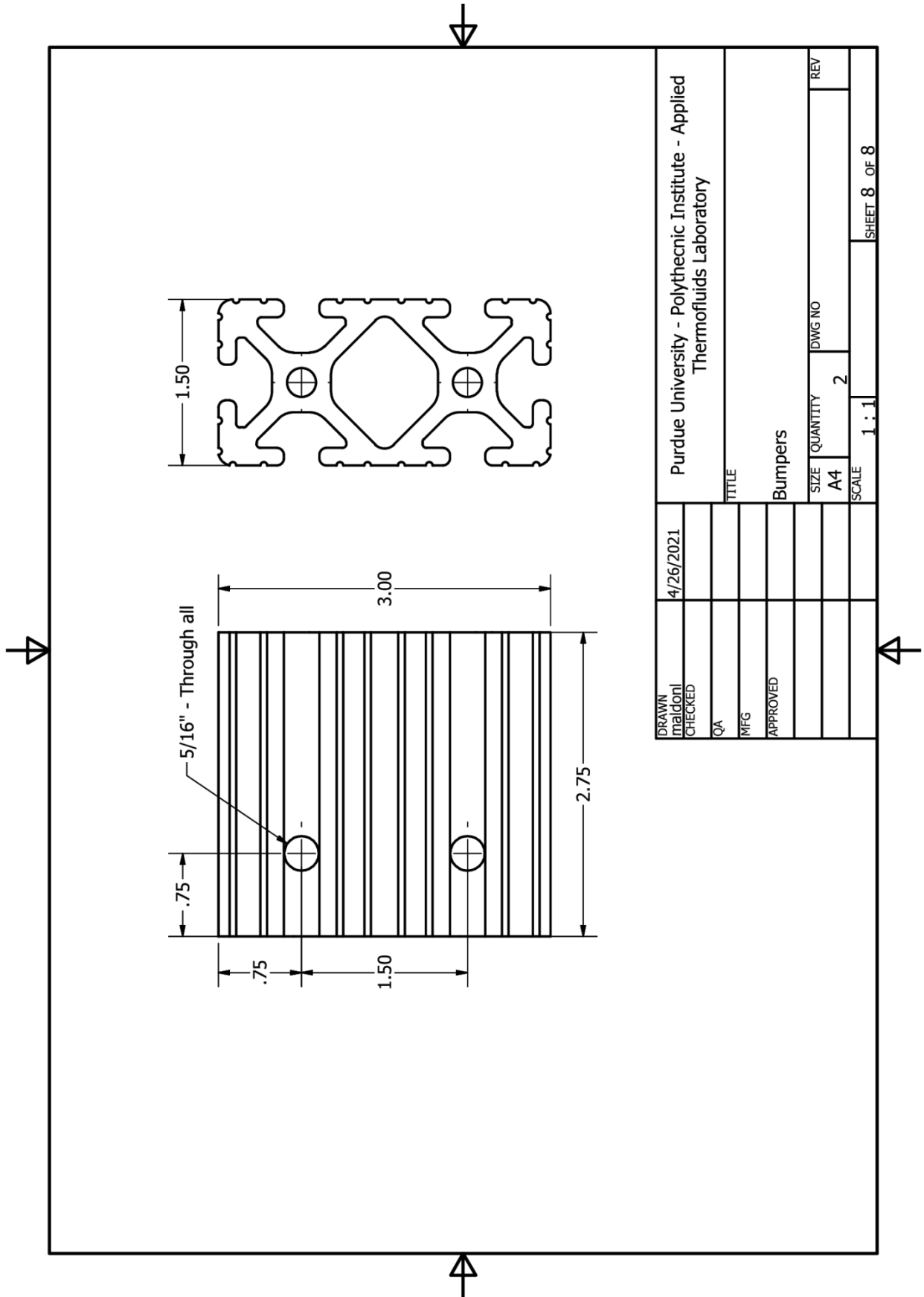


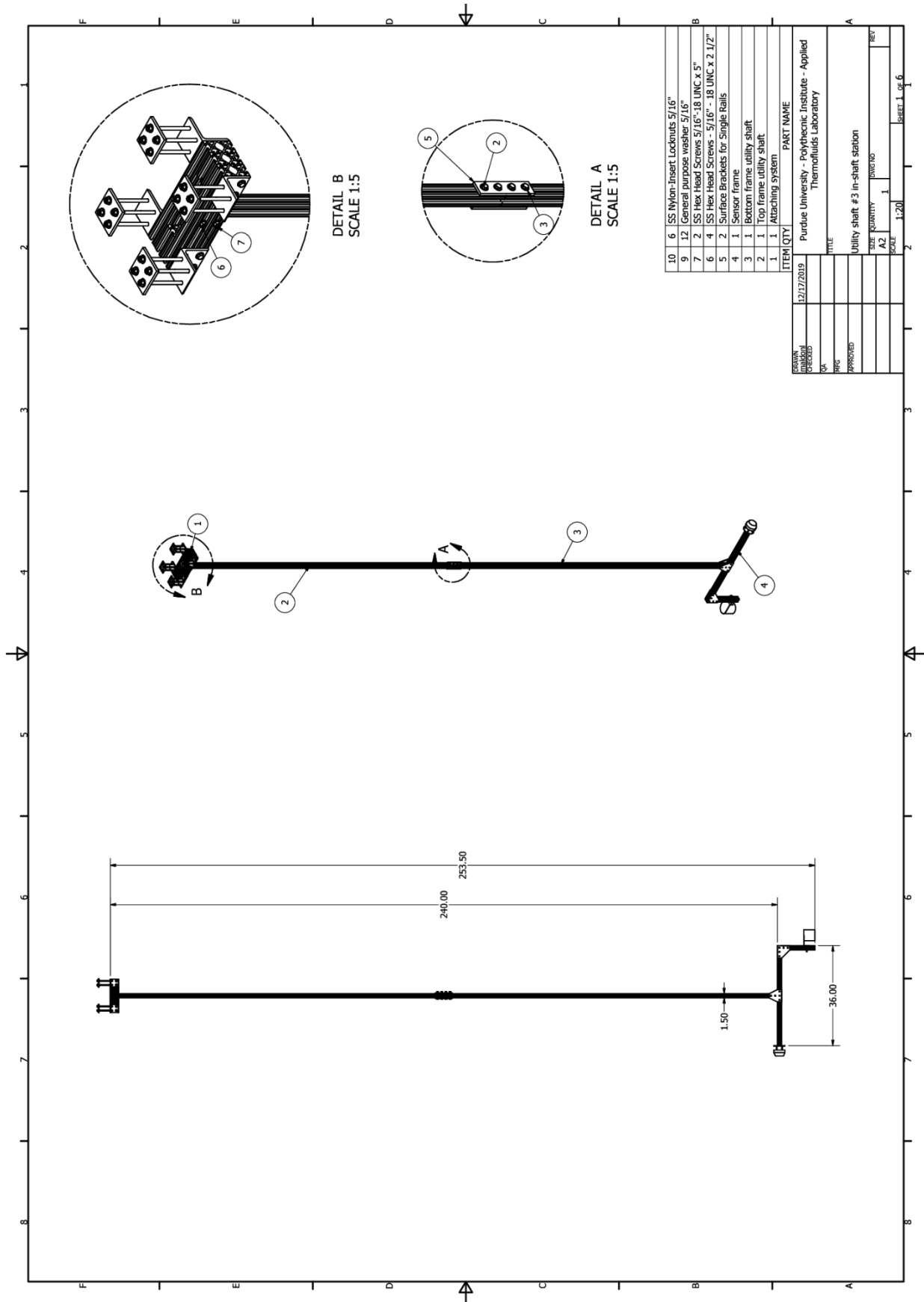
DRAWN maldonl	4/26/2021	Purdue University - Polytechnic Institute - Applied Thermofluids Laboratory	
CHECKED		TITLE	
QA		Blocking frame half	
MFG		SIZE QUANTITY DWG NO	
APPROVED		A4 2	
		REV	
		SCALE 1 : 2	
		SHEET 5 OF 8	









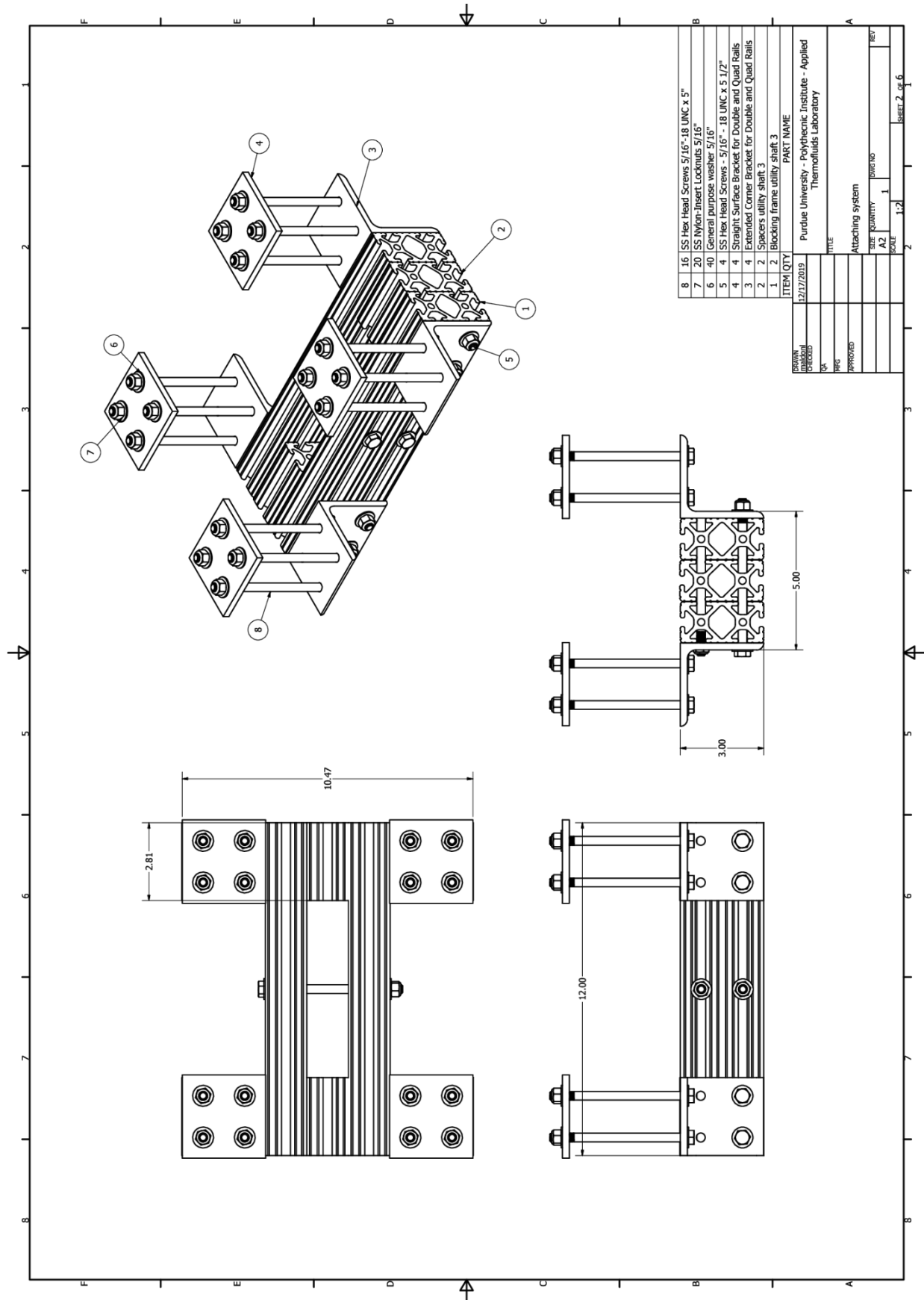


DETAIL B  
SCALE 1:5

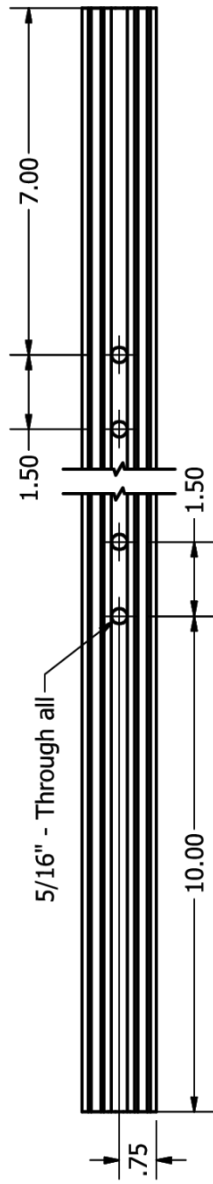
DETAIL A  
SCALE 1:5

10	6	SS Nylon-Insert Locknuts 5/16"
9	12	General purpose washer 5/16"
7	2	SS Hex Head Screws 5/16"-18 UNC x 5"
6	4	SS Hex Head Screws - 5/16" - 18 UNC x 2 1/2"
5	2	Surface Brackets for Single Rails
4	1	Sensor frame
3	1	Bottom frame utility shaft
2	1	Top frame utility shaft
1	1	Attaching system

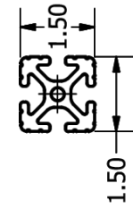
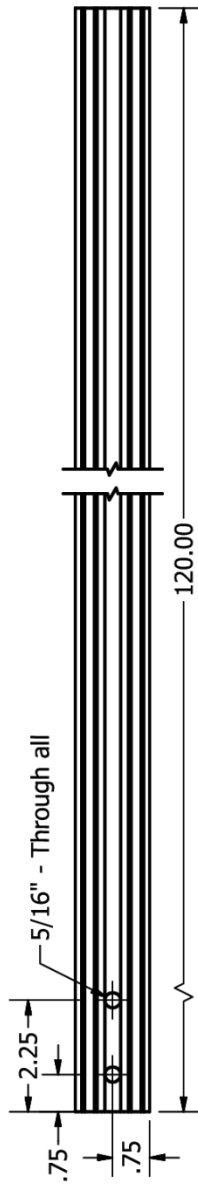
DATE	12/17/2019	PART NAME	Purdue University - Polytechnic Institute - Applied Thermofluids Laboratory
DESIGNED BY		TITLE	Utility shaft # 3 in-shaft station
APPROVED BY		DATE	
		SCALE	1:20
		QUANTITY	1
		REVISIONS	
		REV	





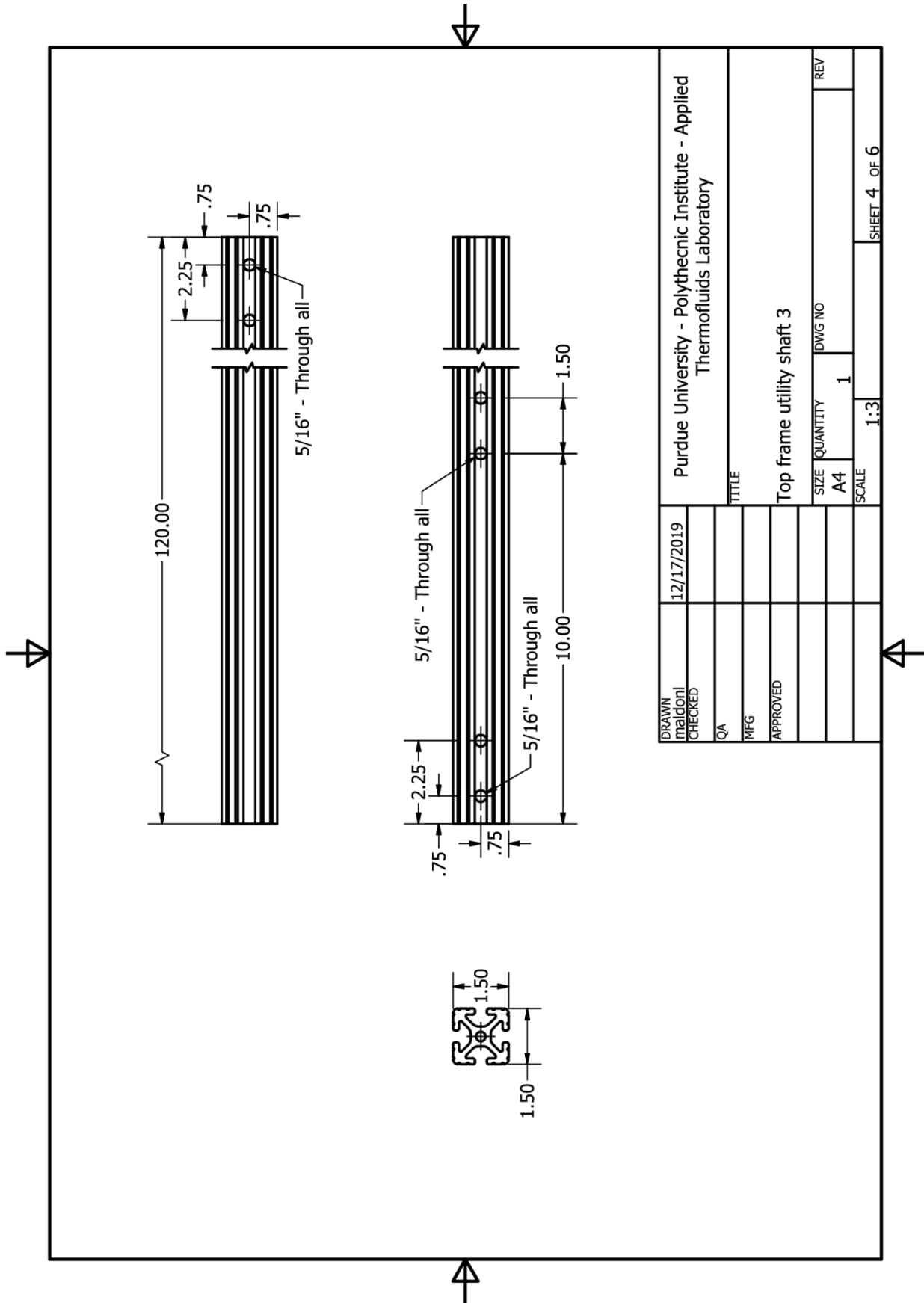


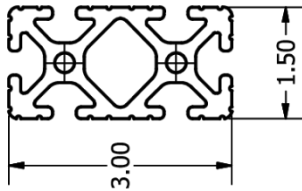
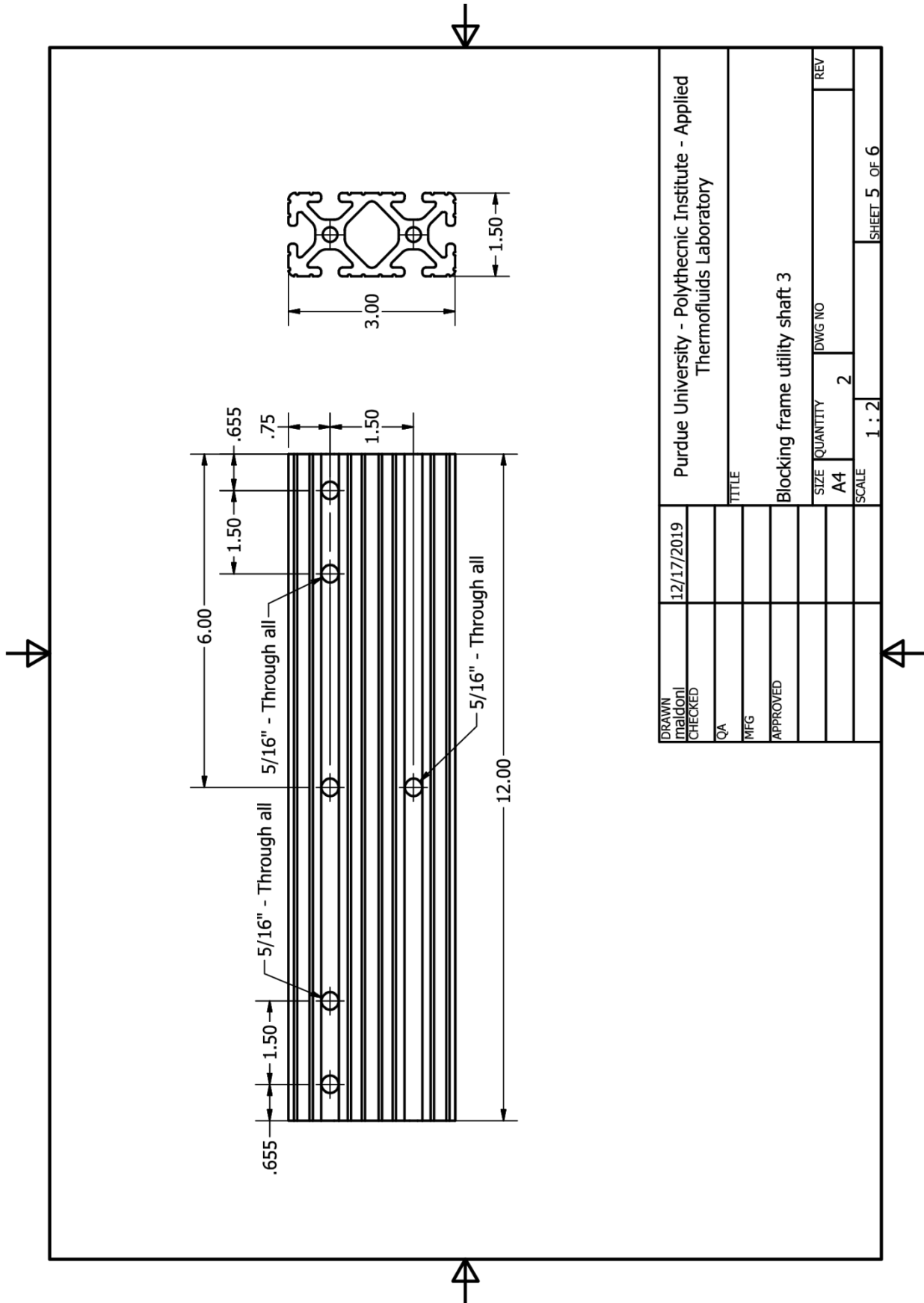
5/16" - Through all



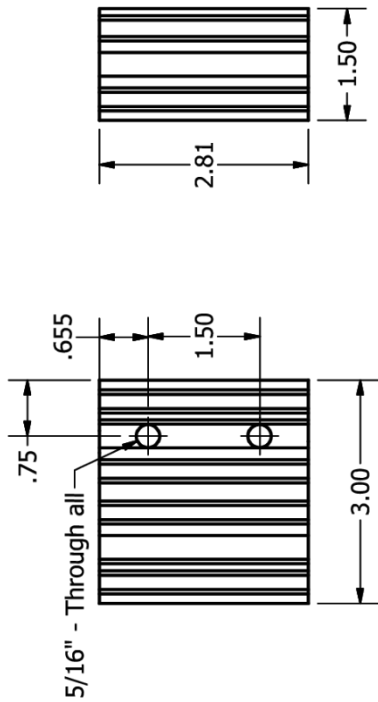
DRAWN maldonl	12/17/2019	Purdue University - Polytechnic Institute - Applied Thermofluids Laboratory	
CHECKED		TITLE	
QA		Bottom frame utility shaft 3	
MFG		SIZE QUANTITY DWG NO REV	
APPROVED		A4 1	
		SCALE 1:3	
		SHEET 3 OF 6	





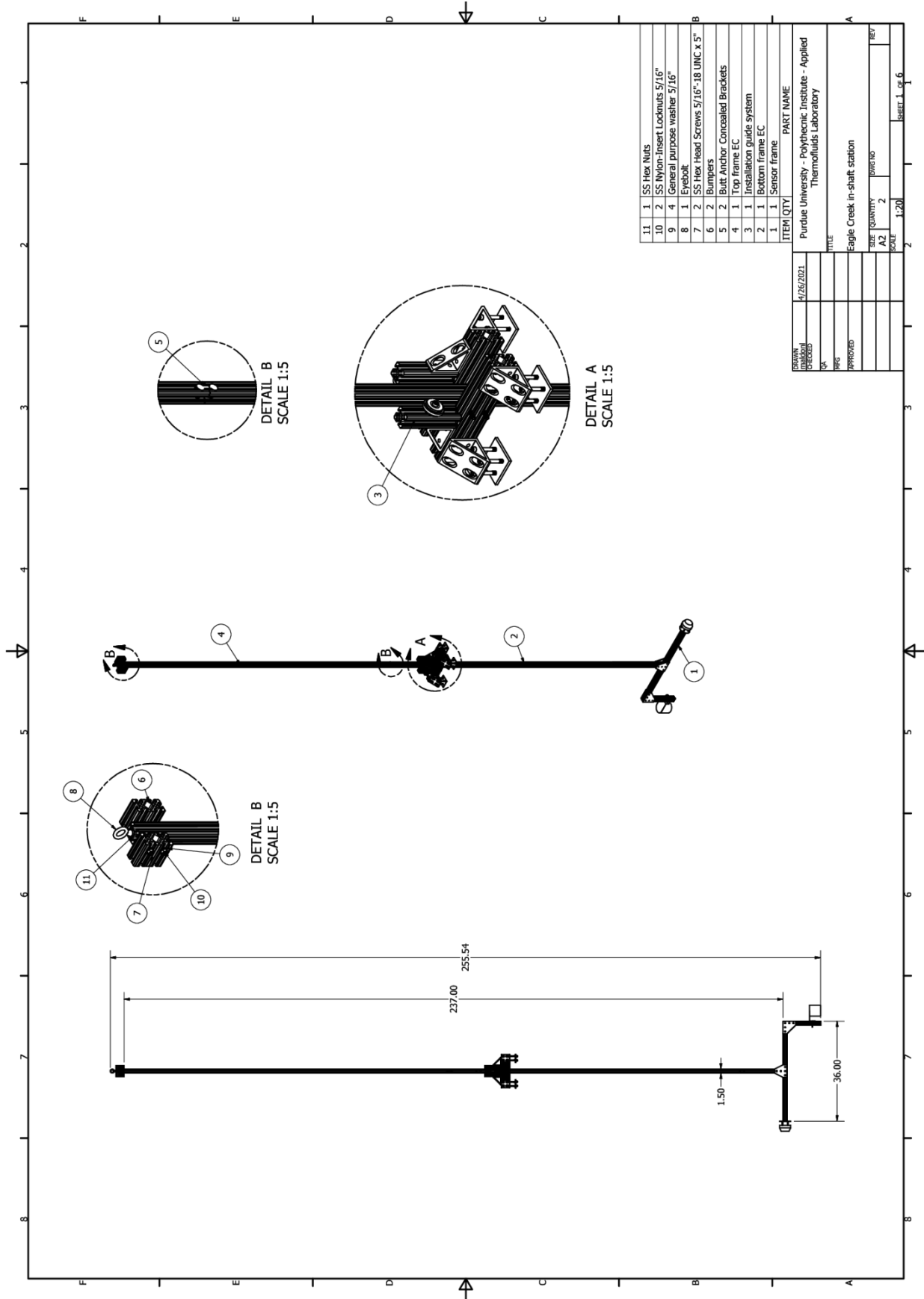


DRAWN maldonl	12/17/2019	Purdue University - Polytechnic Institute - Applied Thermofluids Laboratory			
CHECKED		TITLE			
QA		Blocking frame utility shaft 3			
MFG		SIZE QUANTITY DWG NO REV			
APPROVED		A4 2			
		SCALE 1 : 2			
		SHEET 5 OF 6			



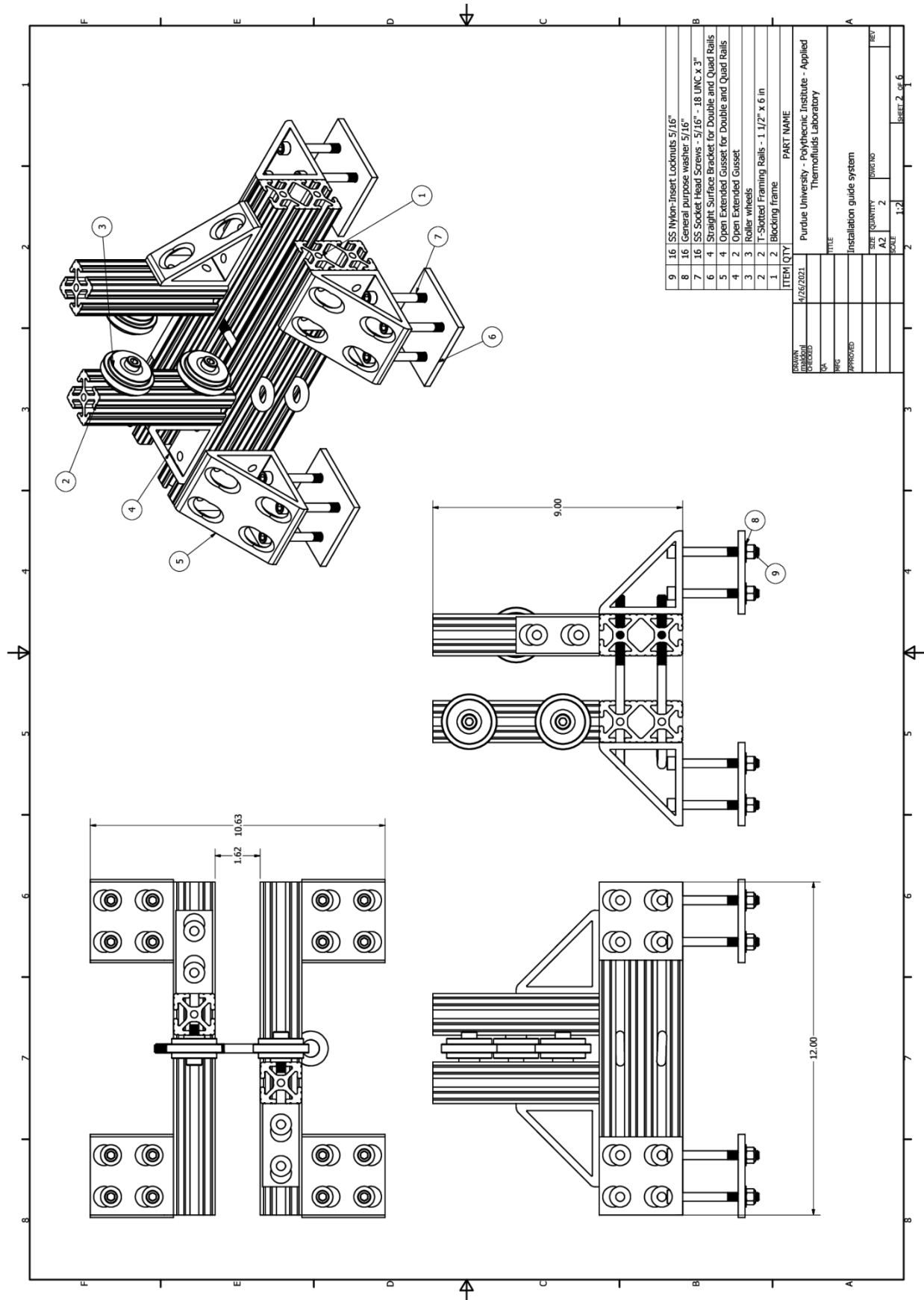
DRAWN maldonl	12/17/2019	Purdue University - Polytechnic Institute - Applied Thermofluids Laboratory			
CHECKED		TITLE			
QA		Spacers utility shaft 3			
MFG		SIZE QUANTITY DWG NO REV			
APPROVED		A4 2			
		SCALE 1 : 2			
		SHEET 6 OF 6			

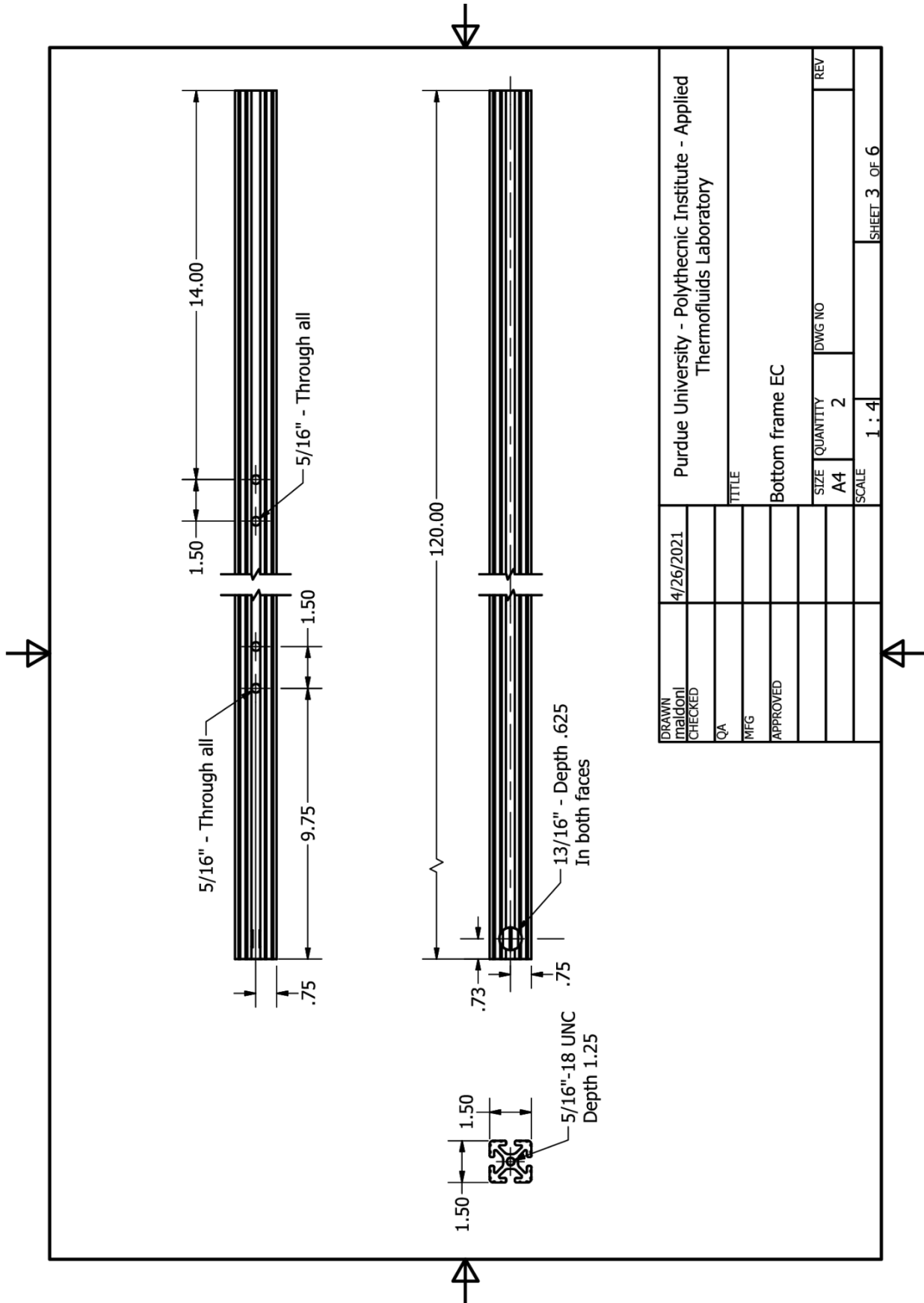


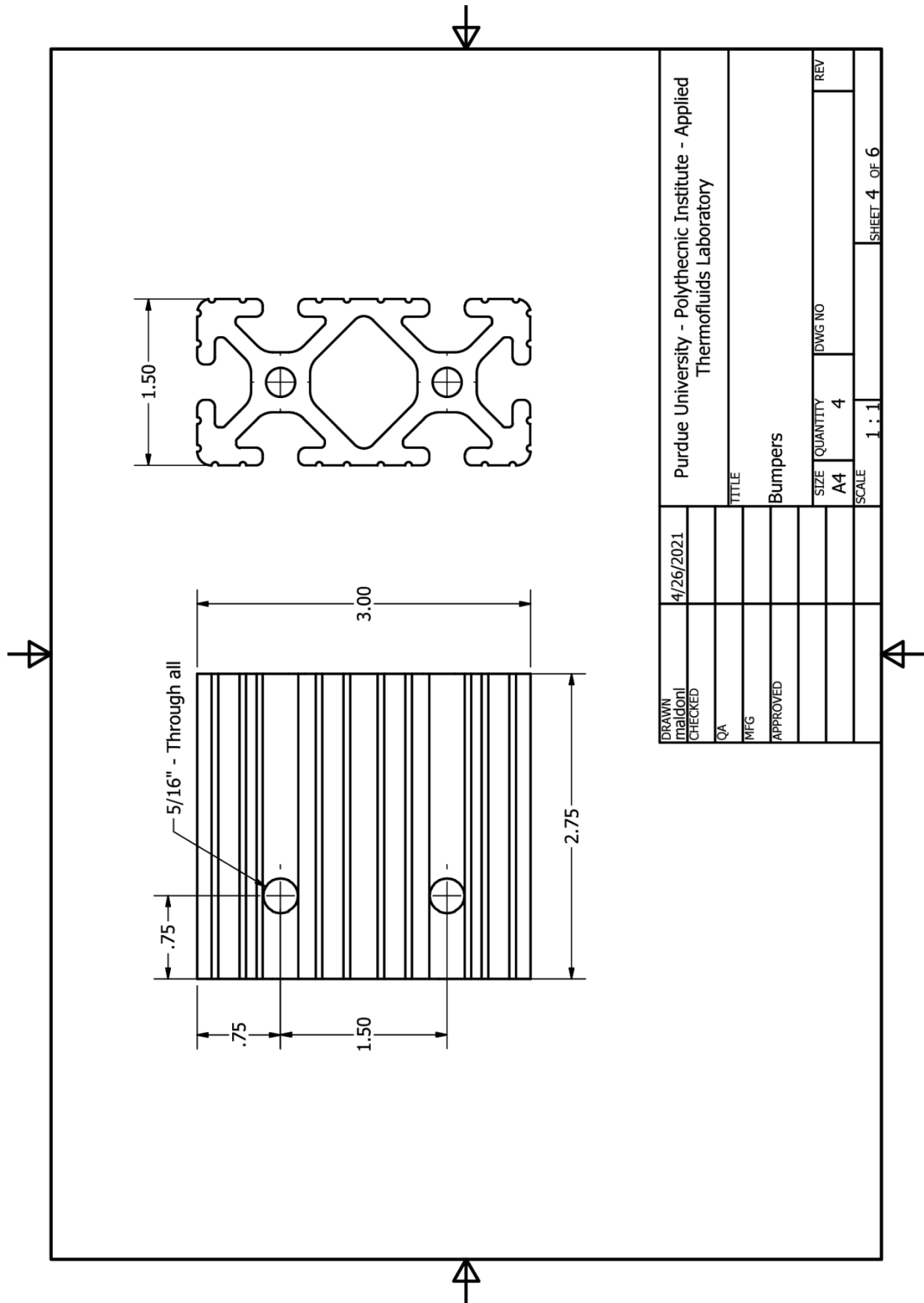


ITEM	QTY	PART NAME
1.1	1	SS Hex Nuts
1.0	2	SS Nylon-Insert Locknuts 5/16"
9	4	General purpose washer 5/16"
8	1	Eyebolt
7	2	SS Hex Head Screws 5/16"-18 UNC x 5"
6	2	Bumpers
5	2	Butt Anchor Concealed Brackets
4	1	Top frame EC
3	1	Installation guide system
2	1	Bottom frame EC
1	1	Sensor frame

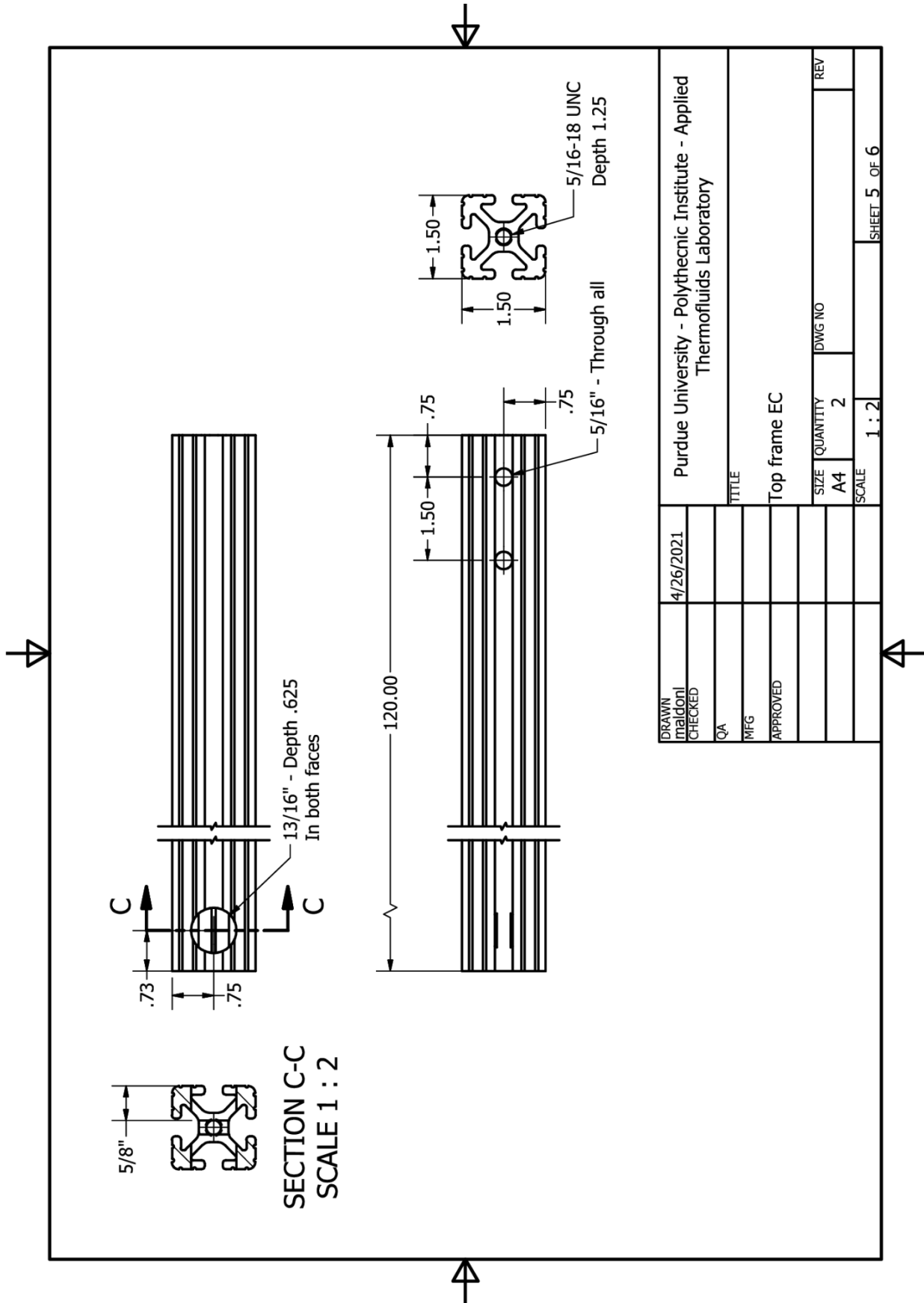
DATE	4/25/2021
DESIGNED BY	
CHECKED BY	
APPROVED BY	
TITLE	Purdue University - Polytechnic Institute - Applied Thermofluids Laboratory
PROJECT	Eagle Creek in-shaft station
DATE	
QUANTITY	2
SCALE	1:20
SHEET	1 of 6

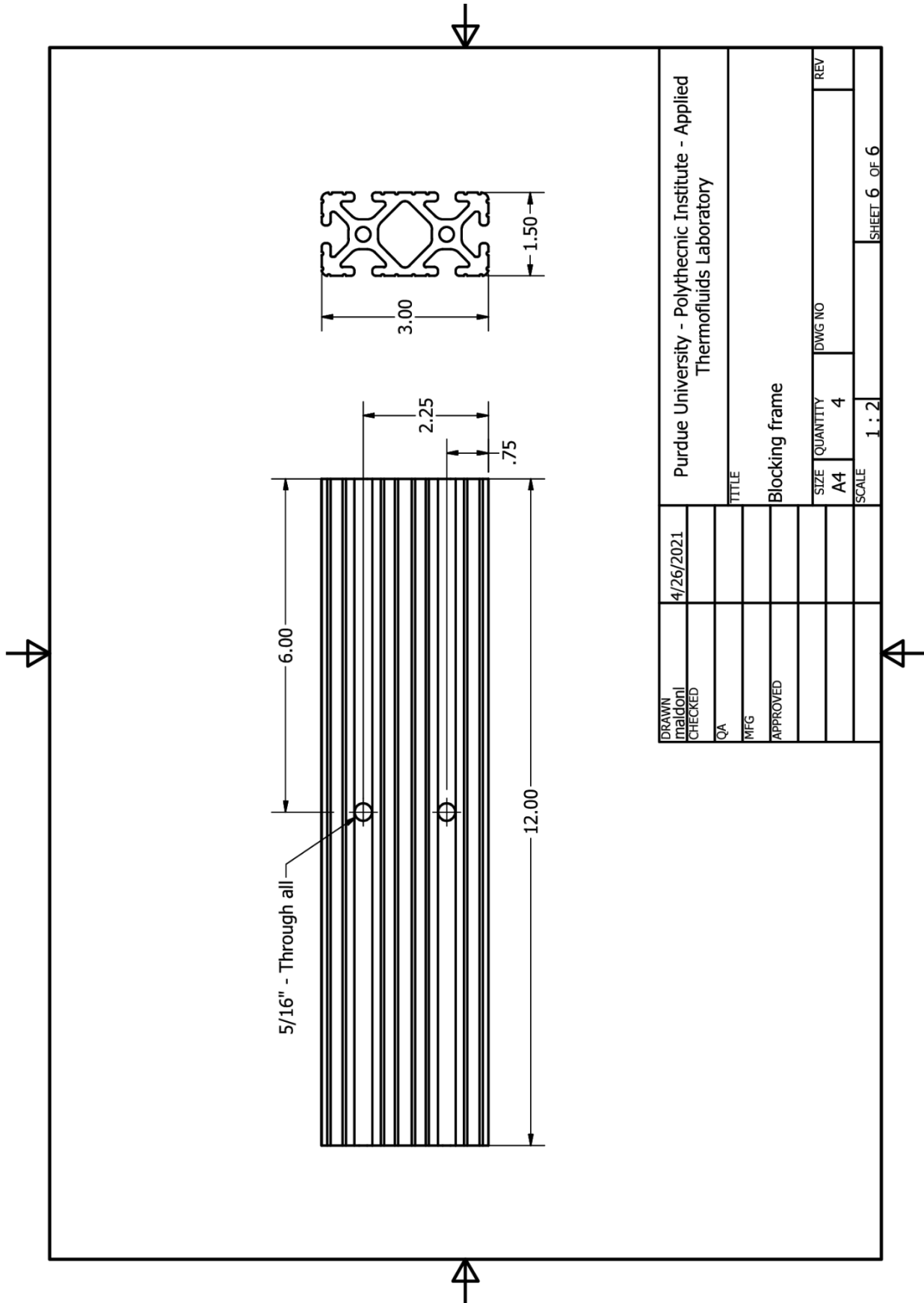












DRAWN maldonl	4/26/2021	Purdue University - Polytechnic Institute - Applied Thermofluids Laboratory			
CHECKED		TITLE			
QA		Blocking frame			
MFG					
APPROVED					
		SIZE	QUANTITY	DWG NO	REV
		A4	4		
		SCALE	1 : 2	SHEET 6 OF 6	

## APPENDIX C – BILL OF MATERIALES

*Table C.1. Bill of materials of surface weather station over concrete.*

Distributor	Reference	Name	Material	Unit	Quantity
Chainlinkfittings		2" Floor Flange w/ 2 Set Screws (Fits 1 7/8" OD)	Galvanized cast steel	unit	1
McMasterr Carr	4936T104	1-7/8" OD Galvanized Steel Framing Rail – 6 ft	Galvanized steel	unit	1
McMasterr Carr	97083A350	Anchors 5/8"-11 UNC	Zinc-Plated Steel	pkg	1
McMasterr Carr	97077A140	Installation tool anchor	N/A	unit	1
McMasterr Carr	92620A804	Hex head screw 5/8"-11 x 2 1/2"	Zinc Yellow- Chromate Plated Grade 8 Steel	unit	4
McMasterr Carr	98023A035	General purpose washer 5/8"	Zinc Yellow- Chromate Plated Grade 8 Steel	unit	4
McMasterr Carr	91104A035	Split lock washers 5/8"	Zinc Yellow- Chromate Plated Grade 8 Steel	unit	4
Meter Group	ATMOS 41	Weather station	N/A	unit	1
Meter Group	ZL6	Data logger	N/A	unit	1

*Table C.2. Bill of materials of surface weather station over grass.*

Distributor	Reference	Name	Material	Unit	Quantity
McMasterr Carr	89965K781	1-3/4" OD General purpose aluminum tube – 6 ft	Aluminum	unit	1
Meter Group	14141	Guy rope ring	N/A	unit	1
Meter Group	14142	Guy rope	N/A	ft	25
Meter Group	14289	12in guy rope anchor	N/A	unit	3
Meter Group	14290	Mast base plate w/center peg and set screw	N/A	unit	1
Meter Group	ATMOS 41	Weather station	N/A	unit	1
Meter Group	ZL6	Data logger	N/A	unit	1

Table C.3. Bill of materials for screen shaft mounting system.

Distributor	Reference	Name	Material	Unit	Quantity
Mcmaster Carr	47065T261	Surface Brackets for Single Rails	Anodized Aluminum	unit	2
Mcmaster Carr	3016T270	Eyebolts with Nuts—For Lifting 5/16" x 5"	Galvanized steel	unit	2
Mcmaster Carr	47065T103	T-Slotted Framing Rails - 1 1/2" x 1'	6105 Aluminum	unit	4
Mcmaster Carr	47065T103	T-Slotted Framing Rails - 1 1/2" x 10'	6105 Aluminum	unit	2
Mcmaster Carr	47065T103	T-Slotted Framing Rails - 1 1/2" x 1'	6105 Aluminum	unit	2
Mcmaster Carr	47065T103	T-Slotted Framing Rails - 1 1/2" x 1'	6105 Aluminum	unit	1
Mcmaster Carr	47065T630	Roller wheels	Plastic	unit	3
Mcmaster Carr	47065T109	T-Slotted Framing Rails - 3" x 1'	6105 Aluminum	unit	1
Mcmaster Carr	47065T762	Open Extended Gusset	Anodized Aluminum	unit	6
Mcmaster Carr	6330K430	Swivel Vibration- Damping Leveling Mounts with Threaded Stud 5/16"- 18 UNC	N/A	unit	4
Mcmaster Carr	47065T845	Corner Bracket for Single Rails	Anodized Aluminum	unit	4
Mcmaster Carr	47065T679	Open Gusset for Single Rails	Anodized Aluminum	unit	4
Mcmaster Carr	47065T258	Straight Surface Bracket for Double and Quad Rails	Anodized Aluminum	unit	4
Mcmaster Carr	47065T103	T-Slotted Framing Rails - 1 1/2" x 10'	6105 Aluminum	unit	1
Mcmaster Carr	47065T103	T-Slotted Framing Rails - 1 1/2" x 3'	6105 Aluminum	unit	1
Mcmaster Carr	47065T103	T-Slotted Framing Rails - 1 1/2" x 1'	6105 Aluminum	unit	1
Mcmaster Carr	47065T279	Tee Surface Bracket for Single Rails	Anodized Aluminum	unit	2
Mcmaster Carr	47065T271	90° Angle Surface Bracket for Single Rails	Anodized Aluminum	unit	2
Mcmaster Carr	3014T460	Eyebolts—For Lifting	Steel	unit	1
Mcmaster Carr	47065T804	Double Six Slot Rails—Cut-to- Length (per Inch)-3"	6105 Aluminum	unit	2

Table C.3. Bill of materials for screen shaft mounting system (continued).

Distributor	Reference	Name	Material	Unit	Quantity
Mcmaster Carr	47065T103	T-Slotted Framing Rails - 1 1/2" x 10'	6105 Aluminum	unit	1
Mcmaster Carr	92198A693	18-8 Stainless Steel Hex Head Screws 5/16"-18 UNC x 2 1/2"	18-8 Stainless steel	unit	4
Mcmaster Carr	90107A030	General purpose washer 5/16"	Stainless steel	unit	8
Mcmaster Carr	91831A030	18-8 Stainless Steel Nylon-Insert Locknuts 5/16"	18-8 Stainless steel	unit	4
Mcmaster Carr	92673A119	18-8 Stainless Steel Hex Nuts	18-8 Stainless steel	unit	1
Mcmaster Carr	92198A703	18-8 Stainless Steel Hex Head Screws 5/16"-18 UNC x 5"	18-8 Stainless steel	unit	2
Mcmaster Carr	90107A030	General purpose washer 5/16"	Stainless steel	unit	4
Mcmaster Carr	91831A030	18-8 Stainless Steel Nylon-Insert Locknuts 5/16"	18-8 Stainless steel	unit	2
Meter Group	ATMOS 14	Temperature, Humidity, and pressure sensor	N/A	unit	1
Meter Group	ATMOS 22	Anemometer	N/A	unit	1
Meter Group		Custom cable 15 m	N/A	unit	2

Table C.4. Bill of materials for Utility Shaft No.3 mounting system.

Distributor	Reference	Name	Material	Units	Quantity
Mcmaster Carr	47065T261	Surface Brackets for Single Rails	Anodized Aluminum	unit	2
Mcmaster Carr	47065T103	T-Slotted Framing Rails - 1 1/2" x 10'	6105 Aluminum	unit	1
Mcmaster Carr	47065T103	T-Slotted Framing Rails - 1 1/2" x 3'	6105 Aluminum	unit	1
Mcmaster Carr	47065T103	T-Slotted Framing Rails - 1 1/2" x 1'	6105 Aluminum	unit	1
Mcmaster Carr	47065T279	Tee Surface Bracket for Single Rails	Anodized Aluminum	unit	2
Mcmaster Carr	47065T271	90° Angle Surface Bracket for Single Rails	Anodized Aluminum	unit	2
Mcmaster Carr	47065T103	T-Slotted Framing Rails - 1 1/2" x 10'	6105 Aluminum	unit	1

Table C.4. Bill of materials for Utility Shaft No.3 mounting system (continued).

Distributor	Reference	Name	Material	Units	Quantity
McMaster Carr	47065T109	Double Six Slot Rails - 3" x 1'	6105 Aluminum	unit	2
McMaster Carr	47065T254	Extended Corner Bracket for Double and Quad Rails	Anodized Aluminum	unit	4
McMaster Carr	47065T804	Double Six Slot Rails—Cut-to-Length (per Inch)-3"	6105 Aluminum	unit	2
McMaster Carr	47065T258	Straight Surface Bracket for Double and Quad Rails	Anodized Aluminum	unit	4
McMaster Carr	92198A693	18-8 Stainless Steel Hex Head Screws - 5/16" - 18 UNC x 2 1/2"	18-8 Stainless steel	unit	4
McMaster Carr	90107A030	General purpose washer 5/16"	Stainless steel	unit	8
McMaster Carr	91831A030	18-8 Stainless Steel Nylon-Insert Locknuts 5/16"	18-8 Stainless steel	unit	4
McMaster Carr	92198A703	18-8 Stainless Steel Hex Head Screws 5/16"-18 UNC x 5"	18-8 Stainless steel	unit	18
McMaster Carr	90107A030	General purpose washer 5/16"	Stainless steel	unit	44
McMaster Carr	91831A030	18-8 Stainless Steel Nylon-Insert Locknuts 5/16"	18-8 Stainless steel	unit	22
McMaster Carr	92198A705	18-8 Stainless Steel Hex Head Screws - 5/16" - 18 UNC x 5 1/2"	18-8 Stainless steel	unit	4
McMaster Carr	92198A695	18-8 Stainless Steel Hex Head Screws - 5/16" - 18 UNC x 3"	18-8 Stainless steel	unit	16
Meter Group	ATMOS 14	Temperature, Humidity, and pressure sensor	N/A	unit	1
Meter Group	ATMOS 22	Anemometer	N/A	unit	1
Meter Group		Custom cable 15 m	N/A	unit	2

Table C.5. Bill of materials for Eagle Creek vent shaft and drop shaft mounting system.

Distributor	Reference	Name	Material	Units	Quantity
Mcmaster Carr	5537T272	Butt Anchor Concealed Brackets	Zinc	unit	2
Mcmaster Carr	47065T103	T-Slotted Framing Rails - 1 1/2" x 10'	6105 Aluminum	unit	1
Mcmaster Carr	47065T103	T-Slotted Framing Rails - 1 1/2" x 3'	6105 Aluminum	unit	1
Mcmaster Carr	47065T103	T-Slotted Framing Rails - 1 1/2" x 1'	6105 Aluminum	unit	1
Mcmaster Carr	47065T279	Tee Surface Bracket for Single Rails	Anodized Aluminum	unit	2
Mcmaster Carr	47065T271	90° Angle Surface Bracket for Single Rails	Anodized Aluminum	unit	2
Mcmaster Carr	3014T460	Eyebolts—For Lifting	Steel	unit	1
Mcmaster Carr	47065T804	Double Six Slot Rails—Cut-to-Length (per Inch)-3"	6105 Aluminum	unit	2
Mcmaster Carr	47065T103	T-Slotted Framing Rails - 1 1/2" x 10'	6105 Aluminum	unit	1
Mcmaster Carr	47065T103	T-Slotted Framing Rails - 1 1/2" x 1'	6105 Aluminum	unit	1
Mcmaster Carr	47065T630	Roller wheels	Plastic	unit	3
Mcmaster Carr	47065T109	Double Six Slot Rails - 3" x 1'	6105 Aluminum	unit	2
Mcmaster Carr	47065T762	Open Extended Gusset	Anodized Aluminum	unit	2
Mcmaster Carr	3016T270	Eyebolts with Nuts—For Lifting 5/16" x 5"	Galvanized steel	unit	2
Mcmaster Carr	47065T906	Open Extended Gusset for Double and Quad Rails	Anodized Aluminum	unit	4
Mcmaster Carr	47065T258	Straight Surface Bracket for Double and Quad Rails	Anodized Aluminum	unit	4
Mcmaster Carr	92673A119	18-8 Stainless Steel Hex Nuts	18-8 Stainless steel	unit	1
Mcmaster Carr	92198A703	18-8 Stainless Steel Hex Head Screws 5/16"-18 UNC x 5"	18-8 Stainless steel	unit	2
Mcmaster Carr	90107A030	General purpose washer 5/16"	Stainless steel	unit	4

*Note.* This bill is only for one shaft in Eagle Creek. The total number of parts used in the Eagle Creek location is twice.

Table C.5. Bill of materials for Eagle Creek vent shaft and drop shaft mounting system (continued).

Distributor	Reference	Name	Material	Units	Quantity
McMaster Carr	91831A030	18-8 Stainless Steel Nylon-Insert Locknuts 5/16"	18-8 Stainless steel	unit	2
McMaster Carr	92196A595	18-8 Stainless Steel Socket Head Screws - 5/16" - 18 UNC x 3"	18-8 Stainless steel	unit	16
McMaster Carr	90107A030	General purpose washer 5/16"	Stainless steel	unit	16
McMaster Carr	91831A030	18-8 Stainless Steel Nylon-Insert Locknuts 5/16"	18-8 Stainless steel	unit	16
Meter Group	ATMOS 14	Temperature, Humidity, and pressure sensor	N/A	unit	1
Meter Group	ATMOS 22	Anemometer	N/A	unit	1
Meter Group		Custom cable 15 m	N/A	unit	2

*Note.* This bill is only for one shaft in Eagle Creek. The total number of parts used in the Eagle Creek location is twice.



## APPENDIX D – MONTHLY NO-RAIN CONDITION SURFACE MEASUREMENTS

Table D.1. Eagle Creek averaged atmospheric experimental measurements.

Month	Time segment		Atmospheric pressure (hPa)			Atmospheric temperature (°C)			Atmospheric vapor pressure (Pa)			Wind speed (m/s)		
	From	To	Samples	Average	Uncertainty	Average	Uncertainty	Average	Uncertainty	Average	Uncertainty	Average	Uncertainty	Average
May	5/11/2020 0:00	5/14/2020 0:00	864	998.888	±1.121	9.534	±0.672	697.029	±34.133	0.917	±0.302			
June	6/16/2020 0:00	6/20/2020 0:00	1152	996.170	±1.136	24.613	±0.673	1521.457	±34.251	0.567	±0.301			
July	7/13/2020 0:00	7/15/2020 0:00	576	992.152	±1.124	23.848	±0.716	1779.428	±34.616	0.672	±0.302			
August	8/20/2020 0:00	8/23/2020 0:00	864	991.270	±1.122	22.975	±0.706	1766.936	±34.086	0.482	±0.300			
September	9/15/2020 0:00	9/23/2020 0:00	2304	999.480	±1.131	16.783	±0.644	1066.022	±35.343	0.767	±0.301			
October	10/8/2020 0:00	10/11/2020 0:00	864	993.361	±1.132	18.558	±0.719	1389.575	±42.799	0.462	±0.301			
November	11/5/2020 12:00	11/9/2020 12:00	1152	999.981	±1.119	13.738	±0.703	1111.481	±34.813	0.427	±0.301			
December	12/16/2020 0:00	12/19/2020 0:00	864	996.869	±1.176	-0.788	±0.622	498.492	±32.823	0.859	±0.301			
January	1/7/2021 0:00	1/12/2021 0:00	1440	1001.466	±1.124	-1.390	±0.620	436.350	±32.776	1.075	±0.301			
February	2/6/2021 0:00	2/10/2021 0:00	1152	999.298	±1.135	-7.883	±0.643	249.292	±33.034	1.033	±0.301			
March	3/4/2021 0:00	3/8/2021 0:00	1152	1002.499	±1.128	3.467	±0.655	400.531	±33.007	1.102	±0.303			
April	4/13/2021 0:00	4/19/2021 0:00	1728	991.914	±1.125	11.126	±0.641	681.080	±33.129	1.138	±0.302			

Table D.2. Utility shaft No.3 averaged atmospheric experimental measurements.

Month	Time segment		Atmospheric pressure (hPa)			Atmospheric temperature (°C)			Atmospheric vapor pressure (Pa)			Wind speed (m/s)		
	From	To	Samples	Average	Uncertainty	Average	Uncertainty	Average	Uncertainty	Average	Uncertainty	Average	Uncertainty	Average
May	5/11/2020 0:00	5/14/2020 0:00	864	998.425	±1.047	9.485	±0.684	703.815	±35.807	1.729	±0.308			
June	6/16/2020 0:00	6/20/2020 0:00	1152	995.684	±1.064	24.353	±0.684	1529.931	±36.046	0.854	±0.302			
July	7/13/2020 0:00	7/15/2020 0:00	576	991.503	±1.051	23.353	±0.712	1797.643	±36.640	1.199	±0.306			
August	8/20/2020 0:00	8/23/2020 0:00	864	990.815	±1.048	22.671	±0.709	1762.786	±36.461	0.728	±0.301			
September	9/15/2020 0:00	9/23/2020 0:00	2304	999.316	±1.058	16.852	±0.663	1076.065	±36.989	1.176	±0.302			
October	10/8/2020 0:00	10/11/2020 0:00	864	993.037	±1.059	19.152	±0.727	1415.362	±43.832	1.476	±0.311			
November	11/5/2020 12:00	11/9/2020 12:00	1152	999.617	±1.045	14.913	±0.712	1114.451	±36.167	1.116	±0.305			
December	12/16/2020 0:00	12/19/2020 0:00	864	996.580	±1.106	-0.606	±0.643	495.258	±34.559	1.817	±0.307			
January	1/7/2021 0:00	1/12/2021 0:00	1440	1001.087	±1.051	-1.396	±0.644	433.845	±34.554	1.640	±0.303			
February	2/6/2021 0:00	2/10/2021 0:00	1152	999.097	±1.062	-7.862	±0.665	245.936	±34.784	1.752	±0.305			
March	3/4/2021 0:00	3/8/2021 0:00	1152	1002.197	±1.055	3.626	±0.667	402.395	±34.777	1.849	±0.308			
April	4/13/2021 0:00	4/19/2021 0:00	1728	991.517	±1.052	10.858	±0.657	694.730	±34.841	2.047	±0.307			

Table D.3. Screen shaft averaged atmospheric experimental measurements.

Month	Time segment		Atmospheric pressure (hPa)			Atmospheric temperature (°C)			Atmospheric vapor pressure (Pa)			Wind speed (m/s)		
	From	To	Samples	Average	Uncertainty	Average	Uncertainty	Average	Uncertainty	Average	Uncertainty	Average	Uncertainty	Average
May	5/11/2020 0:00	5/14/2020 0:00	864	999.309	±1.023	9.081	±0.684	724.000	±37.537	2.255	±0.321			
June	6/16/2020 0:00	6/20/2020 0:00	1152	996.457	±1.040	23.217	±0.693	1616.531	±37.964	1.040	±0.304			
July	7/13/2020 0:00	7/15/2020 0:00	576	992.200	±1.027	22.799	±0.727	1817.695	±37.401	0.924	±0.303			
August	8/20/2020 0:00	8/23/2020 0:00	864	991.472	±1.024	21.772	±0.715	1768.879	±38.374	0.805	±0.303			
September	9/15/2020 0:00	9/23/2020 0:00	2304	999.655	±1.034	16.222	±0.665	1088.013	±38.220	1.331	±0.303			
October	10/8/2020 0:00	10/11/2020 0:00	864	993.438	±1.035	18.512	±0.742	1405.931	±43.805	1.079	±0.304			
November	11/5/2020 12:00	11/9/2020 12:00	1152	999.925	±1.021	14.087	±0.723	1080.982	±37.733	0.958	±0.305			
December	12/16/2020 0:00	12/19/2020 0:00	864	997.032	±1.084	-0.341	±0.649	508.460	±36.268	1.901	±0.306			
January	1/7/2021 0:00	1/12/2021 0:00	1440	1001.333	±1.027	-1.086	±0.645	442.870	±36.179	1.798	±0.303			
February	2/6/2021 0:00	2/10/2021 0:00	1152	999.479	±1.039	-7.404	±0.670	261.642	±36.430	1.409	±0.301			
March	3/4/2021 0:00	3/8/2021 0:00	1152	1002.648	±1.031	3.565	±0.668	439.906	±36.298	1.187	±0.303			
April	4/13/2021 0:00	4/19/2021 0:00	1728	992.095	±1.028	10.540	±0.661	703.114	±36.410	1.526	±0.305			

## APPENDIX E – CFD BOUNDARY CONDITIONS FOR DRTC+ECT ALIGNMENT

*Table E.1. Monthly CFD boundary conditions for DRTC+ECT alignment.*

Month	$\Delta P_t$ (Pa)			$\Delta P_w$ (Pa)			$T$ (K)			$Y_v$ ( $kg_{H_2O}/kg_{humidair}$ ) ( $1 \times 10^{-3}$ )		
	EC	US No.3	SS	EC	US No.3	SS	EC	US No.3	SS	EC	US No.3	SS
May	-64.783	-78.470	0.000	2.614	1.294	0.000	282.684	282.635	282.231	4.352	4.396	4.519
June	-61.235	-74.276	0.000	0.444	0.207	0.000	297.763	297.503	296.367	9.555	9.613	10.153
July	-61.124	-74.095	0.000	0.234	-0.338	0.000	296.998	296.503	295.949	11.232	11.355	11.474
August	-61.240	-74.264	0.000	0.243	0.070	0.000	296.125	295.821	294.922	11.162	11.141	11.172
September	-63.142	-76.486	0.000	0.711	0.235	0.000	289.933	290.002	289.372	6.661	6.725	6.798
October	-62.262	-75.349	0.000	0.563	-0.596	0.000	291.708	292.302	291.662	8.747	8.913	8.850
November	-63.709	-77.047	0.000	0.444	-0.196	0.000	286.888	288.063	287.237	6.943	6.964	6.752
December	-67.112	-81.150	0.000	1.829	0.199	0.000	272.362	272.544	272.809	3.116	3.097	3.178
January	-67.602	-81.752	0.000	1.329	0.347	0.000	271.760	271.754	272.064	2.715	2.700	2.756
February	-69.139	-83.595	0.000	0.600	-0.713	0.000	265.267	265.288	265.746	1.553	1.533	1.630
March	-66.471	-80.424	0.000	0.123	-1.266	0.000	276.617	276.776	276.715	2.489	2.501	2.734
April	-63.998	-77.528	0.000	0.629	-1.129	0.000	284.276	284.008	283.690	4.282	4.370	4.420

*Note.* EC stands for Eagle Creek, US No.3 stands for utility shaft No.3, and SS stands for screen shaft.

# APPENDIX F – DRTC+ECT ALIGNMENT MONTHLY IN-SHAFT EXPERIMENTAL MEASUREMENTS

Table F.1.1. Vertical velocity experimental measurements from in-shaft weather stations.

Time segment													
In-shaft vertical velocity (m/s)													
Month	From	To	Samples	EC vent shaft			EC drop shaft			US No.3			SS
				Average	Uncertainty	Uncertainty	Average	Uncertainty	Uncertainty	Average	Uncertainty	Uncertainty	
May	5/11/2020 0:00	5/14/2020 0:00	864	-0.713	±0.305	±0.304	-0.832	±0.304	0.365	±0.302	-0.549	±0.303	
June	6/16/2020 0:00	6/20/2020 0:00	1152	0.007	±0.300	±0.300	0.012	±0.300	-0.163	±0.300	-0.068	±0.300	
July	7/13/2020 0:00	7/15/2020 0:00	576	0.004	±0.300	±0.300	-0.004	±0.300	-0.118	±0.300	-0.077	±0.300	
August	8/20/2020 0:00	8/23/2020 0:00	864	-0.184	±0.301	±0.301	-0.112	±0.301	-0.151	±0.300	-0.069	±0.300	
September	9/15/2020 0:00	9/23/2020 0:00	2304	-0.752	±0.302	±0.301	-0.622	±0.301	-0.185	±0.300	-0.114	±0.300	
October	10/8/2020 0:00	10/11/2020 0:00	864	-0.363	±0.303	±0.302	-0.316	±0.302	-0.143	±0.300	-0.228	±0.301	
November	11/5/2020 12:00	11/9/2020 12:00	1152	-0.822	±0.304	±0.304	-0.788	±0.304	-0.084	±0.300	-0.109	±0.300	
December	12/16/2020 0:00	12/19/2020 0:00	864	-3.144	±0.301	±0.301	-2.862	±0.301	-1.255	±0.300	0.254	±0.300	
January	1/7/2021 0:00	1/12/2021 0:00	1440	-2.987	±0.301	±0.301	-2.574	±0.301	-1.243	±0.300	-0.287	±0.300	
February	2/6/2021 0:00	2/10/2021 0:00	1152	-3.818	±0.301	±0.300	-2.954	±0.300	-1.448	±0.300	-1.436	±0.300	
March	3/4/2021 0:00	3/8/2021 0:00	1152	-2.399	±0.303	±0.303	-1.954	±0.303	-1.019	±0.301	-0.354	±0.300	
April	4/13/2021 0:00	4/19/2021 0:00	1728	-0.980	±0.303	±0.302	-0.946	±0.302	0.071	±0.301	0.055	±0.300	

Note. EC stands for Eagle Creek, US No.3 stands for utility shaft No.3, and SS stands for screen shaft. The uncertainties were calculated with a confidence interval of 95%.

Table F.2. Temperature experimental measurements from in-shaft weather stations.

Time segment		In-shaft temperature (°C)									
		EC vent shaft				EC drop shaft			US No.3		
Month	From	To	Samples	Average	Uncertainty	Average	Uncertainty	Average	Uncertainty	Average	Uncertainty
May	5/11/2020 0:00	5/14/2020 0:00	864	9.107	±0.531	9.453	±0.537	11.920	±0.504	10.667	±0.518
June	6/16/2020 0:00	6/20/2020 0:00	1152	18.790	±0.507	17.801	±0.504	19.496	±0.505	17.052	±0.509
July	7/13/2020 0:00	7/15/2020 0:00	576	20.640	±0.528	20.335	±0.520	20.856	±0.508	19.261	±0.514
August	8/20/2020 0:00	8/23/2020 0:00	864	18.893	±0.508	19.287	±0.500	20.861	±0.510	19.069	±0.518
September	9/15/2020 0:00	9/23/2020 0:00	2304	15.752	±0.517	16.200	±0.519	17.929	±0.510	15.953	±0.505
October	10/8/2020 0:00	10/11/2020 0:00	864	15.249	±0.526	16.028	±0.532	17.756	±0.520	17.043	±0.534
November	11/5/2020 12:00	11/9/2020 12:00	1152	12.111	±0.538	12.848	±0.547	14.699	±0.515	14.039	±0.506
December	12/16/2020 0:00	12/19/2020 0:00	864	-0.546	±0.512	-0.464	±0.513	-0.088	±0.511	12.162	±0.500
January	1/7/2021 0:00	1/12/2021 0:00	1440	-1.103	±0.513	-1.019	±0.514	-0.866	±0.513	11.506	±0.500
February	2/6/2021 0:00	2/10/2021 0:00	1152	-7.724	±0.538	-7.616	±0.540	-7.388	±0.537	10.764	±0.500
March	3/4/2021 0:00	3/8/2021 0:00	1152	3.504	±0.542	3.948	±0.547	3.975	±0.536	11.014	±0.500
April	4/13/2021 0:00	4/19/2021 0:00	1728	10.799	±0.525	11.083	±0.527	11.881	±0.505	12.467	±0.503

Note. EC stands for Eagle Creek, US No.3 stands for utility shaft No.3, and SS stands for screen shaft. Measurements inside the boxes are from ATMOS 22, whereas the others are from ATMOS 14. The temperature from ATMOS 22 is taken due to the malfunctioning of ATMOS 14. The uncertainties were calculated with a confidence interval of 95%.

Table F.3. Vapor pressure experimental measurements from in-shaft weather stations.

Time segment		In-shaft water vapor mass fraction ( $kg_{H_2O}/kg_{humidair}$ )									
		EC vent shaft					EC drop shaft				
Month	From	To	Samples	Average ( $1 \times 10^{-3}$ )	Uncertainty ( $1 \times 10^{-4}$ )		Average ( $1 \times 10^{-3}$ )	Uncertainty ( $1 \times 10^{-4}$ )		Average ( $1 \times 10^{-3}$ )	Uncertainty ( $1 \times 10^{-4}$ )
May	5/11/2020 0:00	5/14/2020 0:00	864	4.699	$\pm 4.004$		4.787	$\pm 4.073$		7.869	$\pm 4.402$
June	6/16/2020 0:00	6/20/2020 0:00	1152	10.126	$\pm 5.162$		10.360	$\pm 5.045$		10.229	$\pm 5.249$
July	7/13/2020 0:00	7/15/2020 0:00	576	10.989	$\pm 5.598$		11.885	$\pm 5.477$		12.478	$\pm 5.692$
August	8/20/2020 0:00	8/23/2020 0:00	864	10.627	$\pm 5.211$					10.627	$\pm 5.706$
September	9/15/2020 0:00	9/23/2020 0:00	2304							8.055	$\pm 5.092$
October	10/8/2020 0:00	10/11/2020 0:00	864							9.613	$\pm 5.227$
November	11/5/2020 12:00	11/9/2020 12:00	1152							8.065	$\pm 4.671$
December	12/16/2020 0:00	12/19/2020 0:00	864							3.251	$\pm 2.562$
January	1/7/2021 0:00	1/12/2021 0:00	1440							2.817	$\pm 2.432$
February	2/6/2021 0:00	2/10/2021 0:00	1152							1.622	$\pm 1.470$
March	3/4/2021 0:00	3/8/2021 0:00	1152							2.682	$\pm 3.172$
April	4/13/2021 0:00	4/19/2021 0:00	1728							6.328	$\pm 4.402$

Note. EC stands for Eagle Creek, US No.3 stands for utility Shaft No.3, and SS stands for screen shaft. Months without measurements on EC vent shaft, EC drop shaft, and SS are due to the malfunctioning of ATMOS14. The uncertainties were calculated with a confidence interval of 95%.